

# **THE INFLUENCE OF RARE EARTH ELEMENTS ON THERMAL INFRARED SPECTRA OF MONAZITE**

VARAVARAI SUWANNAPURA

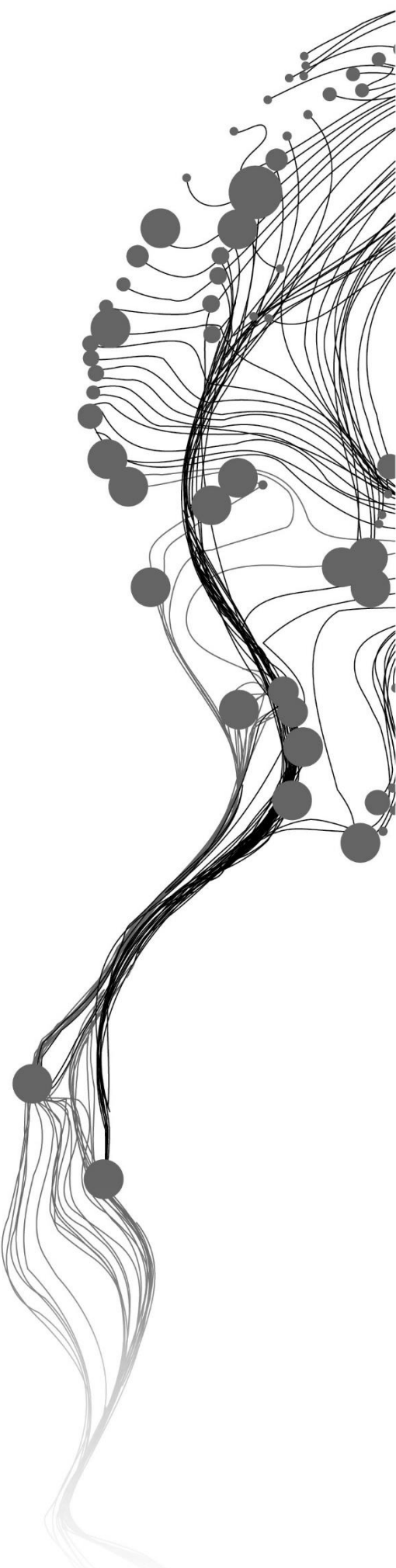
July, 2024

SUPERVISORS:

W.H. Bakker MSc

Dr. A.H Dijkstra





# THE INFLUENCE OF RARE EARTH ELEMENTS ON THERMAL INFRARED SPECTRA OF MONAZITE

VARAVARAI SUWANNAPURA

Enschede, The Netherlands, July, 2024

Thesis submitted to the Faculty of Geo-Information Science and Earth Observation of the University of Twente in partial fulfilment of the requirements for the degree of Master of Science in Geo-information Science and Earth Observation.

Specialization: Applied Remote Sensing for Earth Sciences

**SUPERVISORS:**

W.H. Bakker MSc

Dr. A.H. Dijkstra

**THESIS ASSESSMENT BOARD:**

Dr. C.A. Hecker (Chair)

Dr. C. Laukamp (External Examiner, CSIRO - Australia)

#### DISCLAIMER

This document describes work undertaken as part of a programme of study at the Faculty of Geo-Information Science and Earth Observation of the University of Twente. All views and opinions expressed therein remain the sole responsibility of the author, and do not necessarily represent those of the Faculty.

## ABSTRACT

Visible-to-short wave infrared spectra (350 – 2500 nm) are widely used to study rare earth element (REE)-bearing minerals in the fields of spectral geology and mineral exploration, as the direct diagnostic absorption features of REE electronic process can be observed in this range. However, fundamental understanding of the REE behaviour in the thermal infrared (TIR) region (4000 – 400  $\text{cm}^{-1}$ ; 4 – 25  $\mu\text{m}$ ) remains limited, since spectral features in this range are primarily influenced by the vibrational processes of the mineral group's molecules. This study conducted a detailed investigation to observe the influence of REEs on the fundamental vibration features of REE-host minerals in the TIR region. Laboratory-synthesized minerals were used to simplify the chemical and mineralogical complexity of the samples. Monazite was chosen as the main focus mineral in this study due to its straightforward synthesis process. REE variations within the mineral were introduced using synthetic single-REE monazite (REE = La to Gd) and two series of double-REE monazites (REE =  $\text{La}_{1-x}\text{Nd}_x$  and  $\text{La}_{1-x}\text{Sm}_x$ ). TIR spectra were recorded using ATR-FTIR spectroscopy, which offers distinct advantages in reproducibility and time-efficiency. For detailed analysis, the positions and absorbance intensities of 16 local features, corresponding to the maxima and minima due to the fundamental vibrations of the phosphate group within monazite, were extracted and used to observe the influence of REE in TIR spectra of monazite. The results demonstrated that the TIR spectra of the synthetic monazites exhibit systematic changes in response to varying REE contents. These changes in the spectral features of monazite were observed as variations in spectral intensity, shape, and positional shifts of the local features, corresponding to the effect of lanthanide contraction in single-REE monazites and the increased Nd and Sm content in double-REE monazites. The findings of this study offer valuable insights into how REEs influence the spectral features of host minerals in the TIR region, with possible application in proximal sensing of rocks containing REE-minerals.

## ACKNOWLEDGEMENTS

First of all, I would like to express my deepest gratitude to both of my supervisors, Wim Bakker and Dr. Arjan Dijkstra, for their guidance, patience, and support. Your motivation and encouragement helped me through challenging times. It really meant a lot to me. Thank you, Wim, for your help and insight on spectra processing and for critically reviewing my work. Thank you, Arjan, for your expertise in mineralogy and crystallography, and for teaching me how to “cook” a mineral! I truly enjoyed our discussions, and I have learned a lot of things from both of you.

I would like to extend my gratitude to Dr. Chris Hecker for your encouragement and helpful guidance when I reached out for assistance with thermal infrared. Your elective course was truly meaningful to me and sparked my curiosity. Without that course, I would not have been able to develop this MSc topic.

My sincere gratitude to the AES staff, especially my mentor, Dr. Islam Fadel. Thank you for your understanding, encouragement, and for listening when I was having a hard time. I learned so much from you. I also want to thank Bruno Portela for your help and support with both academic and non-academic matters.

Special thanks to my mom and dad. Thank you so much for always believing in me! Thank you for your support and understanding. More importantly, thank you for being happy and for taking care of your health properly. Knowing that both of you are happy and healthy, it's really put me at ease.

I want to thank all my friends here! Thank you very much for making my two years of master's studies full of joy and happiness. Special thanks to all my ARS friends for being with me through thick and thin for these two years! Thank you for the fun leisure talks and teatimes. It has been a pleasure to get to know all of you. I also want to thank all my 8th-floor Indonesian neighbours. I had so much fun hanging out with all of you, and I will miss our kitchen-complain sessions. Last but not least, I want to thank the most special person I have ever met here, Nasir. Thank you very much for everything. These two years of mine were not easy at all, but you truly helped make many things went easy on me. Thank you for always being my biggest supporter and for helping me become a better person. Thank you for being my peace of mind.

# TABLE OF CONTENTS

---

Abstract .....	i
Acknowledgements .....	ii
Table of contents .....	iii
List of figures .....	iv
List of tables .....	vi
List of abbreviations .....	vii
1. INTRODUCTION .....	1
1.1. Background .....	1
1.2. Problem statement .....	4
1.3. Research objective .....	5
1.4. Research questions .....	5
1.5. Thesis structure .....	5
2. DATASET AND METHODOLOGY .....	6
2.1. Dataset .....	6
2.2. Experimental method for monazite synthesis .....	7
2.3. Sample characterization and validation methods .....	8
2.4. TIR spectra analytical method .....	10
3. RESULTS: THE SYNTHESIZED PRODUCTS .....	13
3.1. The synthesized monazite products .....	13
3.2. Structural characterization from pXRD analysis .....	15
3.3. REE validation from VNIR-SWIR reflectance spectroscopic analysis .....	18
4. RESULTS: TIR SPECTRA OF SYNTHETIC MONAZITES .....	19
4.1. TIR spectra of synthetic monazite .....	19
4.2. Feature extraction .....	21
4.3. TIR spectra and feature extraction results of all synthetic monazite samples .....	22
5. DISCUSSION .....	31
5.1. Discussion on methodology .....	31
5.2. Changes in TIR spectra of monazite with different REE contents .....	34
5.3. Difference in TIR spectra of single-REE monazite (REE = La, Nd, Sm) from Sample Set 1 and 2 .....	40
5.4. The influence of REEs on TIR spectra of monazite .....	42
5.5. Comparison between the TIR spectra of synthetic and natural monazite samples .....	43
6. CONCLUSION AND RECOMMENDATIONS .....	47
6.1. Conclusion .....	47
6.2. Recommendations .....	48
List of references .....	49
Appendix .....	53

# LIST OF FIGURES

---

<b>Figure 1.1</b> TIR spectra from 2.5 - 25 $\mu\text{m}$ (4000 - 400 $\text{cm}^{-1}$ ) of Gd-phosphate polymorphs (Clavier et al., 2018) .....	3
<b>Figure 1.2</b> Fundamental vibrational features of major mineral groups, including phosphate (Williams, 1995) .....	3
<b>Figure 2.1</b> The VNIR-SWIR reflectance spectra of single-REE phosphates minerals, including monazites (mnz) (Dijkstra et al., 2024) .....	9
<b>Figure 2.2</b> A schematic diagram showing how ATR-FTIR works (Eid, 2022) .....	10
<b>Figure 2.3</b> The comparison between transmittance and absorbance spectra.....	11
<b>Figure 2.4</b> The calculation of an interpolated local minima using the second-degree polynomial fitting method (Van Ruitenbeek et al., 2014) .....	12
<b>Figure 3.1</b> The single and double-REE powder products obtained from the synthesis experiment.....	13
<b>Figure 3.2</b> Single-REE monazites from the Sample Set 1 .....	13
<b>Figure 3.3</b> The XRD patterns of single-REE products from the experimental synthesis study .....	15
<b>Figure 3.4</b> The XRD patterns of double-REE monazite synthesized in this study ( <b>Top</b> ) REE = $\text{La}_{1-x}\text{Nd}_x$ ( <b>Bottom</b> ) REE = $\text{La}_{1-x}\text{Sm}_x$ .....	16
<b>Figure 3.5</b> Unit cell parameters of double-REE monazite synthesized in this study ( <b>Left</b> ) REE = $\text{La}_{1-x}\text{Nd}_x$ ( <b>Right</b> ) REE = $\text{La}_{1-x}\text{Sm}_x$ .....	17
<b>Figure 3.6</b> Systematic decrease in cell volume as Nd and Sm content increases in double-REE monazites.....	17
<b>Figure 3.7</b> Reflectance spectra in VNIR-SWIR range (400 – 2400 nm) of all monazite products from the synthesis experiment in this study .....	18
<b>Figure 4.1</b> Example TIR absorbance spectrum from wavenumbers 4000 – 400 $\text{cm}^{-1}$ (wavelengths 2.5 – 25 $\mu\text{m}$ ) of synthetic monazite-(Pr) .....	19
<b>Figure 4.2</b> Example TIR absorbance spectrum from wavenumbers 1400 – 400 $\text{cm}^{-1}$ (wavelengths 7.14 – 25 $\mu\text{m}$ ) of synthetic monazite-(Pr). .....	20
<b>Figure 4.3</b> TIR absorbance spectrum of synthetic monazite-(Pr) from wavenumbers 1400 – 400 $\text{cm}^{-1}$ (wavelengths 7.14 – 25 $\mu\text{m}$ ) .....	21
<b>Figure 4.4</b> Results of the feature extraction method, showing the positions of the detected local features in the TIR absorbance spectra from wavenumbers 1400 – 400 $\text{cm}^{-1}$ (wavelengths 7.14 – 25 $\mu\text{m}$ ) of synthetic monazite-(Pr) .....	23
<b>Figure 4.5</b> The TIR absorbance spectra from 1400 – 400 $\text{cm}^{-1}$ (wavelengths 7.14 – 25 $\mu\text{m}$ ) of synthetic <b>single-REE monazites (La to Gd)</b> from <i>Sample Set 1 (synthesized as part of the work of Dijkstra et al., 2024)</i> .....	24
<b>Figure 4.6</b> The TIR absorbance spectra from 1400 – 400 $\text{cm}^{-1}$ (wavelengths 7.14 – 25 $\mu\text{m}$ ) of synthetic <b><math>\text{La}_{1-x}\text{Nd}_x</math> and single-REE: La and Nd monazites</b> from <i>Sample Set 2 (synthesized in this study)</i> .....	26
<b>Figure 4.7</b> The TIR absorbance spectra from 1400 – 400 $\text{cm}^{-1}$ (wavelengths 7.14 – 25 $\mu\text{m}$ ) of synthetic <b><math>\text{La}_{1-x}\text{Sm}_x</math> and single-REE: La and Sm monazites</b> from <i>Sample Set 2 (synthesized in this study)</i> .....	28
<b>Figure 5.1</b> TIR spectrum from wavenumbers 4000 – 400 $\text{cm}^{-1}$ of monazite-(Gd) ( <b>Top</b> ) from this study, recorded with ATR-FTIR ( <b>Bottom</b> ) modify from Heuser et al. (2014), recorded with transmission FTIR.....	32
<b>Figure 5.2</b> Example of interpolated local minimum obtained after applying the second-degree polynomial fitting function to Feature $\text{C}_{\text{min}2}$ from the spectra of monazite-( $\text{La}_{50}\text{Nd}_{50}$ ). .....	33
<b>Figure 5.3</b> Scatter plots showing how how <b>absorbance intensity of feature <math>\text{A}_{\text{max}3}</math></b> changes with different REE contents in synthetic monazites. ( <b>Left</b> ) Single-REE monazites (from Sample Set 1 and 2), ( <b>Middle</b> ) $\text{La}_{1-x}\text{Nd}_x$ monazites, and ( <b>Right</b> ) $\text{La}_{1-x}\text{Sm}_x$ monazites. ....	35
<b>Figure 5.4</b> Scatter plots showing how <b>absorbance intensity of feature <math>\text{D}_{\text{max}1}</math></b> changes with different REE contents in synthetic monazites. ( <b>Left</b> ) Single-REE monazites (from Sample Set 1 and 2), ( <b>Middle</b> ) $\text{La}_{1-x}\text{Nd}_x$ monazites, and ( <b>Right</b> ) $\text{La}_{1-x}\text{Sm}_x$ monazites. ....	36
<b>Figure 5.5</b> Scatter plots showing how <b>intensities between two local features: Feature <math>\text{C}_{\text{max}2}</math> and <math>\text{C}_{\text{max}3}</math> change relatively</b> with different REE contents in synthetic monazites ( <b>Left</b> ) Single-REE monazites (from Sample Set 1 and 2), ( <b>Middle</b> ) $\text{La}_{1-x}\text{Nd}_x$ monazites, and ( <b>Right</b> ) $\text{La}_{1-x}\text{Sm}_x$ monazites.....	37
<b>Figure 5.6</b> TIR spectra from wavenumbers 1200 – 900 $\text{cm}^{-1}$ of ( <b>Left</b> ) synthetic <b>single-REE monazites (La to Gd)</b> from <i>Sample Set 1</i> . ( <b>Middle</b> ) $\text{La}_{1-x}\text{Nd}_x$ and single-REE: La and Nd monazites from <i>Sample Set 2</i> . ( <b>Right</b> ) $\text{La}_{1-x}\text{Sm}_x$ and single-REE: La and Sm monazites from <i>Sample Set 2</i> .....	38



<b>Figure 5.7</b> Scatter plots showing a strong linear correlation in the changes of feature $C_{\min 2}$ position with different REE contents in synthetic monazites. <b>(Left)</b> Single-REE monazites (from Sample Set 1 and 2), <b>(Middle)</b> $La_{1-x}Nd_x$ monazites, and <b>(Right)</b> $La_{1-x}Sm_x$ monazites.....	39
<b>Figure 5.8</b> Scatter plots showing example of a strong linear correlation in changes of feature $B_{\max 1}$ position, contrasted with a polynomial regression in double-REE monazites across different REE contents in synthetic monazites. <b>(Left)</b> Single-REE monazites (from Sample Set 1 and 2), <b>(Middle)</b> $La_{1-x}Nd_x$ monazites, and <b>(Right)</b> $La_{1-x}Sm_x$ monazites.....	40
<b>Figure 5.9</b> Scatter plots showing example of a polynomial regression in double-REE monazites in feature $C_{\max 4}$ position, contrasted with the high deviation within a linear correlation in single-REE monazites across different REE contents in synthetic monazites. <b>(Left)</b> Single-REE monazites (from Sample Set 1 and 2), <b>(Middle)</b> $La_{1-x}Nd_x$ monazites, and <b>(Right)</b> $La_{1-x}Sm_x$ monazites .....	40
<b>Figure 5.10 (Left)</b> TIR spectra of single-REE monazites (REE = La, Nd, and Sm) from Sample Set 1 and Sample Set 2. <b>(Right)</b> XRD patterns of single-REE monazites (REE = La, Nd, and Sm) from Sample Set 1 and Sample Set 2. ....	41
<b>Figure 5.11</b> Scatter plots show the comparison of reported wavenumber of positional shifts in <b>(Left)</b> $B_{\max 1}$ feature <b>(Right)</b> $C_{\max 2}$ features in TIR spectra of synthetic single-REE monazites. The wavenumbers obtained from both Sample Set 1 (REE = La to Gd) and Sample Set 2 (REE = La, Nd, and Sm) in this study are plot along with the wavenumbers reported in Hezel & Ross (1966) and Heuser et al. (2014).. .....	42
<b>Figure 5.12</b> TIR spectra TIR absorbance spectra from wavenumbers 1400 – 400 $cm^{-1}$ (wavelengths 7.14 – 25 $\mu m$ ) of <b>(From bottom to top) synthetic monazite-(La)</b> from Sample Set 1, <b>synthetic natural-like monazite</b> (synthesized as part of the work of Dijkstra et al., 2024), <b>natural monazite from ITC collection</b> (used as part of the work of Dijkstra et al., 2024), <b>natural monazite from RRUFF database</b> (RRUFF ID: RA040106), and <b>natural monazite from USGS spectral library</b> (Spectrum title: HS255.3B NIC4bbb RREF).. .....	44

## LIST OF TABLES

---

<b>Table 1.1</b> Effective ionic radii of lanthanide (III) ions with coordinate number = 9 (Shannon, 1976).....	4
<b>Table 2.1</b> Summary table of laboratory-synthesized monazite samples used in this study.....	6
<b>Table 2.2</b> Information of materials used for synthesizing monazites.....	7
<b>Table 2.3</b> Mole quantities of each REE in double-REE monazite samples.....	7
<b>Table 3.1</b> List of the amount of total REE (in mol) in the starting solution as prepared for synthesizing the precipitation product (precursor) and in the final product obtained after thermal treatment. The percent yield indicates the relative proportions of REE the final product compared to the starting solution for each product. ....	14
<b>Table 4.1</b> Summary of the number of selected minima and maxima features for each feature group (A, B, C, and D).....	23
<b>Table 4.2 (Top)</b> Positions and <b>(Bottom)</b> absorbance intensities of the selected minima (min) and maxima (max) features within TIR absorbance spectra from wavenumbers 1400 – 400 $\text{cm}^{-1}$ of synthetic <b>single-REE monazites</b> from <i>Sample Set 1 (La to Gd)</i> and <i>Sample Set 2 (La, Nd, and Sm; labeled with [2])</i> .....	25
<b>Table 4.3 (Top)</b> Positions and <b>(Bottom)</b> absorbance intensities of the selected minima (min) and maxima (max) features within TIR absorbance spectra from wavenumbers 1400 – 400 $\text{cm}^{-1}$ of synthetic <b>La<sub>1-x</sub>Nd<sub>x</sub> (X as the Molar fraction of Nd) and single-REE: La (shown as 0.00*) and Nd (shown as 1.00*) monazites</b> from <i>Sample Set 2</i> . ....	27
<b>Table 4.4 (Top)</b> Positions and <b>(Bottom)</b> absorbance intensities of the selected minima (min) and maxima (max) features within TIR absorbance spectra from wavenumbers 1400 – 400 $\text{cm}^{-1}$ of synthetic <b>La<sub>1-x</sub>Sm<sub>x</sub> (X as the Molar fraction of Nd) and single-REE: La (shown as 0.00*) and Sm (shown as 1.00*) monazites</b> from <i>Sample Set 2</i> . ....	29
<b>Table 5.1</b> Chemical composition detail of each monazite sample and TIR spectra acquisition technique.....	43

## LIST OF ABBREVIATIONS

---

REE	: Rare earth element
LREE	: Light rare earth element
REO	: Rare earth oxide
CN	: Coordination number
IR	: Infrared
VNIR	: Visible-near infrared (400 - 1000 nm)
SWIR	: Shortwave infrared (1000 - 2500 nm)
TIR	: Thermal infrared (3 - 25 $\mu\text{m}$ )
HSI	: Hyperspectral imaging
FTIR spectroscopy	: Fourier-transform infrared spectroscopy
ATR-FTIR spectroscopy	: Attenuated total reflectance-Fourier transform spectroscopy
XRD	: X-ray diffraction
pXRD	: Powder X-ray diffraction
ASD	: Analytical spectral devices
KBr	: Potassium bromide

### Chemical formula:

$[\text{REE}]\text{PO}_4$	: Monazite-(REE); anhydrous orthophosphate
$[\text{REE}]\text{PO}_4 \cdot n\text{H}_2\text{O}$	: Rhabdophane-(REE); hydrous orthophosphate
$\text{H}_3\text{PO}_4$	: Orthophosphoric acid
$[\text{REE}]_2\text{O}_3$	: Rare earth metal (III) oxide

### Modes of fundamental vibrations:

$\nu$	: Stretching mode
$\delta$	: Bending mode
$\nu_{\text{as}}$	: Antisymmetric stretching
$\nu_{\text{s}}$	: Symmetric stretching
$\delta_{\text{as}}$	: Antisymmetric bending
$\delta_{\text{s}}$	: Symmetric bending



# 1. INTRODUCTION

## 1.1. Background

The global demand for rare earth elements (REEs) has experienced sustained growth due to the rapid advancement of modern technology and the worldwide response to the clean energy transition (Smelror et al., 2023). REEs are widely considered as critical raw materials in many industrial countries because of their significant economic importance and potential for supply shortages (Lusty & Gunn, 2014; Kalvig, 2022). REEs, comprising 15 lanthanides (including La, Ce, Pr, Nd, Pm, Sm, Eu, Gd, Tb, Dy, Ho, Er, Tm, Yb, and Lu), yttrium (Y), and scandium (Sc), play a vital role in modern technology due to their distinctive physical, chemical, and magnetic properties. These properties can help optimize the performance and efficiency of numerous modern products, especially in the context of green technology (Balaram, 2019)

In the field of spectral geology, many research and exploration projects of REEs have been conducted using hyperspectral remote sensing technique. This method offers distinct advantages, such as time, cost-effectiveness, and non-destructiveness. The primary focus of these studies is the detection and identification of REEs, mainly conducted in the visible-near infrared (VNIR) range (400 – 1000 nm) and the shortwave infrared (SWIR) range (1000 – 2500 nm). The VNIR-SWIR approach is considered as a direct method for detecting REEs (Asadzadeh & de Souza Filho, 2016). This is because REEs exhibit distinctive absorption features in the electromagnetic spectrum within this range, resulting from the electronic processes, the spin-orbit coupling and the crystal field effect (Hunt, 1977; Clark, 1999; Dijkstra et al., 2024) which are commonly observed in VNIR-SWIR spectra of transition metals and lanthanide elements, resulting from the splitting in energy levels.

The VNIR-SWIR reflectance spectroscopy technique has proven to be a powerful tool for detecting and identifying REEs. Numerous studies have been conducted at various scales, including aerial (airborne and spaceborne), terrestrial, and laboratory scales. The studies consistently demonstrate promising results in the detection of REEs. For instance, Morin-Ka (2018) used the hyperspectral imaging (HSI) technique to detect and identify REEs in different rock types by comparing the spectral signatures of rock samples with those of pure synthetic rare earth oxides (REOs). The findings consistently confirmed the presence of REEs in the rocks. However, some limitations of using VNIR-SWIR for REEs study were noted in this study. Firstly, not all REEs, such as La and Ce, exhibit diagnostic absorption features within this spectral range. Another limitation can be found when dealing with iron oxides-rich samples, as the broad absorption features of iron oxides at 700 – 900 nm can overlap with the features of some REEs. This overlapping could be an obstacle to detecting Nd, Dy, Ho, Er, and Tm since their absorption features are also exhibited in this range (Tan et al., 2021).

In contrast to the abundance of research in the VNIR-SWIR range, the amount of research conducted on the thermal infrared (TIR) range (3 - 25  $\mu\text{m}$ ) studied on REEs remains relatively limited. Since the VNIR-SWIR range has already proven to be an effective technique for the direct detection of electronic absorption features of almost every REE, except for La, Ce, Lu, and Y, as each REE displays consistent patterns and positions of absorption features, which can be used for the direct detection and identification of REEs in the minerals. (Hunt, 1977; Clark et al., 1990; Morin-Ka, 2018; Dijkstra et al., 2024;). However,

it is essential to note that most rock-forming minerals, as well as REEs-host minerals, show diagnostic spectral features in the TIR range (Williams, 1995; Christensen et al., 2000). Nevertheless, the baseline knowledge of how REEs influence the TIR spectra of the host mineral remains limited.

The absorption features observed in the TIR range are the consequence of the vibrational process occurring within the molecular bonds of minerals (Clark, 1999). These bond vibrations can be categorized into fundamental bending and stretching modes, overtones (which represent multiples of the same fundamental mode), and combinations (involving the addition of different modes). These vibrational motions are directly dependent on the crystal structure and chemical composition of the mineral, leading to unique patterns in the spectra of each mineral (Christensen et al., 2000).

Studies of several minerals conducted by Salisbury et al. (1987), Christensen et al. (2000), and Laukamp et al. (2021) have shown that fundamental frequencies are helpful for identifying minerals, especially in distinguishing different mineral groups. This is because the fundamental vibrations of various anion groups, such as  $\text{SiO}_4$ ,  $\text{CO}_3$ , and  $\text{PO}_4^-$ , produce diagnostic and well-separated spectral features, which can be seen within the reststrahlen bands, the strong reflectance peaks in the TIR region (Salisbury et al., 1987).

In nature, REEs never exist as a native elemental form like gold and silver. Instead, they are found as multi-cationic solid solutions within various groups of minerals, including phosphates, silicates, carbonates, and oxides (Balaram, 2019). One of the primary sources of REEs is Monazite, which is an anhydrous phosphate ( $[\text{REE}]\text{PO}_4$ ) mineral (Turner et al., 2016). Monazite exhibits a monoclinic structure and commonly hosts light rare earth elements (LREEs; La - Gd).

The study of Clavier et al. (2018) on laboratory-synthesized gadolinium phosphate ( $\text{GdPO}_4$ ) polymorphs of monazite, xenotime, rhabdophane, and churchite reveals that monazite shows strong and unique reststrahlen bands and diagnostic absorption features in TIR range from 8.33 - 25  $\mu\text{m}$  (1200 - 400  $\text{cm}^{-1}$ ) due to the fundamental bending and stretching modes of the phosphate  $(\text{PO}_4)^{3-}$  (Figure 1.1). Similarly, Williams (1995) also shows that fundamental vibration modes of  $(\text{PO}_4)^{3-}$  in phosphate minerals occur in the TIR range.

Several studies have attempted to identify diagnostic features from vibration modes of REEs of geological materials in the TIR region. Unfortunately, this direct detection approach has not produced the desired results. Laakso et al. (2019) used a longwave infrared HSI technique from 8 - 12  $\mu\text{m}$  to investigate TIR spectra of various naturally occurring REEs-bearing minerals, including monazite. The spectra results were then compared to the 2 - 26  $\mu\text{m}$  spectra of synthetic pure REO compounds from Sheibley & Fowler (1966). However, the TIR spectra of the mineral samples show no sign of diagnostic features from REEs that can be observed from REO in the study range. Additionally, Morin-Ka (2018) conducted a similar analysis, measuring compacted pure REO powders using the longwave infrared HSI technique from 6 - 14  $\mu\text{m}$ . In this case, the spectral results did not reveal any diagnostic spectral features that can be used to distinguish REEs within the study range.

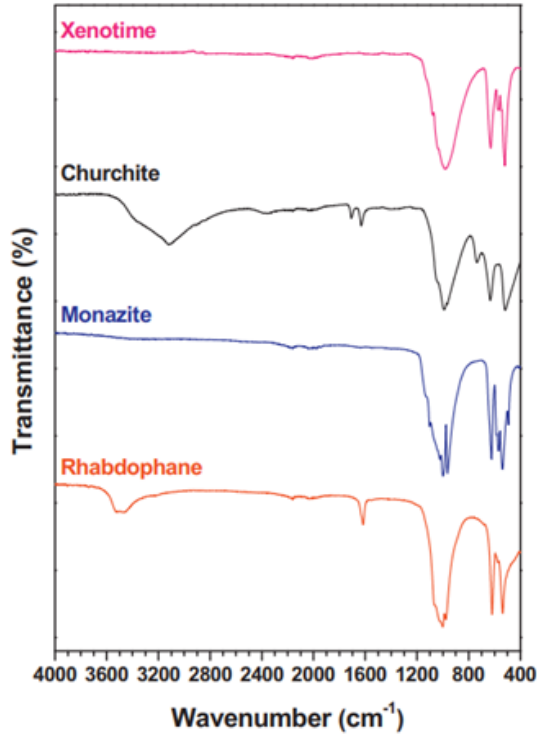


Figure 1.1 TIR spectra from 2.5 - 25  $\mu\text{m}$  (4000 - 400  $\text{cm}^{-1}$ ) of Gd-phosphate polymorphs (Clavier et al., 2018)

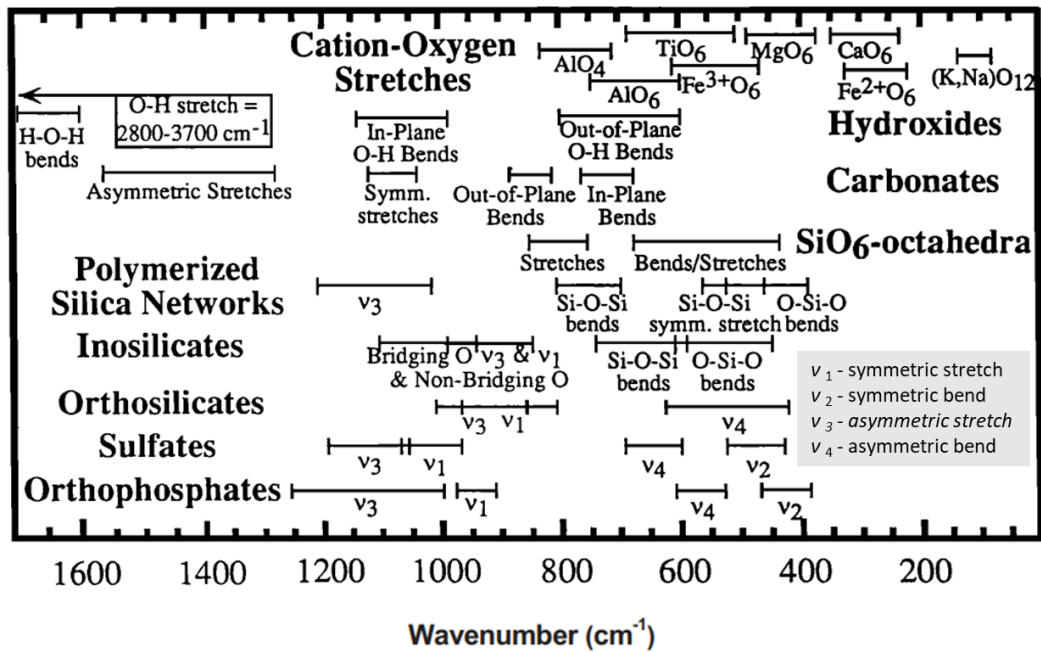


Figure 1.2 Fundamental vibrational features of major mineral groups, including phosphate (Williams, 1995)

However, in the field of material sciences, the TIR spectra of laboratory-synthesized inorganic rare earth compounds with various compositions and structures have been examined extensively. Fourier-Transform infrared spectroscopy (FTIR) has been widely used in these studies. FTIR is commonly used for studying infrared spectra of both organic and inorganic substances, as the data can be used to interpret the chemical composition of the sample due to the vibrational motion of the molecular bonds (Stuart, 2005). This technique also provides detailed and continuous spectra, covering a wide measurement range.

The studies of Hezel & Ross (1966), Begun et al. (1981), Silva et al. (2006), and Heuser et al. (2014) on the vibrational spectra of synthetic anhydrous REE-orthophosphate compounds ( $[\text{REE}]\text{PO}_4$ ) yield similar results on the change of the spectral features toward different REEs. The studies show the subtle shifts in spectral features toward higher wavenumber (lower wavelength) as the atomic number of REEs increases. This trend corresponds to the effect of lanthanide contraction, which involves a subtle decrease in the size of ionic radii of REEs with an increasing atomic number (Bart, 2023) (Table 1.1). The same trend can also be observed in other synthetic inorganic REE compounds, such as REE-orthoniobates ( $[\text{REE}]\text{NbO}_4$ ) (Pradhan & Choudhary, 1987) and REE-aluminium garnets ( $[\text{REE}]_3\text{Al}_5\text{O}_{12}$ ) (Papagelis & Ves, 2003).

Atomic no.	Symbol	Name	Ionic radii (Å) (CN = 9)	
57	La	Lanthanum	La <sup>3+</sup>	1.216
58	Ce	Cerium	Ce <sup>3+</sup>	1.196
59	Pr	Praseodymium	Pr <sup>3+</sup>	1.179
60	Nd	Neodymium	Nd <sup>3+</sup>	1.163
61	Pm	Promethium	Pm <sup>3+</sup>	1.144
62	Sm	Samarium	Sm <sup>3+</sup>	1.132
63	Eu	Europium	Eu <sup>3+</sup>	1.120
64	Gd	Gadolinium	Gd <sup>3+</sup>	1.107
65	Tb	Terbium	Tb <sup>3+</sup>	1.095
66	Dy	Dysprosium	Dy <sup>3+</sup>	1.083
67	Ho	Holmium	Ho <sup>3+</sup>	1.072
68	Er	Erbium	Er <sup>3+</sup>	1.062
69	Tm	Thulium	Tm <sup>3+</sup>	1.052
70	Yb	Ytterbium	Yb <sup>3+</sup>	1.042
71	Lu	Lutetium	Lu <sup>3+</sup>	1.032

**Table 1.1** Effective ionic radii of lanthanide (III) ions with coordinate number = 9 (Shannon, 1976)

## 1.2. Problem statement

Although there are several studies on TIR spectra of synthetic REE-bearing compounds in the field of material science, these studies usually focus on theoretical aspects by reporting band assignment of fundamental vibration modes of the mineral and exploring the relationship between the shifts of the vibration bands and the effect of lanthanide contraction of different REE. However, the practical application of this knowledge is still lacking. Therefore, this study aimed to address this gap by focusing more on practical aspects, expecting to improve the ability to estimate the relative abundance of REE in host minerals using TIR spectra which could potentially contribute novel insights to the field of spectral geology.

The objective of this study is to establish a fundamental understanding of how REEs influence the TIR spectra of the host minerals, specifically the spectral features regarding the fundamental vibrations of the host minerals, by conducting a detailed analysis on the changes in spectral features of the TIR spectra of REE-bearing minerals. Due to the simpler synthesis procedure, this study primarily focused on monazite, an anhydrous phosphate mineral which is considered as one of the primary sources of LREEs. In order to simplify the chemical and mineralogical complexities of the mineral, laboratory-synthesized monazite samples were used. This allowed for precise control over the chemical composition and complexity of the mineral, allowing for easier observation of how REEs influence the TIR spectra of the host mineral.



### **1.3. Research objective**

#### **1.3.1. Main objective**

Analyzing the influence of rare earth elements on the TIR spectra of laboratory-synthesized monazites to assess the feasibility of estimating the relative abundance of REEs in their natural occurrences.

#### **1.3.2. Sub-objectives**

1. Understanding how single-REE influences the spectral features of TIR spectra of monazites using laboratory-synthesized samples
2. Understanding how multi-REE influences the spectral features of TIR spectra of monazites using laboratory-synthetic samples
3. Assessing the feasibility of estimating the relative abundance of REEs from TIR spectra of naturally occurring monazites

### **1.4. Research questions**

1. What are the diagnostic spectral features of TIR spectra of monazite?
2. How do different REEs impact the shape, intensity, and position of the spectral features in the TIR spectra of single-REE monazites?
3. Which specific features in the TIR spectra of monazites can be used to distinguish each specific REE?
4. What is the relationship between the change of the spectral features and the atomic properties of each specific REE?
5. How could the presence of multi-REE impact the shape, intensity, and position of the spectral features of the TIR spectra of monazite?
6. How do the spectral features of monazite change toward the changes of REE ratios in the mineral?
7. What are the similarities and differences between TIR spectra of laboratory-synthesized and naturally occurring monazite?
8. Which specific spectral features in TIR spectra can be useful for distinguishing the species and proportion of REEs in natural minerals?
9. How does the difference variation of REE in the natural mineral impact the spectral behaviour of monazite?

### **1.5. Thesis structure**

#### **Chapter 1 Introduction:**

Introducing the background, problem statement, research objective, and research questions

#### **Chapter 2 Dataset and Methodology:**

Describing the dataset and elaborating the methodology used in this study

#### **Chapter 3 Results: The Synthesized Products**

Describing the synthesized products and presenting product characterization results

#### **Chapter 4 Results: TIR Spectra of Synthetic Monazites**

Displaying the TIR spectra of synthetic monazites and presenting feature extraction results

#### **Chapter 5 Discussion:**

Discussing on the methodology, results, and the application on natural monazite samples

#### **Chapter 6 Conclusion and Recommendations**

## 2. DATASET AND METHODOLOGY

This chapter provides a detailed description of the dataset and the methodology used in this study, covering the experimental procedure for monazite synthesis, sample characterization and validation methods, and the techniques used for TIR spectra acquisition and spectral analysis. The experimental process and data acquisition were conducted using the instruments and laboratory facilities in the GeoScience Laboratory at the Faculty of ITC, University of Twente.

### 2.1. Dataset

Two sets of laboratory-synthesized monazite for 20 samples in total, including ten single-REE monazites and ten double-REE monazites, were used in this study. Although both sample sets were synthesized using the same experimental procedure under controlled laboratory conditions, each set was prepared by a different experimenter at different times. A summary of the laboratory-synthesized samples in each sample set is provided in Table 2.1.

- **Sample Set 1** was synthesized as part of the work of Dijkstra et al. (2024). This set consists of seven samples of single-REE monazites (REE = La, Ce, Pr, Nd, Sm, Eu, and Gd).
- **Sample Set 2** was explicitly synthesized for this study. This set includes three samples of single-REE monazites (REE = La, Nd, and Sm) and two series of double-REE monazites (REE = La, Nd, and La, Sm). Each double-REE series consists of five samples with varying molar ratios of the two REEs, including 10:90, 25:75, 50:50, 75:25, and 90:10.

Set	Type	Composition	Formula	Experiment	
1	Single-REE	La	LaPO <sub>4</sub>	Dijkstra et al. (2024)	
		Ce	CePO <sub>4</sub>		
		Pr	PrPO <sub>4</sub>		
		Nd	NdPO <sub>4</sub>		
		Sm	SmPO <sub>4</sub>		
		Eu	EuPO <sub>4</sub>		
		Gd	GdPO <sub>4</sub>		
2	Single-REE	La	LaPO <sub>4</sub>	<i>This study</i>	
		Nd	NdPO <sub>4</sub>		
		Sm	SmPO <sub>4</sub>		
	Double-REE	La, Nd			(La <sub>0.90</sub> , Nd <sub>0.10</sub> )PO <sub>4</sub>
					(La <sub>0.75</sub> , Nd <sub>0.25</sub> )PO <sub>4</sub>
					(La <sub>0.50</sub> , Nd <sub>0.50</sub> )PO <sub>4</sub>
					(La <sub>0.25</sub> , Nd <sub>0.75</sub> )PO <sub>4</sub>
					(La <sub>0.10</sub> , Nd <sub>0.90</sub> )PO <sub>4</sub>
		La, Sm			(La <sub>0.90</sub> , Sm <sub>0.10</sub> )PO <sub>4</sub>
					(La <sub>0.75</sub> , Sm <sub>0.25</sub> )PO <sub>4</sub>
					(La <sub>0.50</sub> , Sm <sub>0.50</sub> )PO <sub>4</sub>
					(La <sub>0.25</sub> , Sm <sub>0.75</sub> )PO <sub>4</sub>
			(La <sub>0.10</sub> , Sm <sub>0.90</sub> )PO <sub>4</sub>		

**Table 2.1** Summary table of laboratory-synthesized monazite samples used in this study

## 2.2. Experimental method for monazite synthesis

The method for synthesizing REE-bearing monazites in this study closely followed the protocol outlined by Dijkstra et al. (2024), with slight adjustments. In this synthesis route, rhabdophane, a hydrous orthophosphate ( $[\text{REE}]\text{PO}_4 \cdot n\text{H}_2\text{O}$ ), was used as a precursor for synthesizing a monazite. Initially, rhabdophane was prepared through wet precipitation by using REO ( $[\text{REE}]_2\text{O}_3$ ) and orthophosphoric acid ( $\text{H}_3\text{PO}_4$ ) as starting materials. Later, high-temperature thermal treatment was applied to the synthetic rhabdophane, transforming the mineral into monazite, an anhydrous orthophosphate ( $[\text{REE}]\text{PO}_4$ ). The summary of materials used for synthetic experiments is provided in Table 2.2.

Name	Formula	Supplier	Remark
Lanthanum (III) oxide	$\text{La}_2\text{O}_3$	Strategic Elements	> 99.9% purity
Neodymium (III) oxide	$\text{Nd}_2\text{O}_3$	Strategic Elements	> 99.9% purity
Samarium (III) oxide	$\text{Sm}_2\text{O}_3$	Strategic Elements	> 99.9% purity
Orthophosphoric acid	$\text{H}_3\text{PO}_4$	Merck Emsure	85% concentrated
Ultrapure water	$\text{H}_2\text{O}$	Millipore	> 18.2 M $\Omega$ , 25 °C

**Table 2.2** Information of materials used for synthesizing monazites

Additionally, the preparation procedure for monazite synthesis in this study can be achieved by following this detailed protocol:

1. Calcine the REO powder at 650 °C in a conventional muffle furnace for 20 hours to remove impurities and volatile substances in the oxide powder.
2. Calculate the required amount of the calcined REO powder to achieve the desired mole of REE in the final monazite products. Then, weigh out the powder using a high-precision analytical balance. The amount of REO powder can be calculated using the following equation:

$$mass_{REO} (g) = \frac{mole_{REE} (mol) \times Molar\ mass_{REO} (g/mol)}{2}$$

In this study, the target amount of REE was set at 0.005 mol for all single-REE monazite samples. Similarly, for double-REE monazites, the total amount of REE was also set at 0.005 mol per sample. However, the molar ratio between two REEs was set to be varied across the samples, resulting in different mole quantities for each REE in every sample (Table 2.3). The mass of REO for synthesizing each sample in this study is shown in *Appendix I*.

Molar ratio	10:90	25:75	50:50	75:25	90:10
$mol_{REE1}$	0.00050	0.00125	0.00250	0.00375	0.00450
$mol_{REE2}$	0.00450	0.00375	0.00250	0.00125	0.00050
<b>Total <math>mol_{REE}</math></b>	0.00500	0.00500	0.00500	0.00500	0.00500

**Table 2.3** Mole quantities of each REE in double-REE monazite samples

3. Start preparing rhabdophane by filling a glass beaker with a small amount of water and adding the prepared REO powder. Stir the mixture continuously at room temperature with magnetic

stirring until the powder is completely dissolved and the solution becomes clear. Next, add 27.0 ml of concentrated  $\text{H}_3\text{PO}_4$  acid into the beaker and carefully add ultrapure water until the solution reaches a total volume of 210 ml. Then, heat the solution on a hotplate to 215 °C while vigorously stirring the solution, and cover the beaker with a watch glass to prevent evaporation. After the solution starts to boil, leave the solution boiling and stirring for 1.5 hours. During this process, the rhabdophane will begin to form and can be observed as a cloudy suspension in the solution.

4. Once the boiling process is complete, turn off the heat plate and remove the stirrer magnet. Then, wait for the solution to cool down for approximately 30 minutes. During this period, the rhabdophane suspension will settle at the bottom of the beaker. Then, carefully pour the clear aqueous solution out of the beaker, wash the remaining rhabdophane with ultrapure water, and transfer the product into a centrifuge tube. To get rid of the remaining  $\text{H}_3\text{PO}_4$  acid, centrifuge and wash the rhabdophane at least three times until the pH of the material becomes neutral (around pH 5.5 – 6). After that, transfer the rhabdophane to a ceramic evaporating dish and leave the product overnight in a fume hood until the product dries.
5. Once the rhabdophane is completely dry, gently remove the powder from the ceramic dish and transfer the material to a porcelain ceramic crucible. Then, place the crucible into a conventional muffle furnace and heat it at 800 °C for 6 hours in the air. During this high thermal treatment process, the rhabdophane will transform into monazite.

### 2.3. Sample characterization and validation methods

The final products obtained from the synthesis experiments were validated for their monazite structure through powder X-ray diffraction (pXRD) analysis. Furthermore, VNIR-SWIR reflectance spectroscopic analysis was conducted to confirm the presence of REE in the products.

#### 2.3.1. Powder X-ray diffraction analysis

The synthesized product powders were used for pXRD analysis to characterize their mineral structure and acquire crystallographic information. The measurements were conducted with a Bruker D2 Phaser diffractometer with a  $\text{Cu-K}\alpha$  X-ray source ( $\lambda = 1.5405 \text{ \AA}$ ). Before placing the powder into a standard PMMA sample holder, the product must be hand-grounded in an agate mortar to break down large aggregate clumps, resulting in a homogeneously fine-grained powder.

For the measurement setup, the diffractometer was equipped with a 0.6 mm source slit, 1 mm knife, and 8 mm detector slit. The data were collected by integrating ten repeated scans over  $2\theta$  range  $6 - 60^\circ$  with a step size of  $0.012^\circ$  and a time step of 0.1 seconds. The total runtime to complete a full measurement per sample was approximately 1.2 hours. After completing each measurement, the XRD pattern was manually compared with the reference pattern from the database in DIFFRAC.EVA software to preliminarily confirm that the products were completely transformed into monazite without any remaining REO and  $\text{H}_3\text{PO}_4$  residuals left in the samples.

In addition, the acquired XRD data were also used to perform a structural refinement analysis to extract the crystallographic information of the monazite samples. The refinement was conducted in MAUD, the Rietveld refinement software. Before starting the refinement, the crystallographic information file (CIF) of monazite-(La) from Ni et al. (1995) (COD ID 9001647), accessible for download from the Crystallography

Open Database (2024), was used as an initial phase for generating the compute structural model. The refinement was performed in the selected region, from the  $2\theta$  range between  $16 - 60^\circ$ , to ignore the influence of the amorphous sample holder in the low  $2\theta$  angle. The refinement results provided essential crystallographic information about the products, such as unit cell parameters, cell volume, and bond lengths, which were later used in further analyses.

### 2.3.2. VNIR-SWIR reflectance spectroscopic analysis

Since almost trivalent form of every REE shows unique diagnostic absorption patterns in the VNIR-SWIR range of the electromagnetic spectrum, the VNIR-SWIR reflectance spectroscopic analysis was used to validate the presence of REE in the synthetic samples. The study was conducted using the ASD Fieldspec 3 spectrometer, equipped with a pistol grip, to acquire the VNIR-SWIR spectra of the samples from the wavelength range  $350 - 2500$  nm. The spectra measurements were taken in the darkroom using a quartz-tungsten-halogen lamp (ASD Illuminator reflectance lamp) as a light source.

The measurements were performed on compacted powder samples (with approximately 1 mm thickness) placed on a circular flat glass. Five measurements were taken for each sample. Before taking measurements of every sample, a white reference panel (Spectralon™) was measured to convert radiance to reflectance values. After finishing the measurements, splice correction was applied to smoothly connect the spectra between the VNIR and SWIR ranges. Then, the spectra were exported in ASCII file format. All the spectra of each sample were averaged after checking the consistency of the spectral features. Finally, the averaged spectra were compared with the reference spectra of single-REE monazite from Dijkstra et al. (2024) (Figure 2.1) to confirm the presence of REEs in the samples.

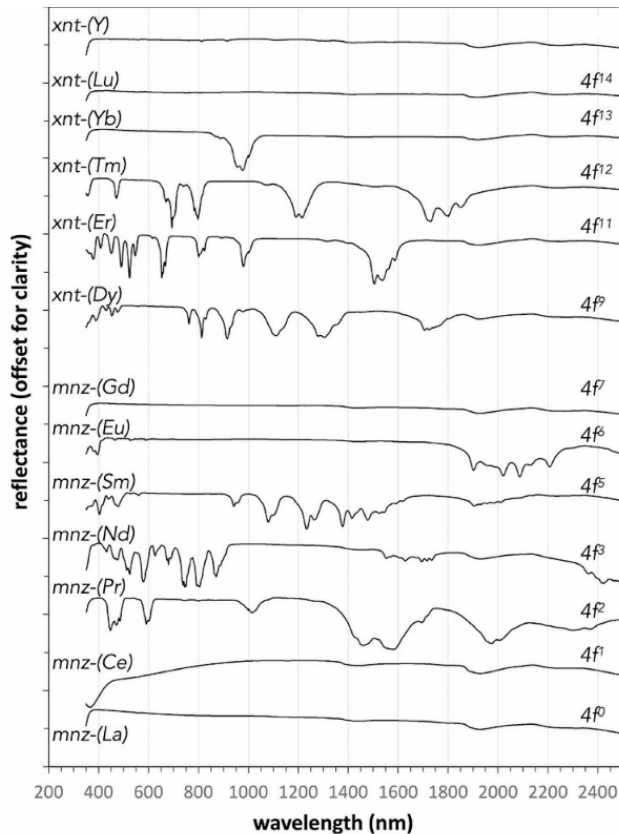


**Figure 2.1** The VNIR-SWIR reflectance spectra of single-REE phosphates minerals, including monazites (mnz) (Dijkstra et al., 2024)

## 2.4. TIR spectra analytical method

Once it was confirmed that the obtained products were the desired REE-bearing monazite, the samples were taken to collect their TIR spectra to fulfill the study's objective. Fourier transform infrared (FTIR) spectroscopy was used to acquire the spectra. The FTIR spectroscopy analysis is widely used to study vibrational spectra of the materials in the TIR range due to its capability to capture a broad range of infrared spectra, fully covering the fundamental vibrations region of many REE-host minerals, including monazite, which is the primary focus of this study. Moreover, the advantage of moving mirrors of the interferometer within the FTIR spectrometer allows the adjustment of spectral resolution, providing the ability to obtain highly detailed TIR spectra, which is essential for examining the influence of REEs toward the spectral features of the host minerals.

There are several techniques for acquiring the infrared spectra in FTIR spectroscopy. The most common technique is transmission-FTIR, which is widely used in many fields, including chemistry, geology, and material science (Chen et al., 2015). This technique requires the preparation of a traditional potassium bromide (KBr) pellet by mixing the sample with KBr powder. Preparing these pellets requires significant experience to estimate the appropriate amounts of sample and KBr powder, which can lead to variations in the spectral features obtained (Surovell & Stiner, 2001).

Therefore, attenuated total reflectance (ATR)-FTIR was selected to be used in this study due to its suitability for analyzing powdered samples. This technique is time-efficient, needs only a small amount of sample, and does not require complex sample preparation. This can minimize the cause of spectra variation from the sample preparation (Thompson et al., 2009). The ATR-FTIR also yields high-quality spectra with a good signal-to-noise ratio. Additionally, Beasley et al. (2014) suggested that ATR-FTIR can be an effective alternative to traditional transmission FTIR.

Unlike the traditional transmission technique, the infrared (IR) beam in the ATR technique does not transmit directly through the sample. Instead, the ATR technique works by utilizing the total internal reflection phenomena when the IR incident beam enters a high-refractive-index crystal at an angle of incident greater than the critical angle. The IR beam reflects internally within the crystal and creates an evanescent wave at the point of internal reflection between the crystal and the sample. The evanescent wave penetrates a few micrometers into the sample, interacting with the sample and absorbing specific regions of the IR spectrum. The remaining IR radiation is then detected, producing an ATR spectrum of the sample (Figure 2.2) (Müller et al., 2014; Stuart, 2004).

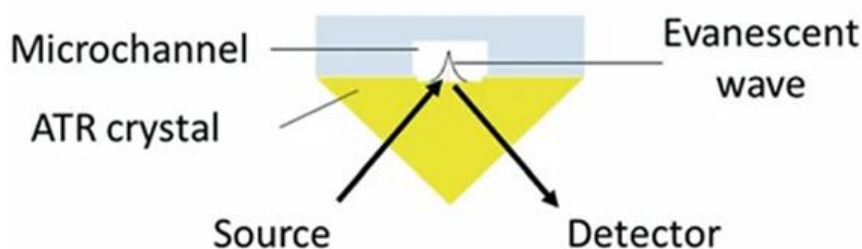


**Figure 2.2** A schematic diagram showing how ATR-FTIR works (Eid, 2022)

### 2.4.1. TIR spectra acquisition

The TIR spectra measurements were conducted using a Bruker Vertex 70 FTIR spectrometer mounted with a Platinum-ATR diamond accessory. The spectrometer was equipped with a DLaTGS detector, a KBr beamsplitter, and an external globar source, providing the ability to obtain a continuous spectrum over a wide range of  $7500 - 370 \text{ cm}^{-1}$  ( $1.33 - 27.03 \text{ }\mu\text{m}$ ). The OPUS software was used to operate the data acquisition, configure the measurement setup, and perform the Fourier transformation. The spectra were recorded in transmission mode within the range of  $4000 - 370 \text{ cm}^{-1}$  with a spectral resolution of  $2 \text{ cm}^{-1}$  and 128 scans per measurement.

For each sample, at least three spectral measurements were taken, using  $0.004 \text{ g}$  of powder for each measurement. Before recording the spectra of each sample, background scanning was performed on an empty ATR channel to eliminate the background effect on the resulting spectra. Then, the sample spectra were recorded by placing the sample powder to cover the ATR channel and gently closing the pressure arm to prevent the powder from spreading away from the channel. After recording all three spectra of each sample, the spectra were manually checked for consistency in shape, intensity, and feature positions. Additionally, the spectra of each sample were compared with those of the different samples. If any abnormalities were observed in the spectra, additional spectra of the following sample were re-recorded to ensure the accuracy of the spectral features.

After completing the measurements, the spectra were exported in Opus file format. Subsequently, the data were converted to Envi spectra library (.sli) file format using HypPy software (Bakker, 2024). Then, the mean spectra of each sample were calculated and saved. Finally, every resulting spectrum, including the mean spectra of each sample, was converted to absorbance mode using the following equation based on Beer-Lambert law (Stuart, 2004):

$$\text{Absorbance} = -\log(\text{Transmittance})$$

After the conversion, the shape and position of the spectral features were preserved. However, this transformation caused the spectra to invert vertically, making the transmission minima become absorbance maxima. Additionally, the conversion impacted the spectral intensity, in which absorbance spectra have a stronger spectral intensity than transmittance spectra (Figure 2.3).

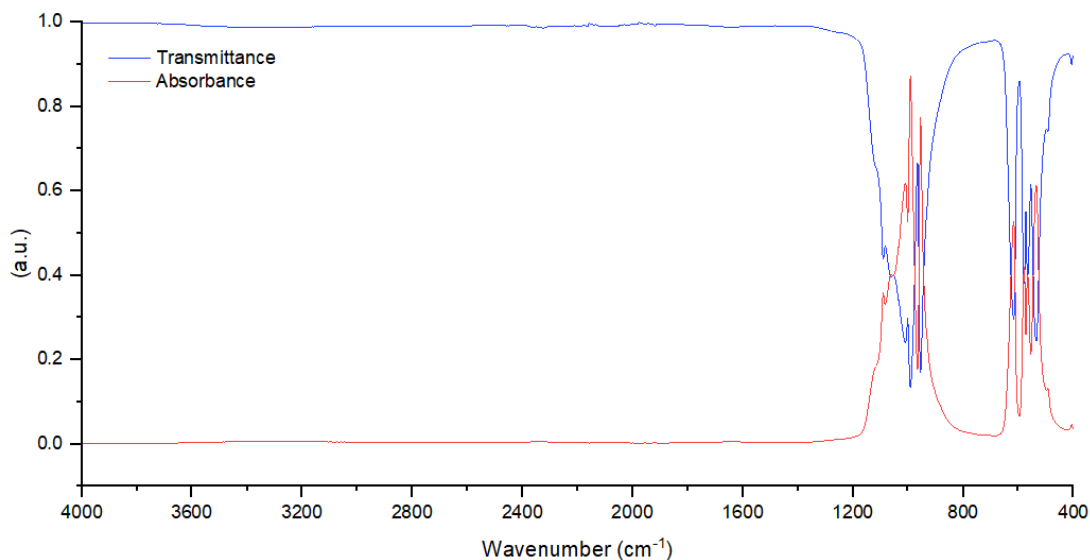


**Figure 2.3** The comparison between transmittance and absorbance spectrum

### 2.4.2. Spectral feature analysis

After obtaining the TIR spectra for each sample, spectral feature analysis was conducted. Initially, the overall spectra of all samples were reviewed and compared with existing data on the vibrational band positions of monazite from previous literature. Subsequently, the wavenumber positions and spectral feature intensities of all minima and maxima features in the spectra were extracted. This data was then used to analyze the relationship between spectral changes toward different REE compositions in the monazites.

The information derived from single-REE spectra was used as reference data to predict how multi-REE impacts monazites' TIR spectra. In the multi-REE samples, the correlation between the changes in the spectral features and difference ratio and variation of REE content will be analyzed. This information will be used as baseline knowledge to understand how REE could possibly influence the TIR spectra of natural monazite.

### 2.4.3. Spectral feature extraction

The spectral feature extraction was performed using interpolated local extrema (minima and maxima) functions in HypPy software to reduce bias from manually selecting the minima and maxima points in the spectra. These functions utilize a second-degree polynomial fitting method, which involves fitting a parabolic curve through three consecutive data points of the spectral bands. This process begins by selecting the extrema point, which has the highest or lowest spectral intensity (the extrema point) in the spectra, and the two adjacent points. By applying a parabolic fit, the vertex of the resulting parabola represents the interpolated local extrema. This vertex provides information on both the position (in wavenumber,  $\text{cm}^{-1}$ ) and absorbance intensity (in absorbance unit, a.u.) of the spectral feature (Figure 2.4). This feature extraction approach has been proven to be highly accurate in identifying the actual position of absorption minima in hyperspectral reflectance spectra (Van Ruitenbeek et al., 2014), which is helpful in observing the slight shift in the spectral features.

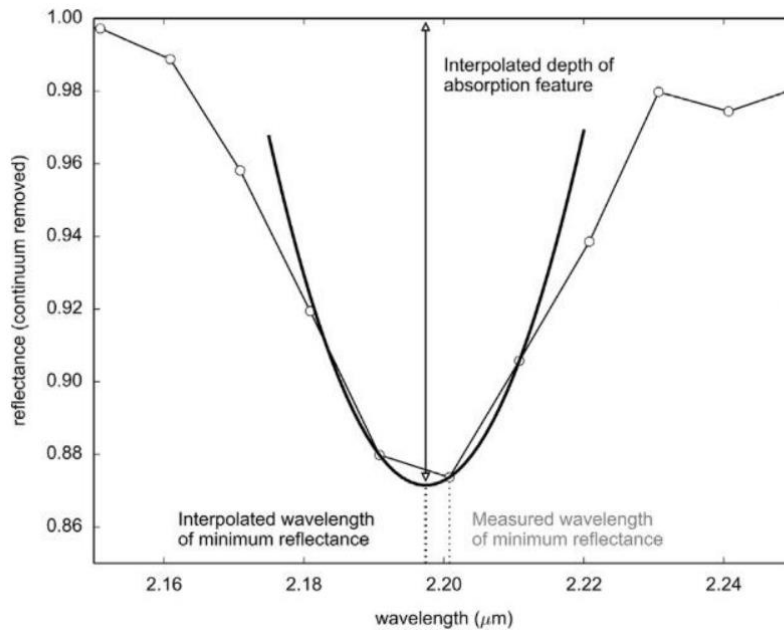


**Figure 2.4** The calculation of an interpolated local minima using the second-degree polynomial fitting method (Van Ruitenbeek et al., 2014)



### 3. RESULTS: THE SYNTHESIZED PRODUCTS

This chapter describes the results of the products from Sample Set 2 obtained from the synthesis experiments in this study. The results of their characterization and validation from pXRD and VNIR-SWIR reflectance spectroscopy analysis are also presented and described.

#### 3.1. The synthesized monazite products

The powder products obtained from the synthesis experiment exhibited different colours based on their REE compositions (Figure 3.1). For single-REE products, the colour of La was white in natural light, Nd was pinkish white, and Sm was yellowish white. For double-REE products, the colour of the samples was graded and became more intense as the content of Nd and Sm increased. Additionally, the colours of the synthesized products from this study were similar to those of single-REE monazites in the Sample Set 1 from the synthesis experiment of Dijkstra et al. (2024) (Figure 3.2).

Moreover, it was observed that the La and Nd powder products tended to form coarser particles compared to the Sm powders. This was similar to the products from Sample Set 1, where La, Ce, Pr, and Nd monazite had relatively coarse particles, while Sm, Eu, and Gd monazite had relatively fine particles. In absence of any data from quantitative methods to assess particle sizes such as electron microscopy, it is hard to provide a more detailed analysis of the (relative) particle sizes and size distributions.

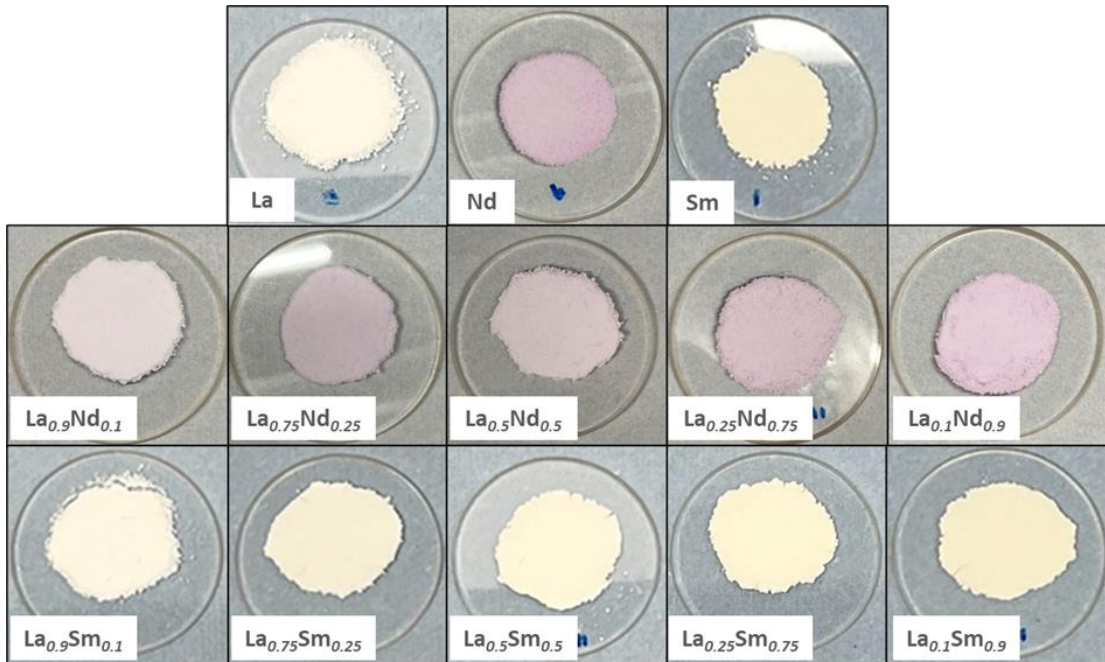


Figure 3.1 The single and double-REE powder products obtained from the synthesis experiment

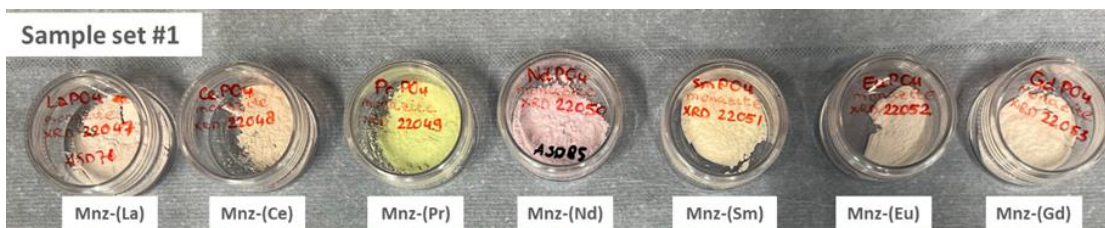


Figure 3.2 Single-REE monazites from the Sample Set 1

The percent yields, calculated based on the total amount of mole REE in the final products compared to the starting solution used for synthesizing the precursor product, show that the average yield of REE in final product is 89.40% with the minimum yield of 77.14% maximum yield of 95.52% (Table 3.1). Generally, yields greater than 95% could indicate minimal fractionation between La, Nd, and Sm during the synthesis, suggesting that the REE composition of the final products remains similar to the starting solution. However, the yields obtained in this study is lower 95% due to losses during the synthesis process. These losses occurred mainly when removing precipitation products from the centrifuge tubes and transferring materials between containers. Therefore, the actual yields in this study are likely higher than the calculated values. However, the fractionation was further confirmed by using the results of structural refinement in the XRD analysis. The refinement results suggest that there is no fractionation within the final products, as presented in the next subsection.

Product	Total mole REE (as prepared)	Total mole REE (final product)	% Yield
<b>Single-REE</b>			
LaPO <sub>4</sub>	0.00500	0.00407	81.42
NdPO <sub>4</sub>	0.00500	0.00386	77.14
SmPO <sub>4</sub>	0.00500	0.00474	94.73
<b>Double-REE: (La<sub>1-x</sub> Nd<sub>x</sub>)</b>			
(La <sub>0.10</sub> Nd <sub>0.90</sub> )PO <sub>4</sub>	0.00500	0.00446	89.26
(La <sub>0.75</sub> Nd <sub>0.25</sub> )PO <sub>4</sub>	0.00500	0.00456	91.21
(La <sub>0.50</sub> Nd <sub>0.50</sub> )PO <sub>4</sub>	0.00500	0.00438	87.62
(La <sub>0.25</sub> Nd <sub>0.75</sub> )PO <sub>4</sub>	0.00500	0.00421	84.21
(La <sub>0.90</sub> Nd <sub>0.10</sub> )PO <sub>4</sub>	0.00500	0.00454	90.82
<b>Double-REE: (La<sub>1-x</sub> Sm<sub>x</sub>)</b>			
(La <sub>0.10</sub> Sm <sub>0.90</sub> )PO <sub>4</sub>	0.00500	0.00437	87.49
(La <sub>0.75</sub> Sm <sub>0.25</sub> )PO <sub>4</sub>	0.00500	0.00472	94.37
(La <sub>0.50</sub> Sm <sub>0.50</sub> )PO <sub>4</sub>	0.00500	0.00478	95.52
(La <sub>0.25</sub> Sm <sub>0.75</sub> )PO <sub>4</sub>	0.00500	0.00465	93.04
(La <sub>0.90</sub> Sm <sub>0.10</sub> )PO <sub>4</sub>	0.00500	0.00477	95.40

**Table 3.1** List of the amount of total REE (in mol) in the starting solution as prepared for synthesizing the precipitation product (precursor) and in the final product obtained after thermal treatment. The percent yield indicates the relative proportions of REE the final product compared to the starting solution for each product.

### 3.2. Structural characterization from pXRD analysis

The results from pXRD analysis allowed the identification and confirmation of mineral phases of the obtained synthesized products. Additionally, crystallographic information of the synthesized products was obtained through structural refinement of the XRD data.

#### 3.2.1. Phase identification

The XRD patterns reveal that the product obtained from the precipitation method was characterized as a single-phase rhabdophane with a hexagonal structure (Kijkowska et al., 2003; Clavier et al., 2018). After heating the products to 800° for 6 hours, the rhabdophane was completely recrystallized and transformed into a single-phase monazite with a monoclinic structure (Figure 3.3). The XRD results confirm that all final products from the synthesis experiments in this study were characterized as monazite (Figure 3.4).

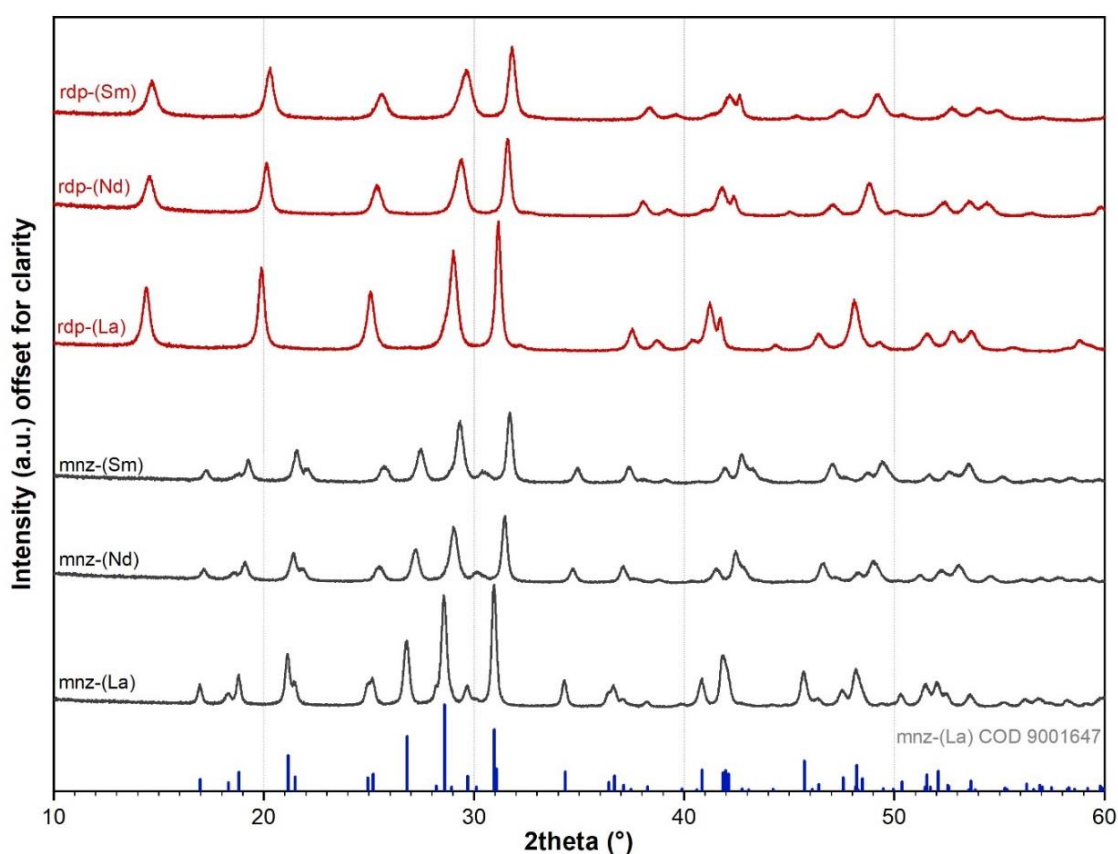


**Figure 3.3** The XRD patterns of single-REE products from the experimental synthesis in this study (REE = La, Nd, and Sm). The products from precipitation method were characterized as rhabdophane (rdp). The products obtained after thermal treatment were characterized as monazite (mnz). The reference XRD peak positions of monazite-(La) from Ni et al. (1995) (COD ID 9001647) are shown as blue vertical bars.

For single-REE monazites, systematic shifts of the XRD peaks towards higher  $2\theta$  angles can be observed as the atomic number of the REE increases. Similar observations were found in the XRD results of single-REE monazites from Sample Set 1 (see Appendix II). These peak shifts correspond to the effect of the lanthanide contraction, where the ionic radii of REEs gradually decrease with increasing atomic number. This reduction in ionic radii leads to smaller d-spacing of the crystal planes, resulting in higher  $2\theta$  angles.

Additionally, systematic XRD peaks shift can be observed in double-REE monazite samples. From Figure 3.4, it can be seen that the monazite peaks shift toward higher  $2\theta$  angles as the content of Nd and Sm in the products increase (Figure 3.4).

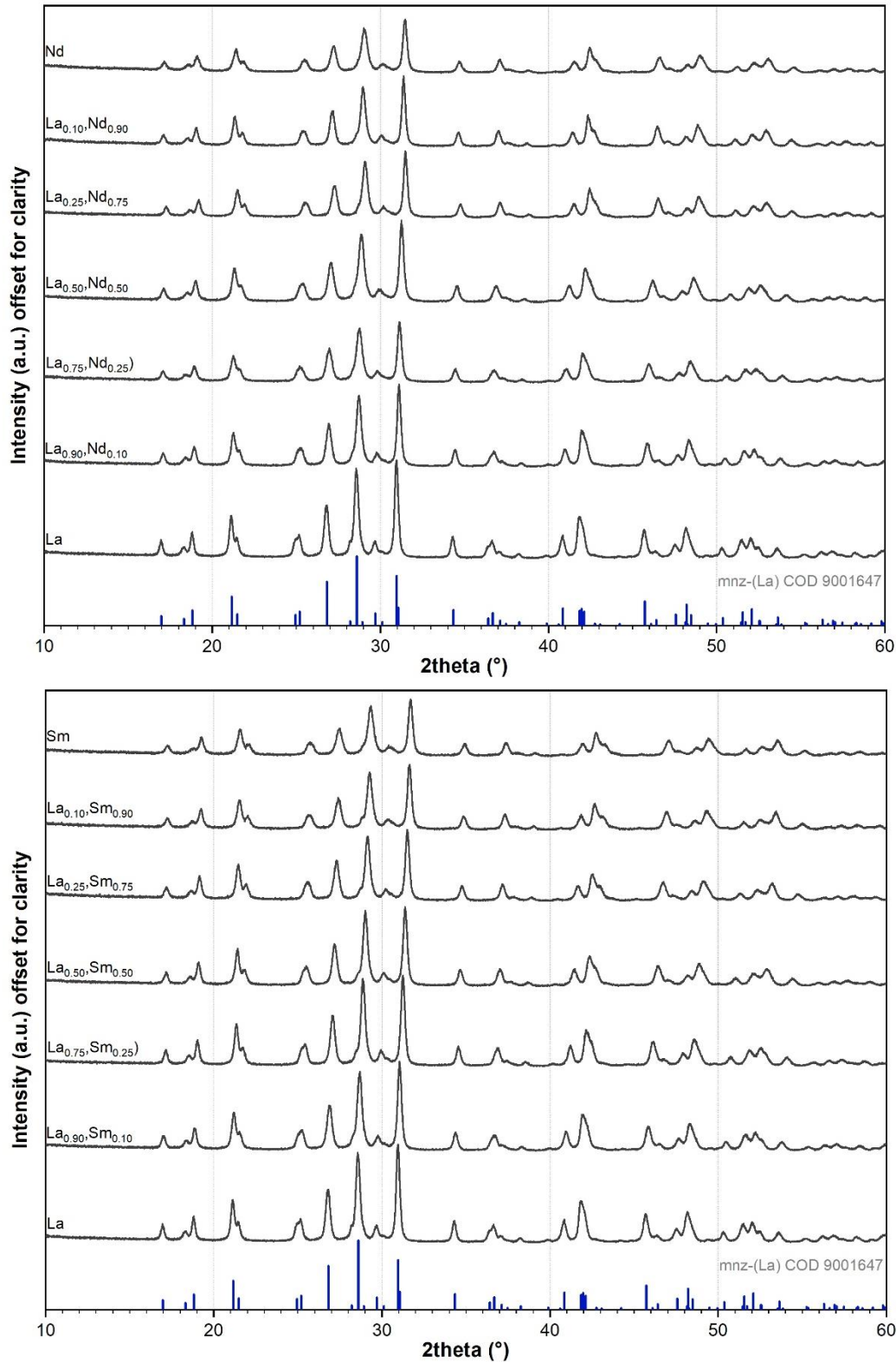


**Figure 3.4** The XRD patterns of double-REE monazite synthesized in this study (**Top**) REE =  $\text{La}_{1-x}\text{Nd}_x$  (**Bottom**) REE =  $\text{La}_{1-x}\text{Sm}_x$ . The reference XRD peak positions of monazite-(La) from Ni et al. (1995) (COD ID 9001647) are shown as blue vertical bars.

### 3.2.2. Structural refinement

The results of Rietveld refinement of the XRD data reveal detailed crystallographic information of the obtained monazite products, including unit cell parameters ( $a$ ,  $b$ ,  $c$ , and  $\beta$  angle) and cell volume (see *Appendix III*). The obtained unit cell parameters for the single-REE monazites synthesized in this study closely match the values from Sample Set 1 (see *Appendix II*), with differences of less than 0.02% (mean 0.01%).

The unit cell parameters obtained from the refinement show an increase in unit cell dimensions ( $a$ ,  $b$ ,  $c$ ) when an atomic number of REE increases (i.e., ionic radii decreased) in single-REE monazites, while the  $\beta$  angle shows a decrease. A similar trend is observed in double-REE monazites, where the increase of Nd and Sm content results in a systematic increase in unit cell dimensions and a decrease in the  $\beta$  angle (Figure 3.5). These linear trends confirmed that there is no significant fractionation during the synthesis of double-REE monazites, as described by Vegard's law. This law states that the unit cell parameters of a binary solid solution show a linear relationship with the concentration (molar fraction,  $x$ ) of the two end-members, assuming ideal mixing, and thus no significant fractionation occurs (Denton & Ashcroft, 1991).

Furthermore, the data reveal that the cell volume of the synthesized single-REE monazites decreases when the atomic number of REE increases (i.e., ionic radii decrease). The trend can also be observed in double-REE monazite products, obtained from the synthesis experiment in this study, where the cell volume decreases with increasing Nd and Sm content (Figure 3.6).

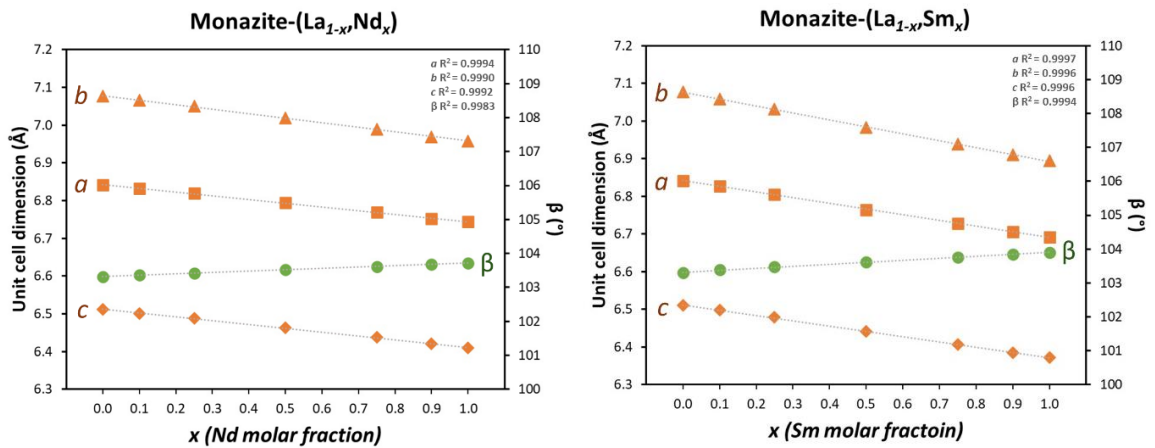


**Figure 3.5** Unit cell parameters of double-REE monazite synthesized in this study (**Left**) REE = La<sub>1-x</sub>Nd<sub>x</sub> (**Right**) REE = La<sub>1-x</sub>Sm<sub>x</sub>. The unit cell dimensions ( $a$ ,  $b$ ,  $c$ ) decrease linearly as the Nd and Sm molar fractions increase, while the  $\beta$  angle increases linearly

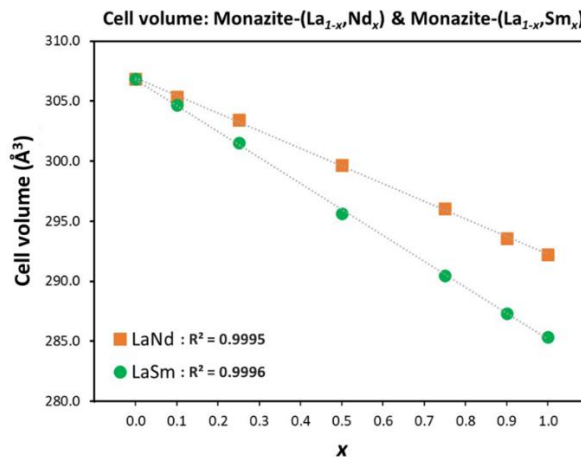


**Figure 3.6** Systematic decrease in cell volume as Nd and Sm content increases in double-REE monazites

### 3.3. REE validation from VNIR-SWIR reflectance spectroscopic analysis

The VNIR-SWIR reflectance spectra of the synthetic monazites, obtained from the experimental synthesis conducted in this study, were used to confirm the presence of REE in the monazite products. The comparison between the spectra of the obtained monazite products and the reference spectra of single-REE monazites from Sample Set 1, reported by Dijkstra et al. (2024) (Figure 2.1), reveals a close match in both position and shape of the absorption features (Figure 3.7). This match can be used to confirm that the final products consist of the desired REE. Additionally, it can be observed that an increase in Nd and Sm content in the products correlates with deeper absorption features of the Nd and Sm trivalent.

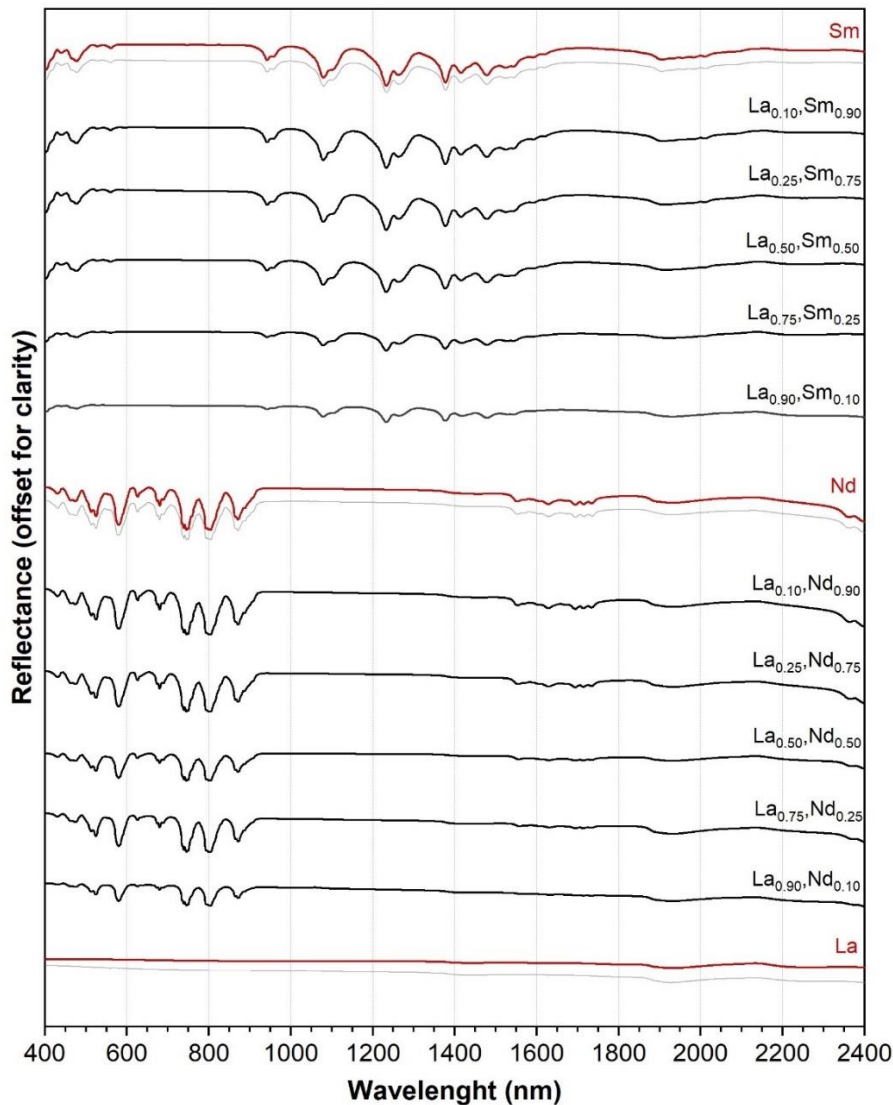


**Figure 3.7** Reflectance spectra in VNIR-SWIR range (400 – 2400 nm) of all monazite products from the synthesis experiment in this study. The red spectra represent single-REE monazite (REE – La, Nd and Sm). The light grey spectra below the each of the single-REE spectra are reference spectra from Sample Set 1, as reported in the publication by Dijkstra et al. (2024)

## 4. RESULTS: TIR SPECTRA OF SYNTHETIC MONAZITES

This chapter displays the results of TIR spectra, displayed in absorbance mode, of laboratory-synthesized monazites recorded using ATR-FTIR spectroscopy technique. These include spectra of single-REE (REE = La to Gd) from Sample Set 1 (synthesized during the work of Dijkstra et al., 2024) and single-REE (REE = La, Nd, and Gd) plus two series of double-REE monazites (REE =  $\text{La}_{1-x}\text{Nd}_x$  and  $\text{La}_{1-x}\text{Sm}_x$ ) from Sample Set 2 (synthesized in this study). Additionally, this chapter includes the results of local feature extractions obtained through second-degree polynomial fitting method.

### 4.1. TIR spectra of synthetic monazite

All obtained TIR spectra from  $4000 - 400 \text{ cm}^{-1}$  ( $2.5 - 25 \mu\text{m}$ ) of laboratory-synthesized monazites show significant absorbance intensity bands at wavenumber below  $1200 \text{ cm}^{-1}$  (Figure 4.1). The absorbance intensity of each repeated measurement spectrum recorded from the same samples shows minor deviation in some part of the strong-intensity regions (Figure 4.2). Detailed examination of each repeated measurement spectrum from the same samples revealed that, although the absorbance intensities varied, the positions of the local features (minima and maxima) remained relatively constant (less than  $0.64 \text{ cm}^{-1}$  differences). Based on the observation, these variations in absorbance intensity could be attributed to differences in the amount of sample powder in contact with the ATR crystal and the slight inconsistencies in force applied when closing the pressure arm of the ATR instrument. Therefore, the average spectra of each sample were used for further analysis.

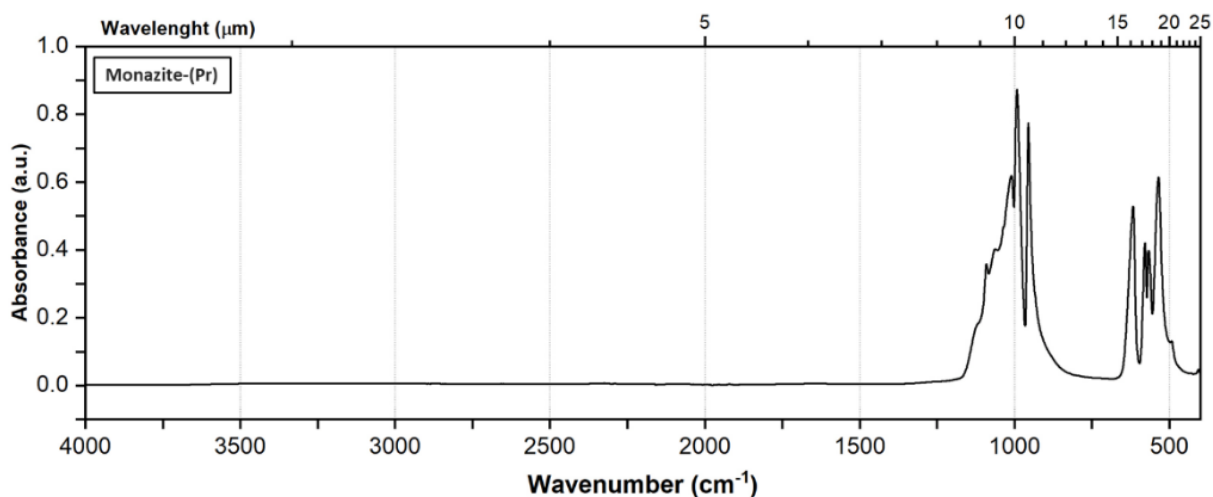


**Figure 4.1** Example TIR absorbance spectrum from wavenumbers  $4000 - 400 \text{ cm}^{-1}$  (wavelengths  $2.5 - 25 \mu\text{m}$ ) of synthetic monazite-(Pr)

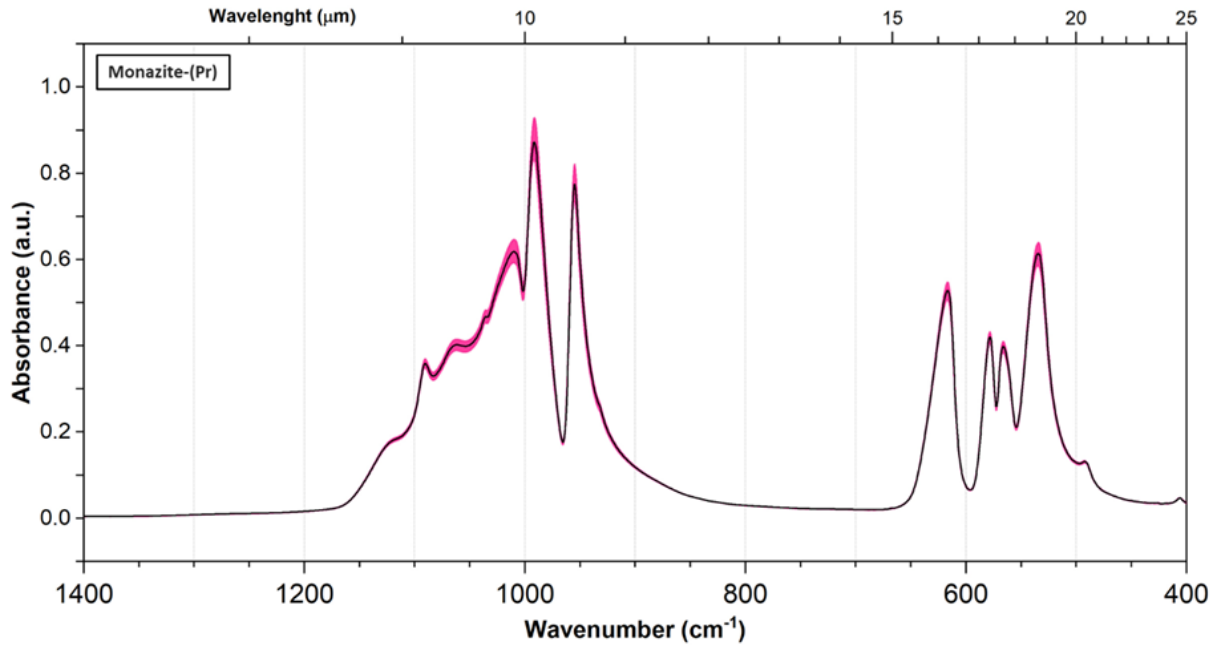


**Figure 4.2** Example TIR absorbance spectrum from wavenumbers 1400 – 400  $\text{cm}^{-1}$  (wavelengths 7.14 – 25  $\mu\text{m}$ ) of synthetic monazite-(Pr). The black line represents the average spectrum derived from three repeated spectra, while the pink area shows the minimum and maximum absorbance intensities from the repeated measurements.

#### 4.1.1. General characteristics of monazites spectral features in TIR range

In the region below 1200  $\text{cm}^{-1}$ , the spectra display two major strong intensity bands: the first between 1200 to 900  $\text{cm}^{-1}$  (8.33 – 11.11  $\mu\text{m}$ ) and the second between 700 to 475  $\text{cm}^{-1}$  (14.29 – 21.05  $\mu\text{m}$ ). These major bands correspond to the fundamental vibration frequencies of the  $\text{PO}_4$ -tetrahedra of the phosphate group within the monazite. The first band corresponds to the stretching mode ( $\nu$ ), while the second band corresponds to the bending mode ( $\delta$ ) (Clavier et al., 2018; J. Heuser et al., 2014) (Figure 4.3). The absorbance maxima (absorbance peaks) within the spectra can be assigned to the modes of fundamental vibrations of  $\text{PO}_4$ , following the band assignments reported by Hezel & Ross (1966).

In the TIR spectra of synthetic monazites in this study, the local features within the 1200 – 900  $\text{cm}^{-1}$  regions can be assigned to two modes of stretching ( $\nu$ ). The band corresponding to antisymmetric stretching ( $\nu_{\text{as}}$ ) is observed around 1120 – 980  $\text{cm}^{-1}$ , appearing as a broad band with small multiple local features. The band corresponding to symmetric stretching ( $\nu_{\text{s}}$ ) is observed as a narrow single band in the 970 – 950  $\text{cm}^{-1}$  region.

In the 700 – 475  $\text{cm}^{-1}$  region, the local features can be assigned to two modes of bending. The band corresponding to antisymmetric bending ( $\delta_{\text{as}}$ ) appears as a broad band with four distinct local features around 600 – 540  $\text{cm}^{-1}$ . The band corresponding to symmetric bending ( $\delta_{\text{s}}$ ) can be observed as a small single feature around 490  $\text{cm}^{-1}$ . Figure 4.2 summarizes the positions of the bands corresponding to each vibrational mode of  $\text{PO}_4$ .



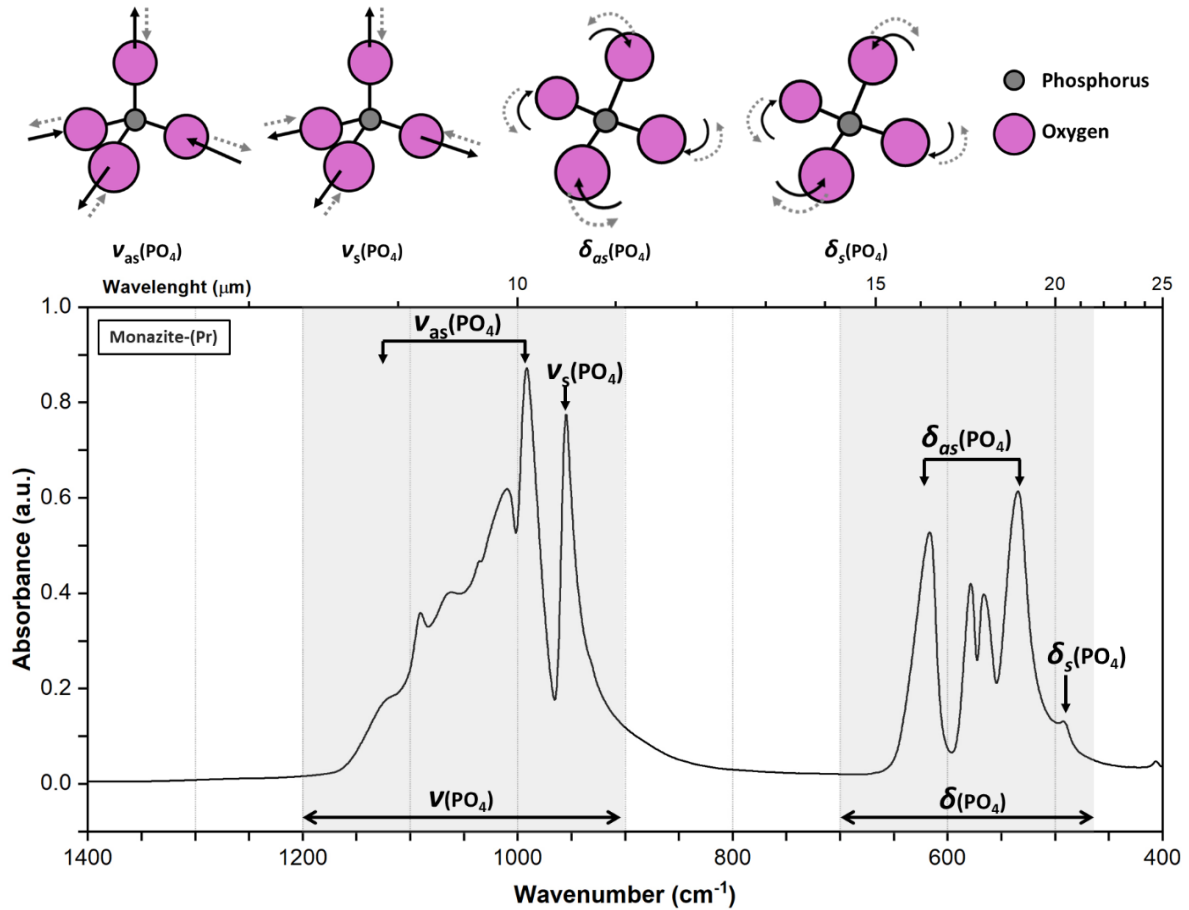


**Figure 4.3** TIR absorbance spectrum of synthetic monazite-(Pr) from wavenumbers 1400 – 400  $\text{cm}^{-1}$  (wavelengths 7.14 – 25  $\mu\text{m}$ ). The major strong absorbance intensity bands corresponding to stretching ( $\nu$ ) and bending ( $\delta$ ) of  $\text{PO}_4$  fundamental vibration are highlighted, with the labels indicating the positions of the band corresponding to vibrational modes (as = antisymmetric, s = symmetric). Molecular models on the top of the spectrum plot show vibrational motions of  $\text{PO}_4$  in monazite.

## 4.2. Feature extraction

The positions (in wavenumber,  $\text{cm}^{-1}$ ) and absorbance intensities (in absorbance unit, a.u.) of the interpolated local minima and maxima features in the spectra were obtained through second-degree polynomial fitting method.

After applying the fitting function to the average spectrum of each sample, interpolated local minima were detected at the troughs, and interpolated local maxima were detected at the peaks of the local features. The results of the feature extraction showed that the function detected a constant number of local minima and maxima features within the region of  $\nu_s$  and  $\delta_{as}$  of phosphate group due to the well-defined shape of these spectral features.

In contrast, varying numbers of local minima and maxima were detected within the  $\nu_{as}$  region, as some local features in this range were weak or absent in some samples. Similarly, the detection function yielded inconsistent results for the single feature in  $\delta_s$  region. This feature was detectable in most samples but appeared as a weak shoulder in the spectra in some samples, such as synthetic monazite-(La) and monazite-(Ce) from Sample Set 1, making it undetectable by the algorithm in these cases.

The extracted features were then categorized into four feature groups, namely A, B, C, and D, in descending order of wavenumber. This grouping corresponds to the spectral range of the  $\text{PO}_4$  vibrational modes present in the monazite spectra ( $\nu_{\text{as}}$ ,  $\nu_{\text{s}}$ ,  $\delta_{\text{as}}$ , and  $\delta_{\text{s}}$  respectively). For broad band like A and C, the features were grouped using the first and last maxima as the indicator, as these maxima features are assumed to directly correspond to the vibrational mode of the phosphate (Clavier et al., 2018; Heuser et al., 2014; Farmer, 1974; Hezel & Ross, 1966). Meanwhile, for single band like B and D, each maximum was grouped with an adjacent minimum from the neighbouring trough. It is important to note that these troughs could represent the transition between different vibrational modes and may not directly reflect a specific vibrational mode.

After grouping, each detected peak was labelled as ‘max’ (for maxima) and each detected trough as ‘min’ (for minima). Both maxima and minima were then sequentially numbered from higher to lower wavenumbers. For feature group A, due to the varying number of detectable features, only the significant features that appeared in every sample were selected for the further analysis. However, it is noted that the spectra of several synthetic monazite samples in this study, including single-REE samples: monazite-(Sm) and double-REE samples: monazite-( $\text{La}_{1-x}\text{Sm}_x$ ) with Sm molar fraction  $\geq 0.50$ , do not display every selected feature in group A since some features are very weak or absent from the spectra. Therefore, these absent features were ignored, and the analysis was continued with the remaining data.

Finally, this selection resulted in a total of 16 features being chosen for further analysis (9 maxima and 7 minima). The summary of the number of the selected features for each group is provided in Table 4.1. The positions of these selected features are shown in the spectra in Figure 4.4.

### 4.3. TIR spectra and feature extraction results of all synthetic monazite samples

The resulting average TIR spectra (from wavenumber  $1400 - 400 \text{ cm}^{-1}$ ) of all monazite samples in this study are presented in Figures 4.5 (single-REE monazite from Sample Set 1), Figure 4.6 ( $\text{La}_{1-x}\text{Nd}_x$  and single-REE: La and Nd monazite from Sample Set 2), and Figure 4.7 ( $\text{La}_{1-x}\text{Sm}_x$  and single-REE: La and Sm monazite from Sample Set 2). Different colours were used to highlight the spectra, indicating the region of the assigned feature group. The selected features for further study were also annotated at the bottommost spectrum for reference. Additionally, small variations in the spectral features, such as shape, intensity, and positional shifts, can be observed across the spectra of each synthetic monazite sample. These variations are further discussed in *Chapter 5.2*. Therefore, to facilitate comparison and improve observation, the spectra are displayed as stacked plots.

The positions and absorbance intensities of the selected features are presented Table 4.2 (single-REE monazite from Sample Set 1 and 2), Table 4.3 ( $\text{La}_{1-x}\text{Nd}_x$  and single-REE: La and Nd monazite from Sample Set 2), and Table 4.4 ( $\text{La}_{1-x}\text{Sm}_x$  and single-REE: La and Sm monazite from Sample Set 2). Moreover, the positions and absorbance intensities of all detectable features in the spectra of all synthetic monazite samples in this study are provided in *Appendix IV*.

Feature group	A (1100 – 980 cm <sup>-1</sup> )	B (970– 950 cm <sup>-1</sup> )	C (650 – 530 cm <sup>-1</sup> )	D (500 – 490 cm <sup>-1</sup> )	Total
Maxima	3	1	4	1	9
Minima	2	1	3	1	7
Total	5	2	7	2	16

Table 4.1 Summary of the number of selected minima and maxima features for each feature group (A, B, C, and D)

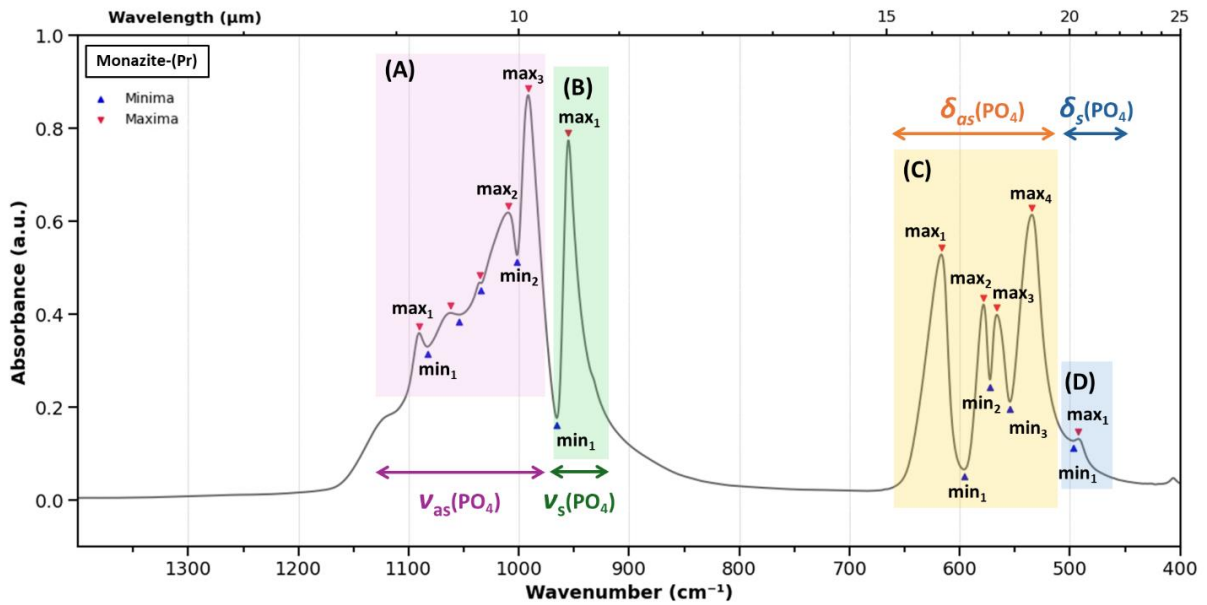
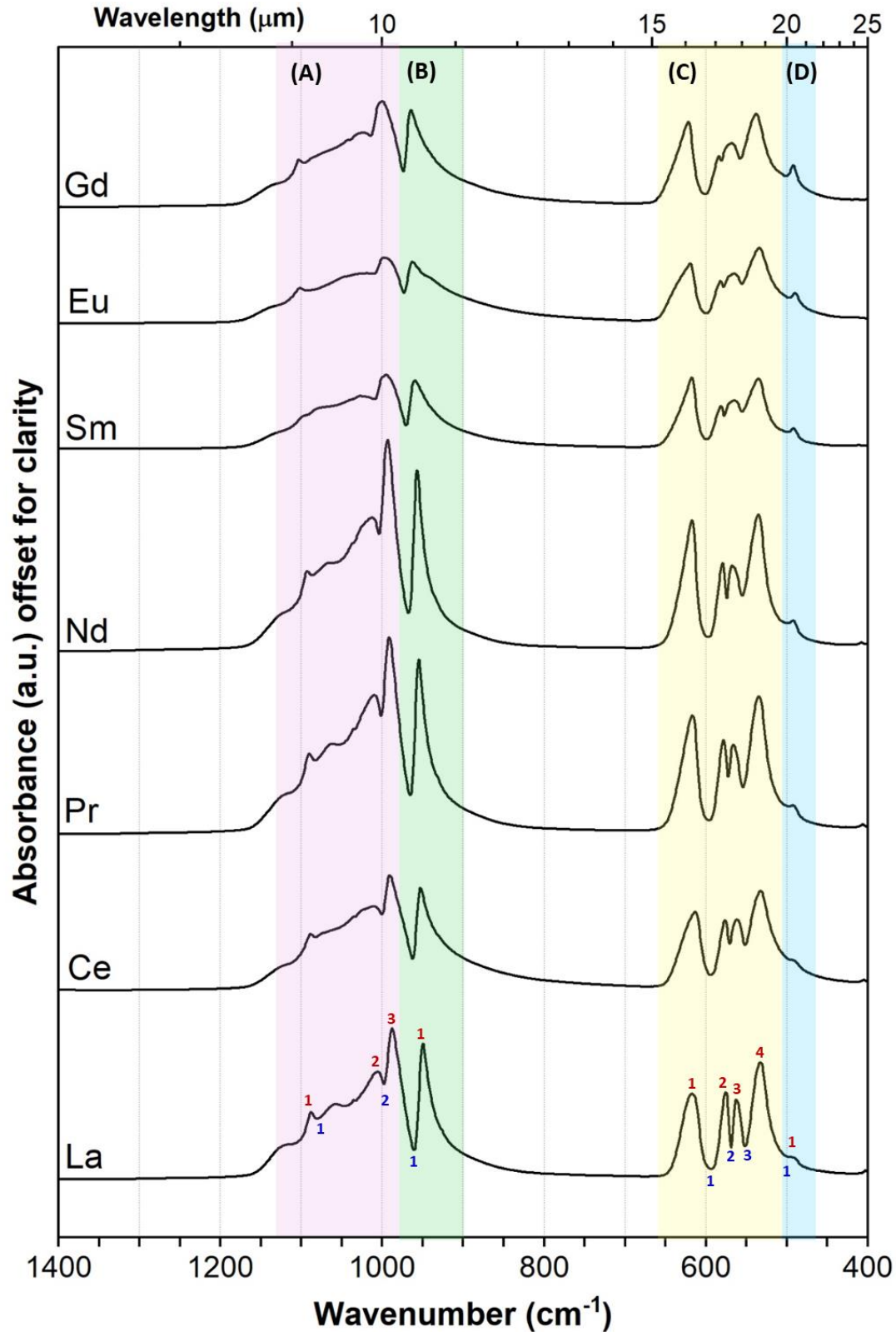


Figure 4.4 Results of the feature extraction method, showing the positions of the detected local features in the TIR absorbance spectra from wavenumbers 1400 – 400 cm<sup>-1</sup> (wavelengths 7.14 – 25 μm) of synthetic monazite-(Pr), marked with triangle symbol (blue for minima, red for maxima). The selected features for the further analysis are annotated with ‘min’ (minima) and ‘max’ (maxima). Local features belonging to each feature group are highlighted: pink - group A, green - group B, yellow - group C, and blue - group D. Arrow labels indicate the region of the bands corresponding to fundamental vibrational modes of phosphate group ( $\nu_{as}$  = antisymmetric stretching,  $\nu_s$  = symmetric stretching,  $\delta_{as}$  = antisymmetric bending,  $\delta_s$  = symmetric bending).



**Figure 4.5** The TIR absorbance spectra from wavenumbers 1400 – 400  $\text{cm}^{-1}$  (wavelengths 7.14 – 25  $\mu\text{m}$ ) of synthetic single-REE monazites (La to Gd) from *Sample Set 1* (synthesized as part of the work of Dijkstra et al., 2024). The spectra are stacked in order of increasing REE atomic number. Local features belonging to each feature group are highlighted: pink - group A, green - group B, yellow - group C, and blue - group D. The selected features for the further analysis are annotated and numbered, with ‘red’ for maxima and ‘blue’ for minima on the spectra of monazite-(La). The spectra are stacked to enable comparison between samples, allowing for better observation of small variations in shape, absorbance intensity and positional shifts of the spectral features.

Single-REE monazites: Spectral features position (cm <sup>-1</sup> )																	
REE	A <sub>max1</sub>	A <sub>min1</sub>	A <sub>max2</sub>	A <sub>min2</sub>	A <sub>max3</sub>	B <sub>min1</sub>	B <sub>max1</sub>	C <sub>max1</sub>	C <sub>min1</sub>	C <sub>max2</sub>	C <sub>min2</sub>	C <sub>max3</sub>	C <sub>min3</sub>	C <sub>max4</sub>	D <sub>min1</sub>	D <sub>max1</sub>	
La	1087.98	1080.30	1005.86	998.10	988.06	960.76	949.94	617.15	593.22	575.51	568.92	562.55	551.66	532.49	ND	ND	
Ce	1088.48	1082.30	1010.88	1000.60	990.88	962.68	952.85	613.02	593.72	576.41	570.72	561.48	551.61	532.23	ND	ND	
Pr	1090.40	1083.02	1009.77	1001.62	991.51	965.56	954.99	616.71	596.14	578.34	572.48	566.26	554.40	534.46	496.99	492.36	
Nd	1092.76	1086.40	1012.52	1004.15	993.47	967.79	957.01	617.24	596.98	579.37	574.36	567.46	555.12	535.09	498.49	492.18	
Sm	ND	ND	1027.38	1009.58	995.00	970.64	959.73	617.52	598.94	581.47	577.31	564.57	555.26	534.89	498.78	491.61	
Eu	1101.52	1092.53	1018.28	1011.42	998.14	973.39	962.85	619.32	599.55	582.01	578.21	564.85	555.52	534.05	497.10	489.83	
Gd	1103.00	1096.52	1023.32	1014.52	999.91	974.22	964.67	621.73	600.89	584.04	581.03	567.63	557.70	537.93	501.21	492.11	
La <sup>[2]</sup>	1085.91	1081.84	1009.26	997.77	987.78	961.90	950.03	611.10	593.57	576.86	569.16	563.33	552.95	534.10	496.76	493.95	
Nd <sup>[2]</sup>	1093.72	1085.95	1015.63	1004.91	995.89	968.22	957.89	618.56	597.61	579.21	574.29	566.76	555.47	537.24	497.88	492.68	
Sm <sup>[2]</sup>	ND	ND	1021.60	1010.49	995.95	970.35	960.01	618.41	599.68	581.57	577.36	565.31	555.79	535.08	498.47	491.47	
Mode	$\nu_{as}$	$\nu_{as}$	$\nu_{as}$	$\nu_{as}$	$\nu_{as}$	$\nu_{as} \rightarrow \nu_s$	$\nu_s$	$\delta_{as}$	$\delta_{as}$	$\delta_{as}$	$\delta_{as}$	$\delta_{as}$	$\delta_{as}$	$\delta_{as}$	$\delta_{as}$	$\delta_{as} \rightarrow \delta_s$	$\delta_s$
Single-REE monazites: Spectral features absorbance intensity (a.u.)																	
REE	A <sub>max1</sub>	A <sub>min1</sub>	A <sub>max2</sub>	A <sub>min2</sub>	A <sub>max3</sub>	B <sub>min1</sub>	B <sub>max1</sub>	C <sub>max1</sub>	C <sub>min1</sub>	C <sub>max2</sub>	C <sub>min2</sub>	C <sub>max3</sub>	C <sub>min3</sub>	C <sub>max4</sub>	D <sub>min1</sub>	D <sub>max1</sub>	
La	0.301	0.273	0.480	0.425	0.673	0.134	0.604	0.383	0.051	0.390	0.146	0.356	0.151	0.521	ND	ND	
Ce	0.252	0.239	0.374	0.340	0.511	0.143	0.456	0.350	0.071	0.312	0.210	0.316	0.205	0.442	ND	ND	
Pr	0.359	0.330	0.619	0.527	0.873	0.176	0.776	0.528	0.065	0.421	0.258	0.398	0.211	0.614	0.127	0.131	
Nd	0.357	0.339	0.594	0.521	0.937	0.172	0.803	0.583	0.067	0.394	0.238	0.382	0.249	0.607	0.128	0.140	
Sm	ND	ND	0.237	0.223	0.330	0.108	0.305	0.321	0.047	0.193	0.151	0.218	0.169	0.315	0.078	0.095	
Eu	0.160	0.149	0.225	0.222	0.294	0.140	0.277	0.268	0.049	0.192	0.164	0.224	0.180	0.338	0.118	0.139	
Gd	0.214	0.201	0.334	0.321	0.473	0.164	0.433	0.383	0.062	0.231	0.211	0.288	0.219	0.417	0.142	0.191	
La <sup>[2]</sup>	0.304	0.300	0.441	0.370	0.738	0.116	0.605	0.527	0.062	0.344	0.139	0.294	0.149	0.454	0.071	0.071	
Nd <sup>[2]</sup>	0.257	0.243	0.421	0.369	0.553	0.135	0.467	0.353	0.057	0.281	0.186	0.289	0.207	0.407	0.100	0.104	
Sm <sup>[2]</sup>	ND	ND	0.215	0.211	0.295	0.117	0.268	0.258	0.049	0.180	0.147	0.203	0.172	0.298	0.100	0.113	
Mode	$\nu_{as}$	$\nu_{as}$	$\nu_{as}$	$\nu_{as}$	$\nu_{as}$	$\nu_{as} \rightarrow \nu_s$	$\nu_s$	$\delta_{as}$	$\delta_{as}$	$\delta_{as}$	$\delta_{as}$	$\delta_{as}$	$\delta_{as}$	$\delta_{as}$	$\delta_{as}$	$\delta_{as} \rightarrow \delta_s$	$\delta_s$

**Table 4.2 (Top)** Positions and **(Bottom)** absorbance intensities of the selected minima (min) and maxima (max) features within TIR absorbance spectra from wavenumbers 1400 – 400 cm<sup>-1</sup> of synthetic **single-REE monazites** from *Sample Set 1 (La to Gd)* and *Sample Set 2 (La, Nd, and Sm; labeled with [2])*. ‘ND’ refers to not detectable. The corresponding fundamental vibrational modes of phosphate group for each feature are provided.

Note:  $\nu_{as}$  = antisymmetric stretching,  $\nu_s$  = symmetric stretching,  $\delta_{as}$  = antisymmetric bending,  $\delta_s$  = symmetric bending; ‘→’ indicates the transition between the modes

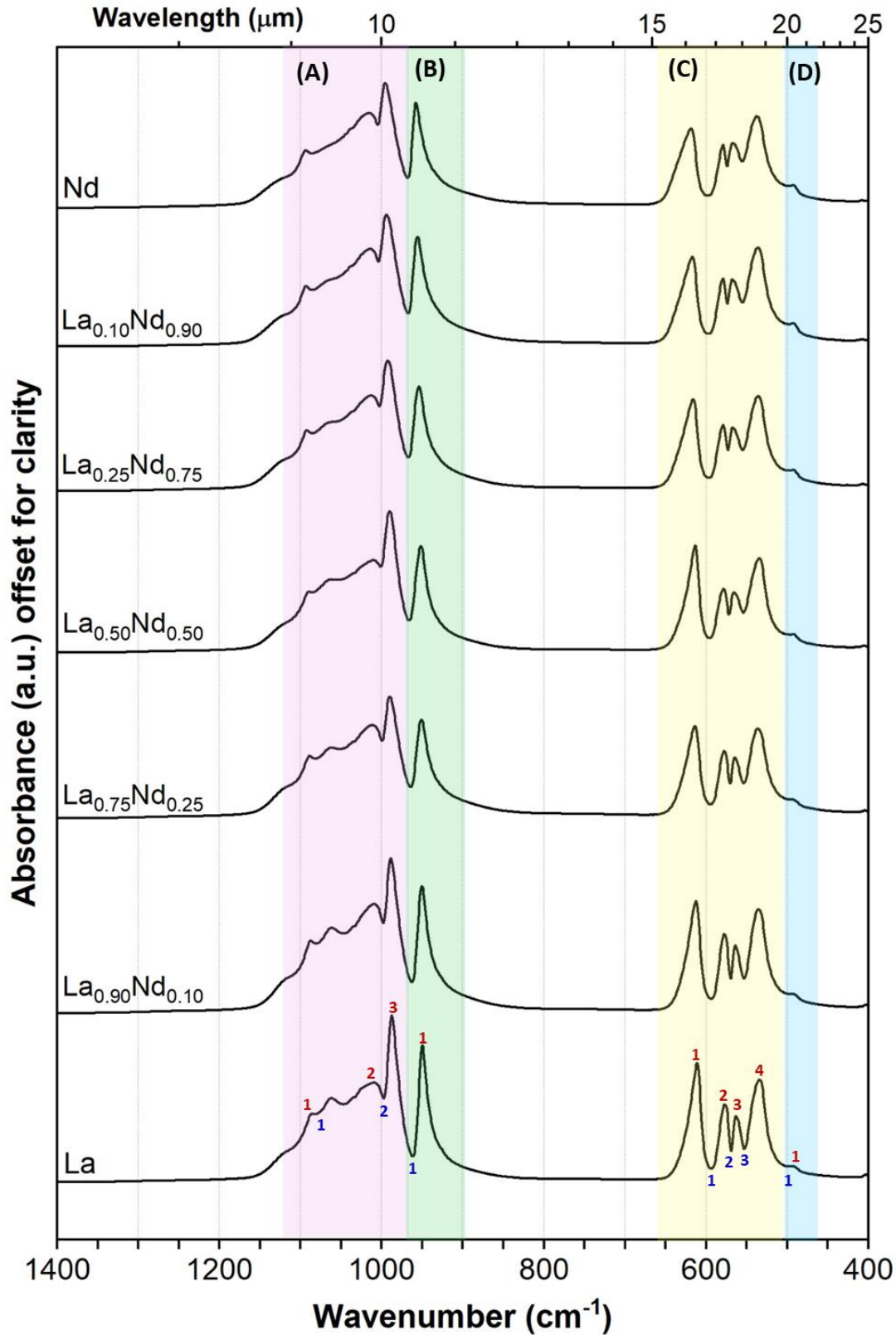


**Figure 4.6** The TIR absorbance spectra from wavenumbers 1400 – 400  $\text{cm}^{-1}$  (wavelengths 7.14 – 25  $\mu\text{m}$ ) of synthetic  $\text{La}_{1-x}\text{Nd}_x$  and single-REE: La and Nd monazites from *Sample Set 2 (synthesized in this study)*. The spectra are stacked in order of increasing Nd molar fraction ( $x$ ). Local features belonging to each feature group are highlighted: pink - group A, green - group B, yellow - group C, and blue - group D. The selected features for the further analysis are annotated and numbered, with 'red' for maxima and 'blue' for minima on the spectra of monazite-(La). The spectra are stacked to enable comparison between samples, allowing for better observation of small variations in shape, absorbance intensity and positional shifts of the spectral features.

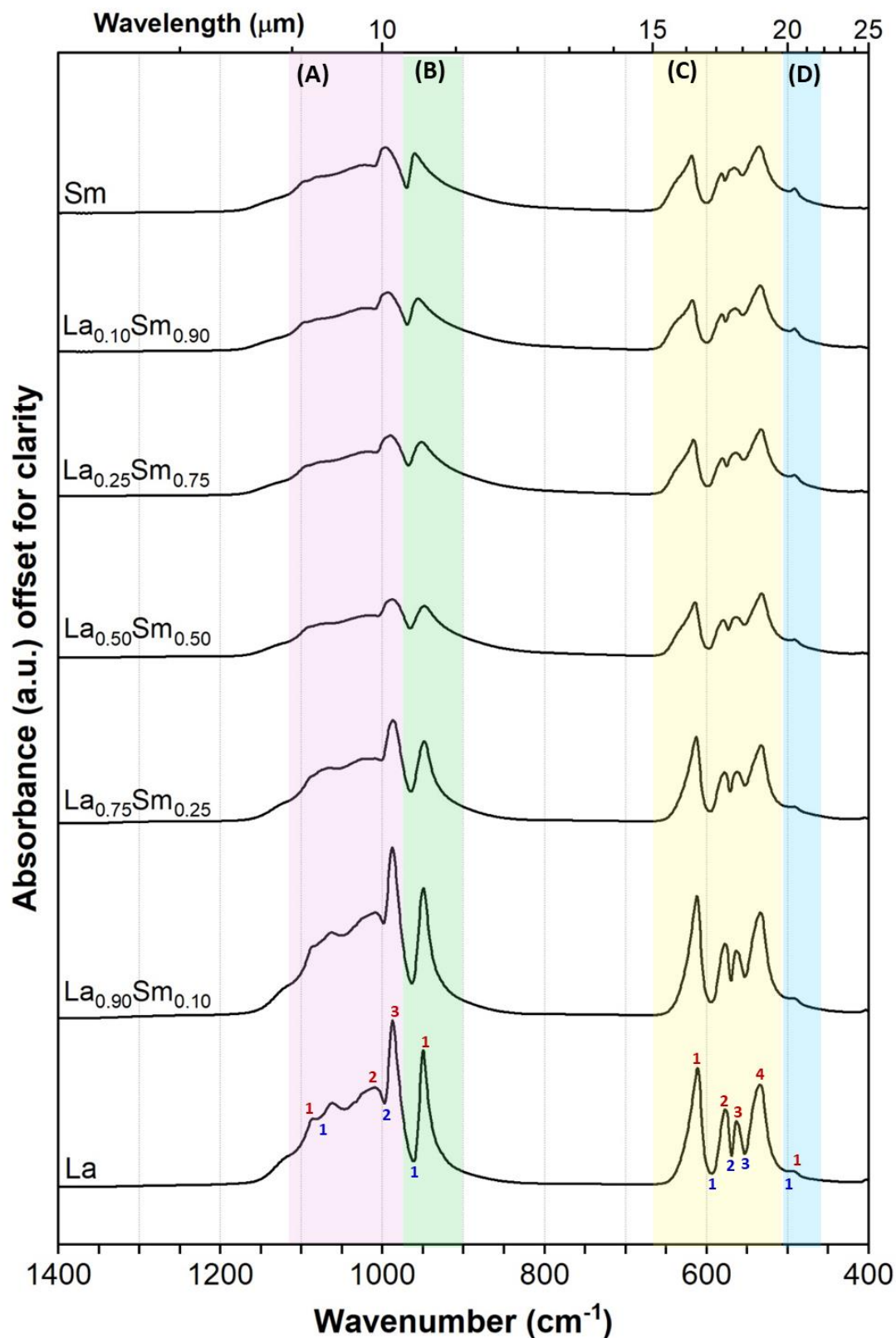
Monazites - (La <sub>1-x</sub> Nd <sub>x</sub> ) : Spectral features position (cm <sup>-1</sup> )																	
<i>Nd<sub>x</sub></i>	<i>A</i> <sub>max1</sub>	<i>A</i> <sub>min1</sub>	<i>A</i> <sub>max2</sub>	<i>A</i> <sub>min2</sub>	<i>A</i> <sub>max3</sub>	<i>B</i> <sub>min1</sub>	<i>B</i> <sub>max1</sub>	<i>C</i> <sub>max1</sub>	<i>C</i> <sub>min1</sub>	<i>C</i> <sub>max2</sub>	<i>C</i> <sub>min2</sub>	<i>C</i> <sub>max3</sub>	<i>C</i> <sub>min3</sub>	<i>C</i> <sub>max4</sub>	<i>D</i> <sub>min1</sub>	<i>D</i> <sub>max1</sub>	
<b>0.00*</b>	1085.91	1081.84	1009.26	997.77	987.78	961.90	950.03	611.10	593.57	576.86	569.16	563.33	552.95	534.10	496.76	493.95	
<b>0.10</b>	1087.50	1080.79	1009.29	998.28	988.93	963.05	950.53	612.64	593.76	577.49	569.71	564.16	553.31	535.19	495.40	493.67	
<b>0.25</b>	1088.89	1081.57	1011.46	999.52	990.17	964.35	951.09	613.80	594.37	577.72	570.45	564.66	553.68	535.96	ND	ND	
<b>0.50</b>	1089.50	1085.39	1009.95	1001.38	990.10	966.25	951.77	613.48	595.65	578.46	571.85	565.45	554.15	534.28	496.44	492.27	
<b>0.75</b>	1092.08	1085.16	1012.78	1002.92	992.59	967.28	954.10	616.05	596.60	579.08	573.20	567.05	554.93	535.54	497.49	492.20	
<b>0.90</b>	1093.25	1085.45	1014.13	1004.02	993.95	967.62	955.90	617.06	597.02	579.28	573.93	567.56	555.25	535.93	497.61	492.49	
<b>1.00*</b>	1093.72	1085.95	1015.63	1004.91	995.89	968.22	957.89	618.56	597.61	579.21	574.29	566.76	555.47	537.24	497.88	492.68	
<i>Mode</i>	<i>ν</i> <sub>as</sub>	<i>ν</i> <sub>as</sub>	<i>ν</i> <sub>as</sub>	<i>ν</i> <sub>as</sub>	<i>ν</i> <sub>as</sub>	<i>ν</i> <sub>as</sub> → <i>ν</i> <sub>s</sub>	<i>ν</i> <sub>s</sub>	<i>δ</i> <sub>as</sub>	<i>δ</i> <sub>as</sub>	<i>δ</i> <sub>as</sub>	<i>δ</i> <sub>as</sub>	<i>δ</i> <sub>as</sub>	<i>δ</i> <sub>as</sub>	<i>δ</i> <sub>as</sub>	<i>δ</i> <sub>as</sub>	<i>δ</i> <sub>as</sub> → <i>δ</i> <sub>s</sub>	<i>δ</i> <sub>s</sub>

Monazites - (La <sub>1-x</sub> Nd <sub>x</sub> ) : Spectral features absorbance intensity (a.u.)																	
<i>Nd<sub>x</sub></i>	<i>A</i> <sub>max1</sub>	<i>A</i> <sub>min1</sub>	<i>A</i> <sub>max2</sub>	<i>A</i> <sub>min2</sub>	<i>A</i> <sub>max3</sub>	<i>B</i> <sub>min1</sub>	<i>B</i> <sub>max1</sub>	<i>C</i> <sub>max1</sub>	<i>C</i> <sub>min1</sub>	<i>C</i> <sub>max2</sub>	<i>C</i> <sub>min2</sub>	<i>C</i> <sub>max3</sub>	<i>C</i> <sub>min3</sub>	<i>C</i> <sub>max4</sub>	<i>D</i> <sub>min1</sub>	<i>D</i> <sub>max1</sub>	
<b>0.00*</b>	0.304	0.300	0.441	0.370	0.738	0.116	0.605	0.527	0.062	0.344	0.139	0.294	0.149	0.454	0.071	0.071	
<b>0.10</b>	0.322	0.311	0.484	0.401	0.686	0.140	0.563	0.497	0.068	0.352	0.156	0.303	0.156	0.462	0.088	0.088	
<b>0.25</b>	0.278	0.266	0.413	0.346	0.540	0.141	0.437	0.409	0.064	0.300	0.156	0.272	0.156	0.397	ND	ND	
<b>0.50</b>	0.272	0.269	0.410	0.382	0.625	0.147	0.472	0.476	0.068	0.285	0.171	0.269	0.179	0.420	0.082	0.084	
<b>0.75</b>	0.271	0.259	0.425	0.378	0.579	0.152	0.466	0.408	0.062	0.294	0.184	0.284	0.185	0.423	0.094	0.097	
<b>0.90</b>	0.270	0.252	0.433	0.379	0.583	0.150	0.487	0.399	0.060	0.304	0.192	0.298	0.197	0.440	0.102	0.107	
<b>1.00*</b>	0.257	0.243	0.421	0.369	0.553	0.135	0.467	0.353	0.057	0.281	0.186	0.289	0.207	0.407	0.100	0.104	
<i>Mode</i>	<i>ν</i> <sub>as</sub>	<i>ν</i> <sub>as</sub>	<i>ν</i> <sub>as</sub>	<i>ν</i> <sub>as</sub>	<i>ν</i> <sub>as</sub>	<i>ν</i> <sub>as</sub> → <i>ν</i> <sub>s</sub>	<i>ν</i> <sub>s</sub>	<i>δ</i> <sub>as</sub>	<i>δ</i> <sub>as</sub>	<i>δ</i> <sub>as</sub>	<i>δ</i> <sub>as</sub>	<i>δ</i> <sub>as</sub>	<i>δ</i> <sub>as</sub>	<i>δ</i> <sub>as</sub>	<i>δ</i> <sub>as</sub>	<i>δ</i> <sub>as</sub> → <i>δ</i> <sub>s</sub>	<i>δ</i> <sub>s</sub>

**Table 4.3 (Top)** Positions and **(Bottom)** absorbance intensities of the selected minima (min) and maxima (max) features within TIR absorbance spectra from wavenumbers 1400 – 400 cm<sup>-1</sup> of synthetic La<sub>1-x</sub>Nd<sub>x</sub> (*X* as the Molar fraction of Nd) and single-REE: La (shown as 0.00\*) and Nd (shown as 1.00\*) monazites from *Sample Set 2*. 'ND' refers to not detectable. The corresponding fundamental vibrational modes of phosphate group for each feature are provided.

Note: *ν*<sub>as</sub> = antisymmetric stretching, *ν*<sub>s</sub> = symmetric stretching, *δ*<sub>as</sub> = antisymmetric bending, *δ*<sub>s</sub> = symmetric bending; '→' indicates the transition between the modes



**Figure 4.7** The TIR absorbance spectra from wavenumbers 1400 – 400 cm<sup>-1</sup> (wavelengths 7.14 – 25 μm) of synthetic  $\text{La}_{1-x}\text{Sm}_x$  and single-REE: La and Sm monazites from *Sample Set 2 (synthesized in this study)*. The spectra are stacked in order of increasing Sm molar fraction (x). Local features belonging to each feature group are highlighted: pink - group A, green - group B, yellow - group C, and blue - group D. The selected features for the further analysis are annotated and numbered, with 'red' for maxima and 'blue' for minima on the spectra of monazite-(La). The spectra are stacked to enable comparison between samples, allowing for better observation of small variations in shape, absorbance intensity and positional shifts of the spectral features.



Monazites - (La <sub>1-x</sub> Sm <sub>x</sub> ) : Spectral features position (cm <sup>-1</sup> )																
<i>Sm<sub>x</sub></i>	A <sub>max1</sub>	A <sub>min1</sub>	A <sub>max2</sub>	A <sub>min2</sub>	A <sub>max3</sub>	B <sub>min1</sub>	B <sub>max1</sub>	C <sub>max1</sub>	C <sub>min1</sub>	C <sub>max2</sub>	C <sub>min2</sub>	C <sub>max3</sub>	C <sub>min3</sub>	C <sub>max4</sub>	D <sub>min1</sub>	D <sub>max1</sub>
<b>0.00*</b>	1085.91	1081.84	1009.26	997.77	987.78	961.90	950.03	611.10	593.57	576.86	569.16	563.33	552.95	534.10	496.76	493.95
<b>0.10</b>	ND	ND	1008.85	998.89	988.08	963.85	949.68	611.96	594.15	577.22	569.88	563.43	552.85	533.51	494.98	491.93
<b>0.25</b>	ND	ND	1008.98	1001.75	987.03	965.08	948.63	612.86	595.58	577.62	571.07	562.32	552.81	532.50	495.91	491.29
<b>0.50</b>	ND	ND	1012.59	1005.92	987.30	965.90	948.29	614.34	597.31	579.09	573.28	563.10	553.45	531.91	496.68	491.34
<b>0.75</b>	ND	ND	1017.34	1008.42	989.93	968.10	951.87	616.03	598.45	580.33	575.40	563.49	554.18	532.89	497.65	491.20
<b>0.90</b>	ND	ND	1020.76	1010.21	992.93	969.49	955.96	617.61	599.40	581.13	576.64	564.46	555.15	533.80	498.01	491.36
<b>1.00*</b>	ND	ND	1021.60	1010.49	995.95	970.35	960.01	618.41	599.68	581.57	577.36	565.31	555.79	535.08	498.47	491.47
<i>Mode</i>	$\nu_{as}$	$\nu_{as}$	$\nu_{as}$	$\nu_{as}$	$\nu_{as}$	$\nu_{as} \rightarrow \nu_s$	$\nu_s$	$\delta_{as}$	$\delta_{as}$	$\delta_{as}$	$\delta_{as}$	$\delta_{as}$	$\delta_{as}$	$\delta_{as}$	$\delta_{as} \rightarrow \delta_s$	$\delta_s$

Monazites - (La <sub>1-x</sub> Sm <sub>x</sub> ) : Spectral features absorbance intensity (a.u.)																
<i>Sm<sub>x</sub></i>	A <sub>max1</sub>	A <sub>min1</sub>	A <sub>max2</sub>	A <sub>min2</sub>	A <sub>max3</sub>	B <sub>min1</sub>	B <sub>max1</sub>	C <sub>max1</sub>	C <sub>min1</sub>	C <sub>max2</sub>	C <sub>min2</sub>	C <sub>max3</sub>	C <sub>min3</sub>	C <sub>max4</sub>	D <sub>min1</sub>	D <sub>max1</sub>
<b>0.00*</b>	0.304	0.300	0.441	0.370	0.738	0.116	0.605	0.527	0.062	0.344	0.139	0.294	0.149	0.454	0.071	0.071
<b>0.10</b>	ND	ND	0.468	0.422	0.757	0.157	0.576	0.543	0.074	0.332	0.168	0.302	0.186	0.469	0.091	0.091
<b>0.25</b>	ND	ND	0.288	0.280	0.458	0.144	0.365	0.384	0.056	0.229	0.143	0.230	0.169	0.348	0.075	0.076
<b>0.50</b>	ND	ND	0.189	0.187	0.261	0.134	0.231	0.248	0.045	0.169	0.127	0.183	0.149	0.287	0.080	0.083
<b>0.75</b>	ND	ND	0.200	0.197	0.271	0.140	0.243	0.254	0.048	0.172	0.138	0.195	0.165	0.300	0.092	0.098
<b>0.90</b>	ND	ND	0.196	0.193	0.266	0.124	0.238	0.232	0.046	0.169	0.138	0.194	0.165	0.297	0.095	0.106
<b>1.00*</b>	ND	ND	0.215	0.211	0.295	0.117	0.268	0.258	0.049	0.180	0.147	0.203	0.172	0.298	0.100	0.113
<i>Mode</i>	$\nu_{as}$	$\nu_{as}$	$\nu_{as}$	$\nu_{as}$	$\nu_{as}$	$\nu_{as} \rightarrow \nu_s$	$\nu_s$	$\delta_{as}$	$\delta_{as}$	$\delta_{as}$	$\delta_{as}$	$\delta_{as}$	$\delta_{as}$	$\delta_{as}$	$\delta_{as} \rightarrow \delta_s$	$\delta_s$

**Table 4.4 (Top)** Positions and **(Bottom)** absorbance intensities of the selected minima (min) and maxima (max) features within TIR absorbance spectra from wavenumbers 1400 – 400 cm<sup>-1</sup> of synthetic La<sub>1-x</sub>Sm<sub>x</sub> (*X* as the Molar fraction of Nd) and single-REE: La (shown as 0.00\*) and Sm (shown as 1.00\*) monazites from *Sample Set 2*. 'ND' refers to not detectable. The corresponding fundamental vibrational modes of phosphate group for each feature are provided.

Note:  $\nu_{as}$  = antisymmetric stretching,  $\nu_s$  = symmetric stretching,  $\delta_{as}$  = antisymmetric bending,  $\delta_s$  = symmetric bending; '→' indicates the transition between the modes

## 5. DISCUSSION

This chapter covers the discussions on methodology and results of this study. The methodology section reviews the use of ATR-FTIR spectroscopy for TIR data collection and discusses the advantages and limitations of using second-degree polynomial fitting algorithms for feature extraction. The results section provides a detailed analysis of how the TIR spectra of monazite change with different REE contents, suggesting possible reasons for these changes. Finally, the chapter provide the comparison between the TIR spectra of synthetic monazites in this study and the natural monazite samples and explore the potential applications of the findings.

### 5.1. Discussion on methodology

#### 5.1.1. TIR spectra acquisition using the ATR-FTIR spectroscopy technique

There are several sampling techniques for TIR spectra acquisition. One of the most popular techniques is transmission FTIR, which is considered as a traditional method for measuring the infrared spectra in TIR range. This technique has been widely used for studying the TIR spectra of earth materials samples in spectral geology (Salisbury et al., 1987; Chukanov, 2014). In transmission FTIR, the infrared beam passes directly through the sample. This ensures that the resulting spectra capture the spectral features of the bulk property within the sample. This method also produces high-quality spectra with a very high signal-to-noise ratio with well-defined and distinguishable spectral features, making the spectral interpretation becomes easier (Smith, 2011). However, preparing KBr pellets is necessary to obtain the spectra, which can be time-consuming. Additionally, the preparation of KBr pellets requires a lot of experience. Consequently, the manual preparation can impact the quality of the spectra, making this method less suitable for inexperienced users (Smith, 2011).

The TIR spectra in this study were acquired using ATR-FTIR sampling technique. The theory behind this technique is different from that of the transmission technique, as explained in *Chapter 2.4*. ATR-FTIR is a surface technique that captures the spectra of the material within direct contact with the ATR crystal. However, our results demonstrate that ATR is an excellent alternative for the studying the TIR spectra of minerals with slight differences in chemical composition, particularly regarding REE incorporation within the samples. This technique shows that it consistently produces the spectra with consistent shape and position across repeated measurements of the same sample, emphasizing the method's reproducibility, and it also provides the high-quality spectra with minimal noise interference. Moreover, Farmer (1974) points out that spectra from ATR-FTIR closely resemble to those obtained using the traditional transmission technique comparing to other FTIR sampling techniques. This finding was further confirmed by Beasley et al. (2014).

It is important to note that TIR spectra from ATR and transmission techniques are not identical. For transmission FTIR spectra, the relative intensity of spectral features remains relatively constant across the entire spectrum. In contrast, for ATR-FTIR spectra, the relative intensity of spectral features changes with wavenumber. This variation occurs because the penetration depth in ATR spectroscopy depends on the wavelength and is inversely proportional to the wavenumber (Stuart, 2004; Smith, 2011). As a result, ATR spectra significantly show weaker intensities at higher wavenumbers (i.e., lower wavelengths) and stronger intensities at lower wavenumbers (i.e., higher wavelengths). However, this should not be an issue

in this study since the fundamental vibrations of the phosphate group within monazite occur only in the lower wavenumber region (at wavenumber below  $1200\text{ cm}^{-1}$ ).

Another difference is that, when comparing the spectra between ATR-FTIR and transmission FTIR, the ATR spectra show lower intensity of background carbon dioxide (around  $2350\text{ cm}^{-1}$  and  $667\text{ cm}^{-1}$ ) and water vapours absorption features (from  $2000 - 1300\text{ cm}^{-1}$ ). As shown in Figure 5.1, these features are very prominent in transmission spectra because carbon dioxide and water vapor are unavoidably introduced to the sample during the preparation of KBr pellets (Smith, 2011).

For these reasons, a direct comparison between TIR spectra obtained from ATR-FTIR and transmission FTIR techniques is not effective, as the spectra from these two methods differ in both intensity and shape. Therefore, for detailed analysis, particularly when interest in the shape and spectral intensity of features, ATR-FTIR spectra should be compared exclusively with other ATR-FTIR spectra.

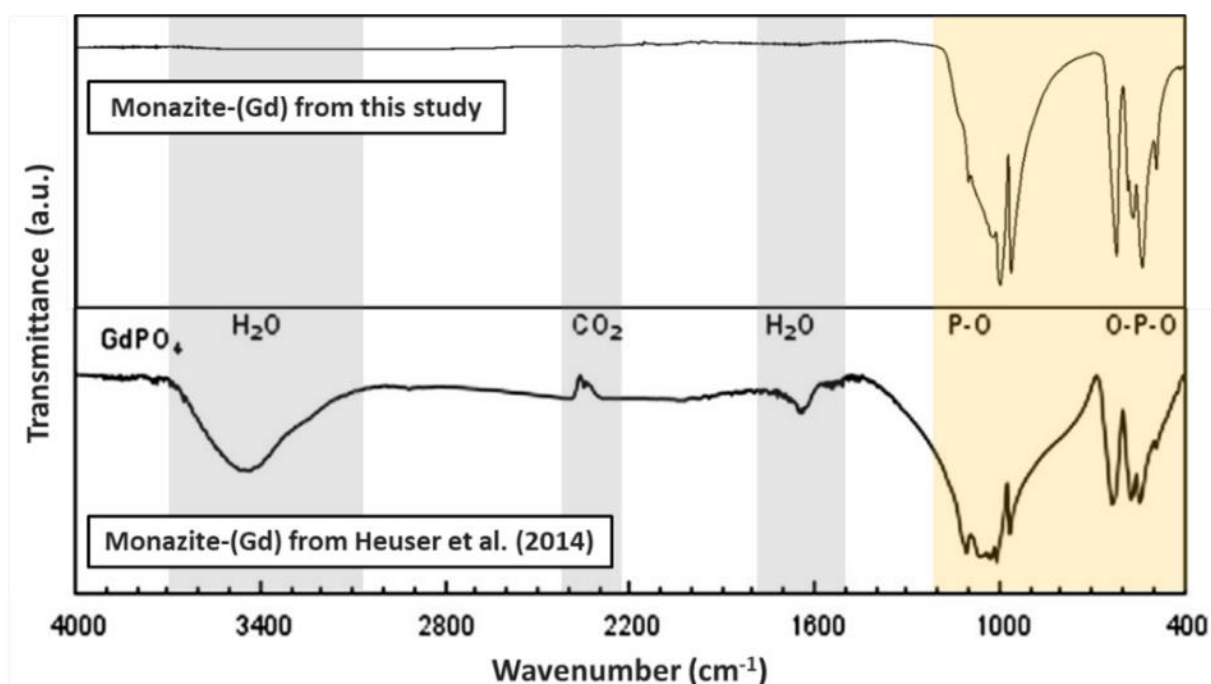


**Figure 5.1** TIR spectra from wavenumbers  $4000 - 400\text{ cm}^{-1}$  of monazite-(Gd) (**Top**) from this study, recorded with ATR-FTIR (**Bottom**) modify from Heuser et al. (2014), recorded with transmission FTIR. The spectra are stacked and displayed in transmittance mode for comparison. Yellow highlight indicates the region of fundamental vibration of  $\text{PO}_4$  within the monazite. Gray highlight indicates the region where the features of water vapours and carbon dioxide display in transmission FTIR spectra.

### 5.1.2. Feature extraction using second-degree polynomial fitting method

In this study, a second-degree polynomial fitting method was used to determine wavenumber positions and absorbance intensities of the maxima (peaks) and minima (troughs) features within the TIR spectra. This approach calculated the interpolated vertices of each extrema features, yielding more precise positions compared to the values observed directly in the spectra (Figure 5.2). This is because the observed positions of the maxima and minima in the spectra corresponding to the spectral band positions of the spectroscopy instrument, which might not accurately represent the true locations of these features.

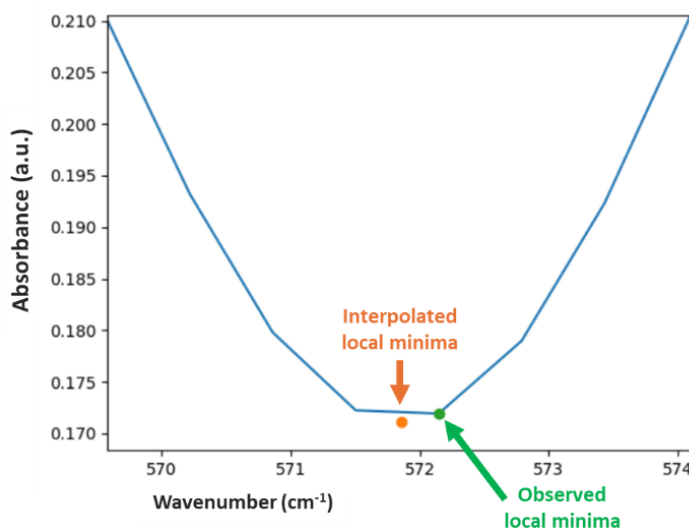


**Figure 5.2** Example of interpolated local minimum obtained after applying the second-degree polynomial fitting function to Feature  $C_{\min 2}$  from the spectrum of monazite-( $La_{50}Nd_{50}$ ). Interpolated local minimum provides more accurate minimum position compared to the observed local minima, which is the lowest points in the spectrum

For TIR spectra analysis, peak positions (i.e., absorbance maxima or transmittance minima) are a primary focus in most of the infrared spectra studies, as they indicate the positions of the specific vibrational modes which are diagnostic in each particular molecule. Therefore, various peak search algorithms are employed to locate the position of peaks. Many spectra processing methods, such as spectra deconvolution or curve decomposition, using Gaussian or Lorentzian models, are widely used to extract features from the spectra. However, obtaining accurate results that closely resemble the true values in the spectra often requires background knowledge to adjust parameters effectively.

In contrast, the feature extraction method used in our study is more straightforward. It can be performed without any prior knowledge of signal processing and has been proven to be reproducible, yielding accurate results without the need to adjust complex mathematical parameters. Our study demonstrates that this feature extraction method can also detect minimal shifts, up to  $0.22\text{ cm}^{-1}$ , in feature  $C_{\min 3}$  of the  $La_{1-x}Nd_x$  monazites series. This highlights the robustness and precision of our method in capturing subtle variations in the spectra.

However, a limitation of the second-degree polynomial fitting method is its inability to detect weak shoulder features within the spectra (e.g., features A and features D). To identify these features, more advanced signal processing and spectral manipulation algorithms, such as spectral deconvolution, are required.

## 5.2. Changes in TIR spectra of monazite with different REE contents

After performing a detailed comparison of all obtained monazite spectra and analysing the positions and absorbance intensities of the selected features of every samples, we found that all synthetic monazite, both single-REE and double-REE, show slight variations within the spectra in both overall and local features, as the relative abundance and the species of REE incorporated within the mineral change.

Based on the observations, monazite spectra do not exhibit any diagnostic features specifically related to the REE contents within the mineral like in VNIR-SWIR range. Instead, the changes are observed as ‘trends’ and can only be seen when making a comparison between the spectra. The trends can be categorized into five types: (1) changes in absorbance intensity of the overall PO<sub>4</sub> features, (2) changes in absorbance intensity of an individual feature, (3) relative changes in intensities between two local features, (4) changes in the number of detectable features, and (5) shifts in spectral feature wavenumber positions.

While visual comparison between each spectra can provide an overview of these ‘trends of changes’, more concrete evidence can be obtained by plotting the absorbance intensities or wavenumber positions of specific features against the quantitative properties of REEs incorporated within each monazite sample. For single-REE monazites, the features (from Table 4.2) are plotted against the cationic radii of the REEs (CN = 9, Shannon, 1976), while for double-REE monazites, the features (from Table 4.3 and 4.4) are plotted against the molar fractions (x) of Nd and Sm. Another notable observation is that the trend of changes within the spectra of monazites in single-REE series behave in a similar manner with the monazites in double-REE series, as the spectra show the changes toward different in REE proportions within the mineral (see the comparison between Figure 4.5, 4.6, and 4.7 in *Chapter 4.3*).

Moreover, when comparing the spectra of the same single-REE monazite but from two different sample sets (REE = La, Nd, and Sm from Sample Set 1 and Sample Set 2), it was found that the two spectra are not exactly identical. To be more specific, the differences within the spectral features in term of shape, intensity, and feature positions can be observed between the two spectra. These observation are discussed further in *Chapter 5.3*.

### 5.2.1. Changes in absorbance intensity of the overall PO<sub>4</sub> features

The absorbance intensities of the spectral features due to the fundamental vibrations of PO<sub>4</sub> in monazite vary with changes in REE contents in the minerals. For single-REE monazites, it is observed that the overall intensities of the PO<sub>4</sub> features are stronger for REEs with lower atomic numbers (La to Nd), whereas REEs with higher atomic numbers (Sm to Gd) exhibit lower intensities (see Figure 4.5). This observation is supported by directly comparing the absorbance intensity of feature A<sub>max3</sub> in the spectra of the synthetic monazites (see a peak at ~990 cm<sup>-1</sup> in Figure 4.5, 4.6, and 4.7). This specific feature was selected because it consistently shows the highest absorbance intensity in most of the monazite spectra in this study.

The results show that for single-REE monazites, there is no clear linear trend in the overall intensity changes. However, the plot in Figure 5.3 (left) shows that monazite-(Sm), (Eu), and (Gd) exhibit weaker intensities of feature A<sub>max3</sub> (less than 0.5 a.u.). Additionally, a comparison between monazite-(La), (Nd), and (Sm) from Sample Sets 1 and 2 reveals a significant difference between the Nd samples, indicating that the intensity of monazite-(Nd) from Sample Set 2 is almost half as strong as Sample Set 1 (see Figure 4.6 and 4.7).

In contrast to single-REE monazites, the spectra of double-REE monazites, both  $\text{La}_{1-x}\text{Nd}_x$  and  $\text{La}_{1-x}\text{Sm}_x$  series, show more pronounced linear correlations in the decrease of feature  $A_{\text{max}3}$  intensity as Nd and Sm content in the mineral increases. This is indicated by correlation coefficient ( $R^2$ ) exceeding 0.50 for both series (Figure 5.3, Middle and Right). Moreover, the plot reveals that the rate of change in  $A_{\text{max}3}$  intensity is higher in  $\text{La}_{1-x}\text{Sm}_x$  series when compared to  $\text{La}_{1-x}\text{Nd}_x$  series, indicating a gradual weakening in the overall intensity of the  $\text{PO}_4$  features in the monazite spectra.

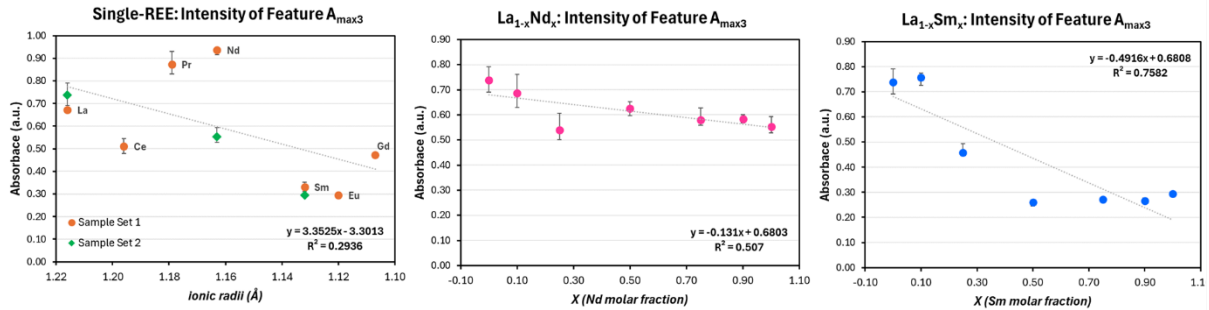


**Figure 5.3** Scatter plots showing how absorbance intensity of feature  $A_{\text{max}3}$  changes with different REE contents in synthetic monazites. **(Left)** Single-REE monazites (from Sample Set 1 and 2), **(Middle)**  $\text{La}_{1-x}\text{Nd}_x$  monazites, and **(Right)**  $\text{La}_{1-x}\text{Sm}_x$  monazites. The single-REE data is plotted against ionic radii of  $\text{REE}^{3+}$  (CN = 9; Shannon, 1976), while double-REE data are plotted against molar fraction of Nd and Sm respectively. The trendline and correlation coefficient in single-REE plot correspond to Sample Set 1. Error bars indicate the minimum and maximum values obtained from the repeated measurement spectra of each sample.

### 5.2.2. Changes in absorbance intensity of the individual features

Despite the overall weakening in absorbance intensities of the  $\text{PO}_4$  features as atomic number of REEs in single-REE monazites increases and content of Nd and Sm in double-REE monazites increases, feature  $D_{\text{max}1}$  shows an opposite trend (see a peak at  $\sim 490 \text{ cm}^{-1}$  in Figure 4.5, 4.6, and 4.7). This particular feature corresponds to symmetric bending vibration ( $\delta_s$ ) of  $\text{PO}_4$  within the monazite. Based on the observation, the absorbance intensity of this feature consistently shows a systematic increasing trend as the REE contents within both single-REE and double-REE monazite series change. Additionally, this trend was also observed in previous studies of single-REE monazite spectra, as reported in Kijkowska et al. (2003) and Heuser et al. (2014).

This trend can be confirmed by comparing the ratio between the absorbance intensities of feature  $D_{\text{max}1}$  and  $D_{\text{min}1}$ . A ratio close to 1.0 indicates a minimal change in the intensities between these two features, while higher values suggest a greater rate of change.

In single-REE monazites, feature  $D_{\text{max}1}$  is absent in the monazite-(La) and (Ce) spectra from Sample Set 1. Despite this, the linear increasing trend can be observed as the atomic number of REE increases (Figure 5.4, Left). As shown in the spectra, the feature becomes progressively more distinct, becoming clearly visible in monazite-(Gd) spectrum. Although the ratio results for monazite-(La), (Nd), and (Sm) in Sample Set 2 are different from those in Sample Set 1, a similar linear increasing trend is also observed.

In double-REE monazites, the intensity of features  $D_{\text{max}1}$  appears to be weaker when La content within the mineral is high, then the feature develops a stronger absorbance intensity and becomes more distinct as the content of Nd and Sm within the mineral increases (Figure 5.4, Middle and Right).

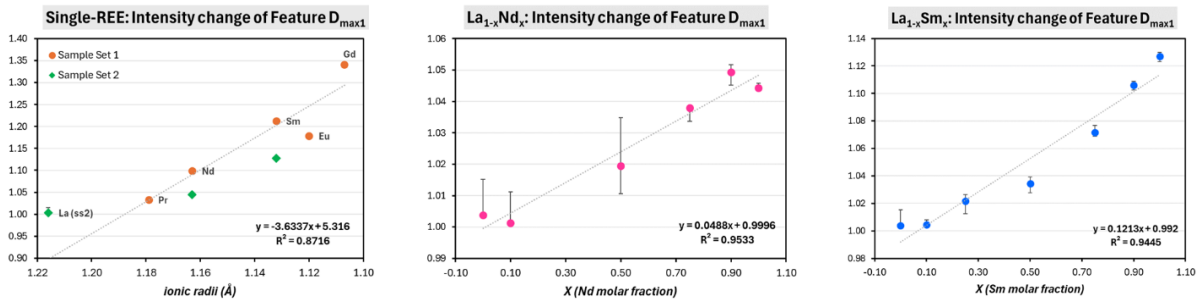


**Figure 5.4** Scatter plots showing how **absorbance intensity of feature D<sub>max1</sub>** changes with different REE contents in synthetic monazites. **(Left)** Single-REE monazites (from Sample Set 1 and 2), **(Middle)** La<sub>1-x</sub>Nd<sub>x</sub> monazites, and **(Right)** La<sub>1-x</sub>Sm<sub>x</sub> monazites. The single-REE data is plotted against ionic radii of REE<sup>3+</sup> (CN = 9; Shannon, 1976), while double-REE data are plotted against molar fraction of Nd and Sm respectively. The trendline and correlation coefficient in single-REE plot correspond to Sample Set 1. Error bars indicates the minimum and maximum values obtained from the repeated measurement spectra of each sample. Noted that D<sub>max1</sub> feature is undetectable in the spectra of monazite-(La) and (Ce) from Sample Set 1 and monazite-(La<sub>0.75</sub>Nd<sub>0.25</sub>)

### 5.2.3. Relative changes in intensity between two local features

Systematic changes in the intensities between two local maxima features: C<sub>max2</sub> and C<sub>max3</sub> are found with varying REE contents within the minerals. This trend can be observed in both single-REE and double-REE monazite series. To be more specific, feature C<sub>max2</sub> shows a gradual decrease in its absorbance intensity, while C<sub>max3</sub> displays a steady increase. In the single-REE monazite series, these changes correspond to increasing atomic numbers of the REEs, while in the double-REE series, the changes occur as the content of Nd and Sm within the mineral increases (see peaks at ~580 cm<sup>-1</sup> and ~560 cm<sup>-1</sup> in Figure 4.5, 4.6, and 4.7).

Therefore, this trend can be validated by calculating the ratio for relative change of the absorbance intensities between the two maxima features using the following equation:

$$\text{Relative change} = \frac{\text{Intensity}_{\text{Left maxima}} - \text{Intensity}_{\text{Right maxima}}}{\text{Intensity}_{\text{Reference minima}}}$$

The result of this equation reveals how the absorbance intensities of two maxima change relatively to each other. Positive result indicates that the intensity of the left maxima is greater than that of the right maxima, while negative result indicates that the intensity of the right maxima is higher. A result of zero means the intensities of the two features are relatively the same. For this analysis, feature C<sub>max2</sub> is designated as the left maxima and C<sub>max3</sub> as the right maxima. For the reference minima, C<sub>min2</sub> is selected because it is shared by both of the target maxima.

The results of the calculation reveal a systematic increase in the relative change between the intensities of features C<sub>max2</sub> and C<sub>max3</sub> as the atomic number of REEs increase in single-REE monazites (Figure 5.5, Left). This trend indicates that the intensity of C<sub>max3</sub> progressively increases. The trend of single-REE monazite from Sample Set 1 shows a highly linear correlation, except for monazite-(Ce), which shows the value close to zero, meaning that the intensities of these two features are relatively the same. Additionally, a similar decreasing trend is also observed within Sample Set 2.

For double-REE monazites, the plot results confirm that the absorbance intensities between the two features change in a similar way to the single-REE series, as Nd and Sm content within the mineral increases. The plots reveal that the trend of the La<sub>1-x</sub>Nd<sub>x</sub> decreases linearly when the molar ratio of Nd

gets higher, similar to the  $\text{La}_{1-x}\text{Sm}_x$  series. However, the relative change between  $C_{\text{max}2}$  and  $C_{\text{max}3}$  features of monazite- $(\text{La}_{1-x}\text{Sm}_x)$  tend to develop a non-linear trend, characterized by a polynomial relationship. A significant rate of decrease is observed when the molar ratio of Sm is less than 0.5, while the trend becomes more subtle when the Sm molar ratio exceeds 0.5 (Figure 5.5, Middle and Right)

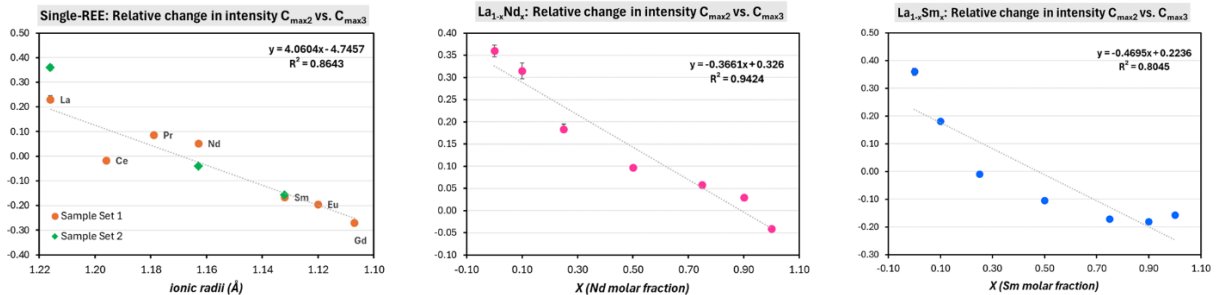


**Figure 5.5** Scatter plots showing how intensities between two local features: Feature  $C_{\text{max}2}$  and  $C_{\text{max}3}$  change relatively with different REE contents in synthetic monazites (**Left**) Single-REE monazites (from Sample Set 1 and 2), (**Middle**)  $\text{La}_{1-x}\text{Nd}_x$  monazites, and (**Right**)  $\text{La}_{1-x}\text{Sm}_x$  monazites. The single-REE data is plotted against ionic radii of  $\text{REE}^{3+}$  (CN = 9; Shannon, 1976), while double-REE data are plotted against molar fraction of Nd and Sm respectively. The trendline and correlation coefficient in single-REE plot correspond to Sample Set 1. Error bars indicates the minimum and maximum values obtained from the repeated measurement spectra of each sample.

#### 5.2.4. Changes in the number of detectable features

The number of detectable local features within feature group A (in the region of wavenumbers 1100 – 980  $\text{cm}^{-1}$ ) shows a clear variation with the changes in REE contents within the synthetic monazite samples. Using the feature extraction methods in this study, the local features are detectable only when clear vertex points in the absorbance intensity of the spectra are present. Undetectable features tend to appear as weak shoulders, lacking distinct changes in spectral intensities. In contrast, the features with strong intensity and well-defined shapes are more easily detected by the algorithm.

In this study, variations in number of detectable features are observed in both synthetic samples of single-REE and double-REE monazite. However, no clear pattern is seen in single-REE monazite samples. From Figure 5.6 (Left), the only conclusion that can be drawn is that samples containing lower atomic number REEs (La to Nd) exhibit several sharp and distinct features, whereas these sharp features become weak or absent in samples with higher atomic number REEs, especially in monazite-(Sm).

The spectra of single-REE monazite show an unpredictable number of detectable features, even among the spectra of monazite-(La) and monazite-(Nd) from Sample Set 1 and 2 (Figure 5.6; Left and Middle). These samples exhibit different numbers of detectable features despite having the same REE content. This observation suggests that the variation in the number of detectable features may be influenced by external factors rather than the mineral's chemical composition. The external factor considered in this case is the temperature during the thermal treatment process in the synthetic experiments. Detailed observations of the local features within the TIR spectra of orthophosphate compounds were conducted. The TIR spectra of monazite from the studies by De Sousa Filho & Serra (2008) and Anfimova et al. (2014) reveal that local features in this region tend to become more distinct with increasing temperature during the thermal treatment process.

In contrast with single-REE monazites, double-REE monazite samples, both  $\text{La}_{1-x}\text{Nd}_x$  and  $\text{La}_{1-x}\text{Sm}_x$  series, show a systematic decrease in the number of detectable features. From the spectra, we can see that the local features within this interested region become weaker as the content of Nd and Sm increases



(Figure 5.6; Left and Right). This suggests that incorporating higher atomic number REEs into the mineral may also impact the presence of these features (Figure 5.6, Middle and Right).

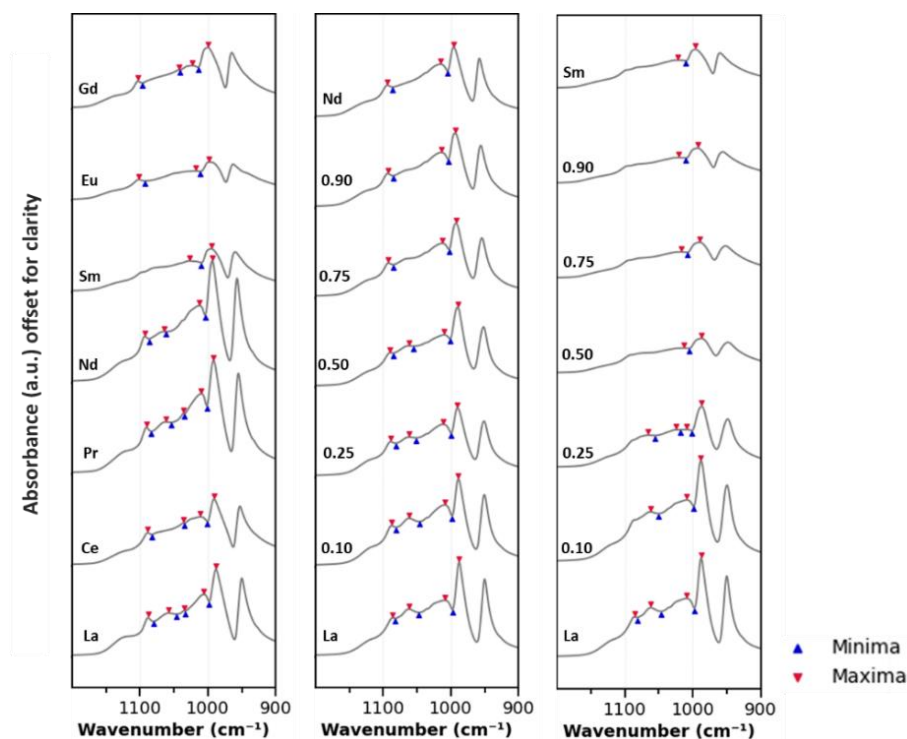


**Figure 5.6** TIR spectra from wavenumbers 1200 – 900  $\text{cm}^{-1}$  of (Left) synthetic single-REE monazites (La to Gd) from *Sample Set 1*. (Middle)  $\text{La}_{1-x}\text{Nd}_x$  and single-REE: La and Nd monazites from *Sample Set 2*. (Right)  $\text{La}_{1-x}\text{Sm}_x$  and single-REE: La and Sm monazites from *Sample Set 2*. The spectra are stacked for comparison. Triangle symbol indicates all detectable local features using second-degree polynomial fitting method (blue = minima, red = maxima). The spectra of double-REE monazites show systematic decrease in the number of detectable features, indicating a gradual weakening of local features in this region as the content of Nd and Sm within the mineral increases.

### 5.2.5. Shifts in spectral feature positions

Previous studies on the TIR spectra of single-REE monazites by Hezel & Ross (1966), Kijkowska et al. (2003), Silva et al. (2006), and Heuser et al. (2014) have reported the observation of systematic positional shifts in the wavenumbers of the maxima features. These shifts trend toward higher wavenumbers as the atomic number of REEs increases in single-REE synthetic monazites, corresponding to the effects of lanthanide contraction (i.e., the gradual decrease in ionic radii of REEs as atomic number increases) as reported in the literature.

Our study confirms these findings through the results obtained from feature extraction. Additionally, we also found that these systematic shifts occur not only in the maxima features but also in the minima features of the absorbance TIR spectra (see *Appendix V*).

The positions of all selected local features in the feature group A, B, and C show strong correlation of the slight shifts as the REE contents within the mineral changes (with average  $R^2$  values of 0.86 for single-REE series, 0.93 for  $\text{La}_{1-x}\text{Nd}_x$  series, and 0.98 for  $\text{La}_{1-x}\text{Sm}_x$  series). Consistent with previous reports, these shifts appear to be systematic. In single-REE monazites, the shifts systematically move toward higher wavenumbers as the atomic number of REEs increases (see Figure 4.5). Moreover, we also observed the same pattern in double-REE series as the content of Nd and Sm increases (see Figure 4.6 and 4.7).

For single-REE monazites, the trend of positional shifts is generally linear in almost every studied features. These shifts are very small, usually around 1 – 2  $\text{cm}^{-1}$  difference, when compared to the positions of the same features between the spectra of monazites containing REE with adjacent atomic numbers. However, each selected feature shows a different degree of correlation (indicated by  $R^2$  value) when comparing the position of a specific local feature with size of ionic radii of  $\text{REE}^{3+}$ . After plotting the positions of every features, we found that the minima features tend to show stronger linear correlation compared to the maxima features (see *Appendix V*).

Furthermore, when comparing the positions of the selected features between the spectra of monazite-(La), (Nd), and (Sm) from Sample Set 1 and 2, our results show that 10 out of 14 selected features show noticeable positional variations. This indicates that samples with the identical REE contents, but obtained from different synthetic experiments, do not yield identical wavenumber positions. We also found that the minima features tend show higher consistency in wavenumber positions when making a comparison between these two sets of single-REE samples. Additionally, the results reveal that feature  $C_{\text{min}2}$  shows the strongest linear correlation in positional shifts and shows very high consistency in the positions of monazite-(La), (Nd), and (Sm) samples from both Sample Set 1 and 2 (Figure 5.7; Left).

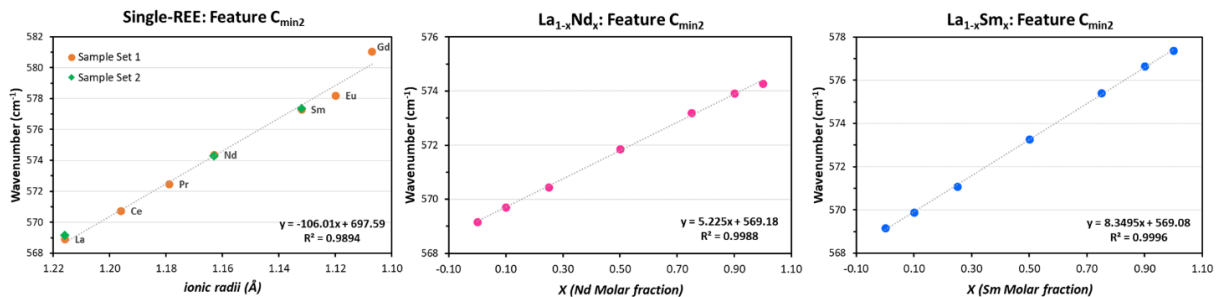


**Figure 5.7** Scatter plots showing a **strong linear correlation in the changes of feature  $C_{\text{min}2}$  position** with different REE contents in synthetic monazites. **(Left)** Single-REE monazites (from Sample Set 1 and 2), **(Middle)**  $\text{La}_{1-x}\text{Nd}_x$  monazites, and **(Right)**  $\text{La}_{1-x}\text{Sm}_x$  monazites. The single-REE data is plotted against ionic radii of  $\text{REE}^{3+}$  (CN = 9; Shannon, 1976), while double-REE data are plotted against molar fraction of Nd and Sm respectively. The trendline and correlation coefficient in single-REE plot correspond to Sample Set 1. Error bars indicates the minimum and maximum values obtained from the repeated measurement spectra of each sample. In single-REE series, the features position of La, Nd, and Sm monazite from Sample Set 1 and 2 show very high consistency.

While the positional shifts in the local features of single-REE monazites generally show a linear increase with higher atomic numbers, the shifts in double-REE series follow different patterns. The analysis results show that not all local features show linear trend in positional shifts. In contrast, the shifting trends tend to exhibit more polynomial relationships as the contents of Nd and Sm within the mineral increases (see middle and right figures in *Appendix V*).

Based on the observations, positional shifts of minima features in the spectra of double-REE monazite samples tend to follow a linear trend (see the example in Figure 5.7; Middle and Right). In contrast, the maxima features often display a parabolic correlation. Additionally, the results indicate that the trend observed in  $\text{La}_{1-x}\text{Sm}_x$  series exhibits more pronounced parabolic curve compared to the  $\text{La}_{1-x}\text{Nd}_x$  series. It is noted that for some local features, this parabolic trend can be seen even though a strong linear correlation is observed in single-REE monazite series (Figure 5.8).

Another finding indicates that, while the positional shifts of a specific feature in single-REE monazite series show weak linear correlations, the parabolic correlations can still be observed in the spectra of double-REE monazite series, as shown in Figure 5.9.

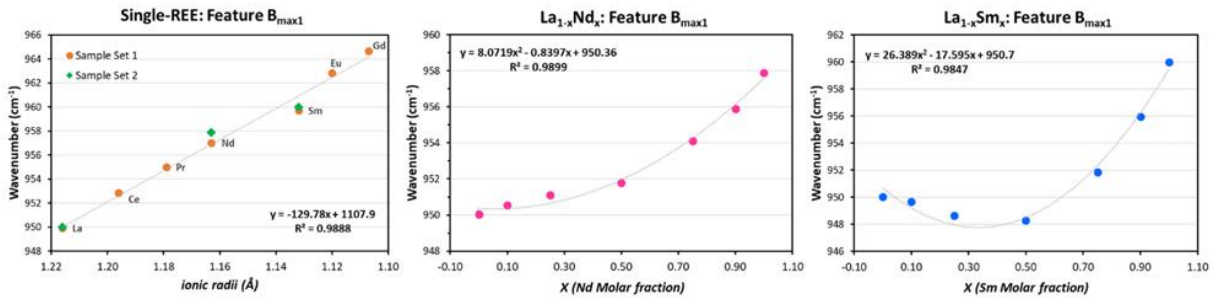


**Figure 5.8** Scatter plots showing example of a strong linear correlation in changes of feature B<sub>max1</sub> position, contrasted with a polynomial regression in double-REE monazites across different REE contents in synthetic monazites. **(Left)** Single-REE monazites (from Sample Set 1 and 2), **(Middle)** La<sub>1-x</sub>Nd<sub>x</sub> monazites, and **(Right)** La<sub>1-x</sub>Sm<sub>x</sub> monazites. The single-REE data is plotted against ionic radii of REE<sup>3+</sup> (CN = 9; Shannon, 1976), while double-REE data are plotted against molar fraction of Nd and Sm respectively. The trendline and correlation coefficient in single-REE plot correspond to Sample Set 1. Error bars indicates the minimum and maximum values obtained from the repeated measurement spectra of each sample. In single-REE series, the features position of La, Nd, and Sm monazite from Sample Set 1 and 2 show high consistency.

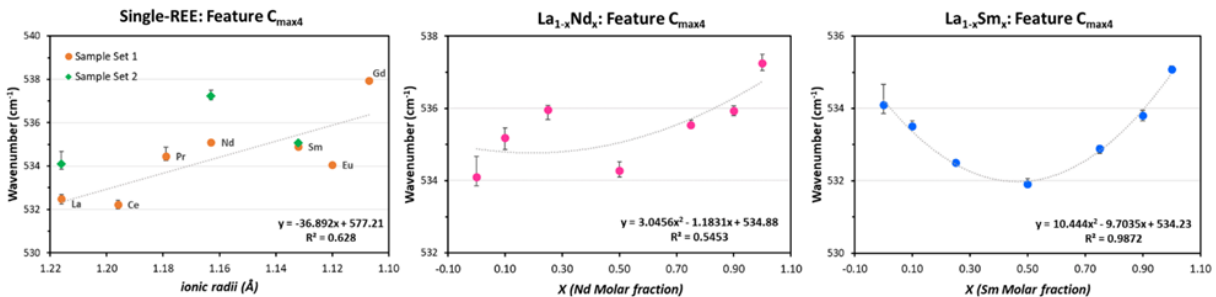


**Figure 5.9** Scatter plots showing example of a polynomial regression in double-REE monazites in feature C<sub>max4</sub> position, contrasted with the high deviation within a linear correlation in single-REE monazites across different REE contents in synthetic monazites. **(Left)** Single-REE monazites (from Sample Set 1 and 2), **(Middle)** La<sub>1-x</sub>Nd<sub>x</sub> monazites, and **(Right)** La<sub>1-x</sub>Sm<sub>x</sub> monazites. The single-REE data is plotted against ionic radii of REE<sup>3+</sup> (CN = 9; Shannon, 1976), while double-REE data are plotted against molar fraction of Nd and Sm respectively. The trendline and correlation coefficient in single-REE plot correspond to Sample Set 1. Error bars indicates the minimum and maximum values obtained from the repeated measurement spectra of the sample. In single-REE series, the features position of La and Nd monazite from Sample Set 1 and 2 show differences.

### 5.3. Difference in TIR spectra of single-REE monazite (REE = La, Nd, Sm) from Sample Set 1 and 2

The detailed analysis on the spectra of synthetic single-REE monazites reveals that although the chemical composition and REE contents within single-REE monazite samples (REE = La, Nd, and Sm) from Sample Sets 1 and 2 are identical, since each synthetic monazite sample consists of 0.005 mol REE in both Sample Set. Their TIR spectra show several variations in the spectral features. These include the variation in overall absorbance intensity, spectra shape, and the positional shifts in some local features

The significant differences between the TIR spectra of the same single-REE monazite samples from the two sample sets are seen in the spectra of monazite-(Nd) and monazite-(Sm) from Sample Set 2. These samples exhibit weaker absorbance intensities and less distinct shapes of local features compared to those from Sample Set 1 (Figure 5.10, Left). These less distinct features in the TIR spectra suggest lower crystallinity. To confirm this assumption, the XRD results were analysed. The XRD patterns of monazite-(Nd) and monazite-(Sm) from Sample Set 2 show broader peaks compared to those from Sample Set 1 (Figure 5.10, Right), supporting the conclusion of lower crystallinity.

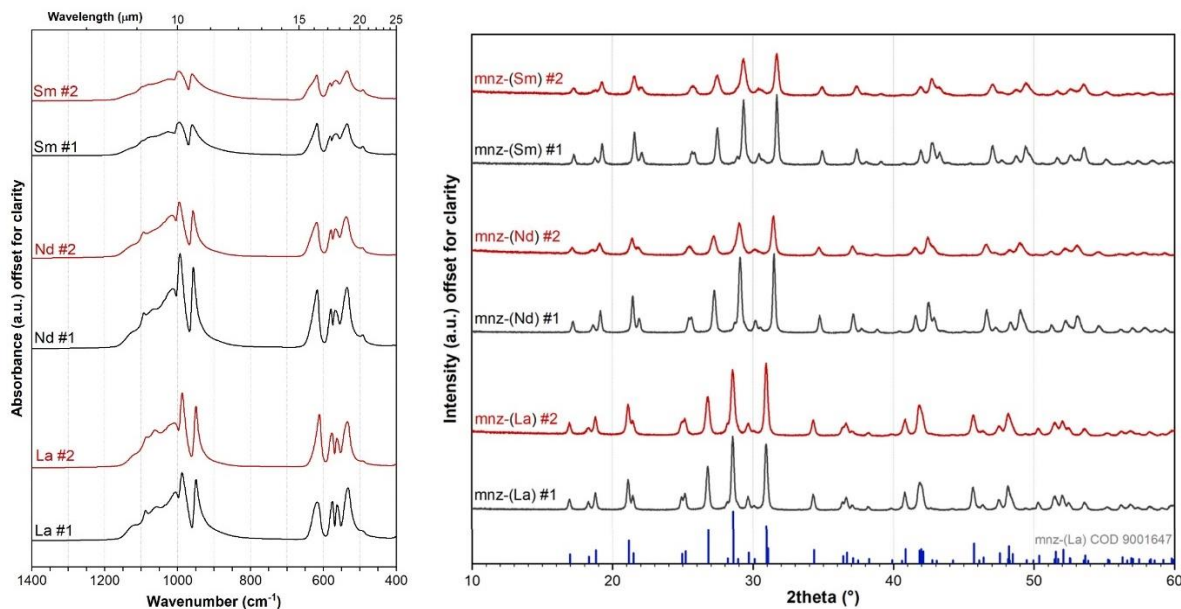


**Figure 5.10 (Left)** TIR spectra of single-REE monazites (REE = La, Nd, and Sm) from Sample Set 1 (black, synthesized as part of the work of Dijkstra et al., 2024) and Sample Set 2 (red, synthesized in this study). **(Right)** XRD patterns of single-REE monazites (REE = La, Nd, and Sm) from Sample Set 1 (black, data from Dijkstra et al., 2024) and Sample Set 2 (red). Note that the monazites from these two sample sets are identical in chemical composition and REE contents (with 0.005 mol REE for each sample). The data are stacked to enable comparison between samples. The TIR spectra show significant weakening in spectral features in monazite-(Nd) and (Sm) spectra from Sample Set 2. The XRD data show significant peak broadening in monazite-(Nd) and (Sm) from Sample Set 2 as compared Sample Set 1.

These findings led to a deeper investigation into the causes of the difference in degree of crystallinity of the synthetic monazite samples between the two sample sets. We believe that minor variations during the synthetic process could account for these differences. After discussing with Dr. A.H. Dijkstra who conducted the synthesis experiments for Sample Set 1, we believe that there are two possible reasons for the lower crystallinity observed in monazites from Sample Set 2 have been identified:

First, the different methods were used for washing H<sub>3</sub>PO<sub>4</sub> acid during the synthetic of rhabdophane. In the synthesis experiments of Sample Set 1, filter paper was used while neutralizing the product. Consequently, the rhabdophane particles smaller than 2 μm were sorted out. In contrast, the centrifugation technique was used in the synthesis of Sample Set 2. This resulted in a mixture of both large and fine particles in the obtained rhabdophane.

Second, procedures of collecting the final monazite product after thermal treatment differed. For Sample Set 2, the monazite products were removed from the muffle furnace quickly, while in Sample Set 1, the products were left to cool down inside the furnace before being taken out. This abrupt cooling in Sample Set 2 may have caused interruptions in crystallinity, leading to minor crystallographic disorders in monazite-(Nd) and monazite-(Sm).

Despite the noticeable differences in the spectra of the two monazite samples, which have identical REE contents but varying degrees of crystallinity, certain spectral features remain consistent. As discussed in *Chapter 5.2*, we found that the wavenumber positions of one local features remained unchanged as the REE contents within the mineral of the two different samples are the same. This particular feature is feature C<sub>min2</sub>.

To summarize, based on the results of our study, one of the most reliable features is  $C_{\min 2}$  as the position show almost identical in both sample sets (Figure 5.7). Additionally, two other features,  $B_{\min 1}$  and  $B_{\max 1}$ , also exhibit significant consistency. Although the positions of these two local features do not completely overlap between the two different samples (unlike feature  $C_{\min 2}$ ). However, due to their high consistency when compared to other features within the spectra, they can still serve as potential alternative features for the further study of the influence of REE in the TIR spectra of monazites, especially for hyperspectral imaging spectroscopy study, since the maximum limit of LWIR HSI camera currently available is only around 12  $\mu\text{m}$  due to the atmospheric windows (Itakura et al., 1974; Laakso et al., 2019)

#### 5.4. The influence of REEs on TIR spectra of monazite

After comparing the spectra of our synthetic single-REE monazites with previous studies by Hezel & Ross (1966) and Heuser et al. (2014), we believe that the ‘direct influence’ of REEs on the TIR spectra of monazite leads to positional shifts in the wavenumber of the local features from fundamental vibration of  $\text{PO}_4$  within the mineral. Interestingly, despite differences in synthetic methods, conditions, and starting materials across these studies, the reported wavenumbers of certain features show a strong linear trend with only minor deviations when compared to our study (Figure 5.11). This consistency suggests that the observed behaviour is indeed due to the presence and variation of REEs within the minerals.

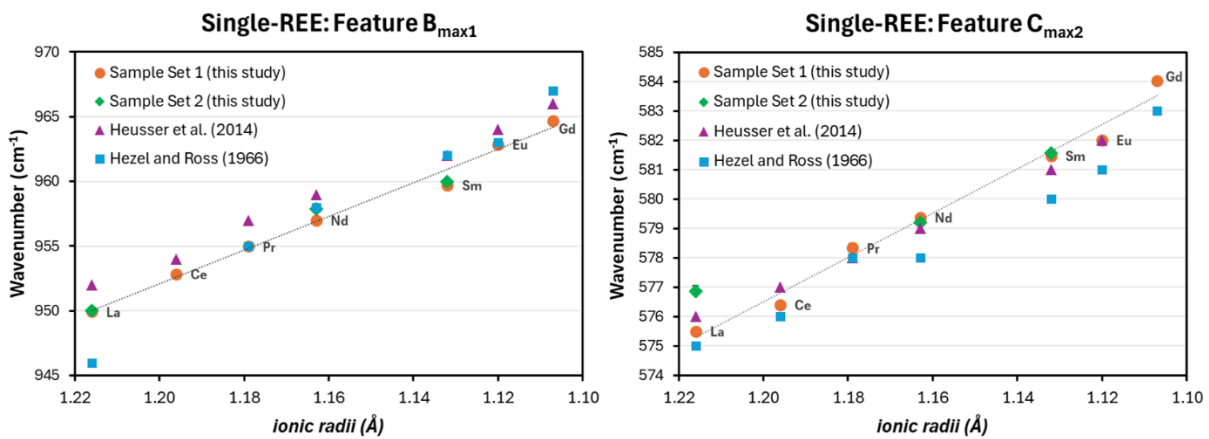


**Figure 5.11** Scatter plots show the comparison of reported wavenumber of positional shifts in (Left)  $B_{\max 1}$  feature (Right)  $C_{\max 2}$  features in TIR spectra of synthetic single-REE monazites. The wavenumbers obtained from both Sample Set 1 (REE = La to Gd) and Sample Set 2 (REE = La, Nd, and Sm) in this study are plot along with the wavenumbers reported in Hezel & Ross (1966) and Heuser et al. (2014). The trendline in both plots correspond to Sample Set 1. Both selected features show similar linear trend of positional shift with little deviation between each study. Note that feature  $C_{\max 2}$  is not detectable in monazite-(Gd) the report of Heuser et al. (2014).

As mentioned in the literature, the positional shifts between these local features are due to lanthanide contraction, where the ionic radii of  $\text{REE}^{3+}$  decrease as the atomic number increases. For single-REE monazite, this contraction shortens the [REE]-O bond length in the crystal lattice of the minerals as can be observed in the XRD refinement results from Ni et al. (1995). Additionally, Hirsch et al. (2017) also observed shifts in the vibrational band within Raman spectra of double-REE monazites (REE =  $\text{La}_{1-x}\text{Pr}_x$ ). They noted that as the Pr content in the monazite increases, the Raman spectra shift to higher wavenumbers. They believe this is because the different amounts of La and Pr cause the average [REE]-O bond length to shorten in the monazite molecule. As a result, the shorter [REE]-O bond length leads to a higher vibrational frequency of the  $\text{PO}_4$  molecules (Hirsch et al., 2017; Heuser et al., 2019).

In addition, we believe that another ‘direct influence’ of REEs on the TIR spectra of monazite is the systematic change in the relative intensities between features  $C_{\max 2}$  and  $C_{\max 3}$ , as discussed in *Chapter 5.2.3*. When comparing our spectra (Figure 4.5, 4.6, and 4.7) with those from other studies (Kijkowska et al., 2003; Heuser et al., 2014; Hirsch et al., 2017; Heuser et al., 2019), we found it was challenging to compare our spectra with those from these studies due to differences in spectral shapes obtained using ATR-FTIR (used in our study) and traditional FTIR methods (used in other studies). To be more specific, in ATR-FTIR spectra, these features appear as two distinct and well-defined features, whereas in transmission spectra, they sometimes appear as a single features that splits into two features and become more distinct as the atomic number of the REE decreases. Therefore, the relative intensity of these splitting features changes similarly to our observations (See Kijkowska et al., 2003 and Heuser et al., 2014). These splitting of  $C_{\max 2}$  and  $C_{\max 3}$  was reported in Heuser et al. (2014) and Heuser et al. (2019), attributing this to the distortion of  $\text{PO}_4$  tetrahedra within monazite molecule due to the decreasing ionic radii of REEs, a result of lanthanide contraction.

In *Chapter 5.2*, we discussed various changes in the TIR spectra of monazite with different REE contents. However, we believe that changes in absorbance intensity and sharpness of local features are not due to the ‘direct influence’ of REEs. Instead, these changes might come from the ‘indirect influence’ of REEs on mineral properties. Absorbance intensity and sharpness in TIR spectra are sensitive to the mineral's crystallinity. We propose that incorporating REEs with higher atomic numbers (such as Sm, Eu, and Gd) may affect the degree of crystallinity of the samples. As a result, minerals containing these higher atomic number REEs might require higher temperatures to achieve the same crystallinity as those with lower atomic number REEs, like La or Pr.

## 5.5. Comparison between the TIR spectra of synthetic and natural monazite samples

Comparisons were made between the TIR spectra of laboratory-synthesized monazites in this study and natural monazite samples. The synthetic samples include single-REE monazite from this study and ‘natural-like’ monazite synthesized by Dijkstra et al. (2024). For natural monazite, we used a sample from the ITC collections (also used in the study of Dijkstra et al., 2024), along with additional spectra downloaded from online database: RRUFF (Lafuente et al., 2016; RRUFF ID: R040106) and the USGS spectral library (Kokaly et al., 2017; Spectrum title: HS255.3B NIC4bbb RREF). Notably, all TIR spectra, except for the USGS sample, were acquired using ATR-FTIR spectroscopy. The USGS monazite spectrum was recorded using diffuse reflectance infrared Fourier transform spectroscopy (DRIFTS), resulting in some variations in the shape of the monazite spectral features due to the different acquisition techniques. Additionally, the sampling resolutions vary for each spectrum, which might cause a weakening of spectral features if the sampling resolution is significantly lower than another. Details regarding the spectra acquisition settings and the chemical composition of each sample are provided in Table 5.1.

Sample	Type	Compositions	Acquisition	Resolution	Remark
Single-REE	Synthetic	$\text{LaPO}_4$	ATR	$2 \text{ cm}^{-1}$	Sample Set 1
Natural-like	Synthetic	$(\text{La}_{0.68}, \text{Pr}_{0.06}, \text{Nd}_{0.18}, \text{Sm}_{0.06}, \text{Dy}_{0.02})\text{PO}_4$	ATR	$4 \text{ cm}^{-1}$	Dijkstra et al. (2024)
ITC	Natural	unknown	ATR	$4 \text{ cm}^{-1}$	Dijkstra et al. (2024)
RRUFF	Natural	$(\text{Ce}_{0.41}, \text{La}_{0.17}, \text{Nd}_{0.17}, \text{Th}_{0.14}, \text{Ca}_{0.06}, \text{Y}_{0.04}) (\text{P}_{0.95}, \text{Si}_{0.05}) \text{O}_4$	ATR	unknown	R040106
USGS	Natural	$(\text{Ce}, \text{La}, \text{Nd}, \text{Th})\text{PO}_4$	DRIFTS	$4 \text{ cm}^{-1}$	HS255.3B NIC4bbb RREF

**Table 5.1** Chemical composition detail of each monazite sample and TIR spectra acquisition technique

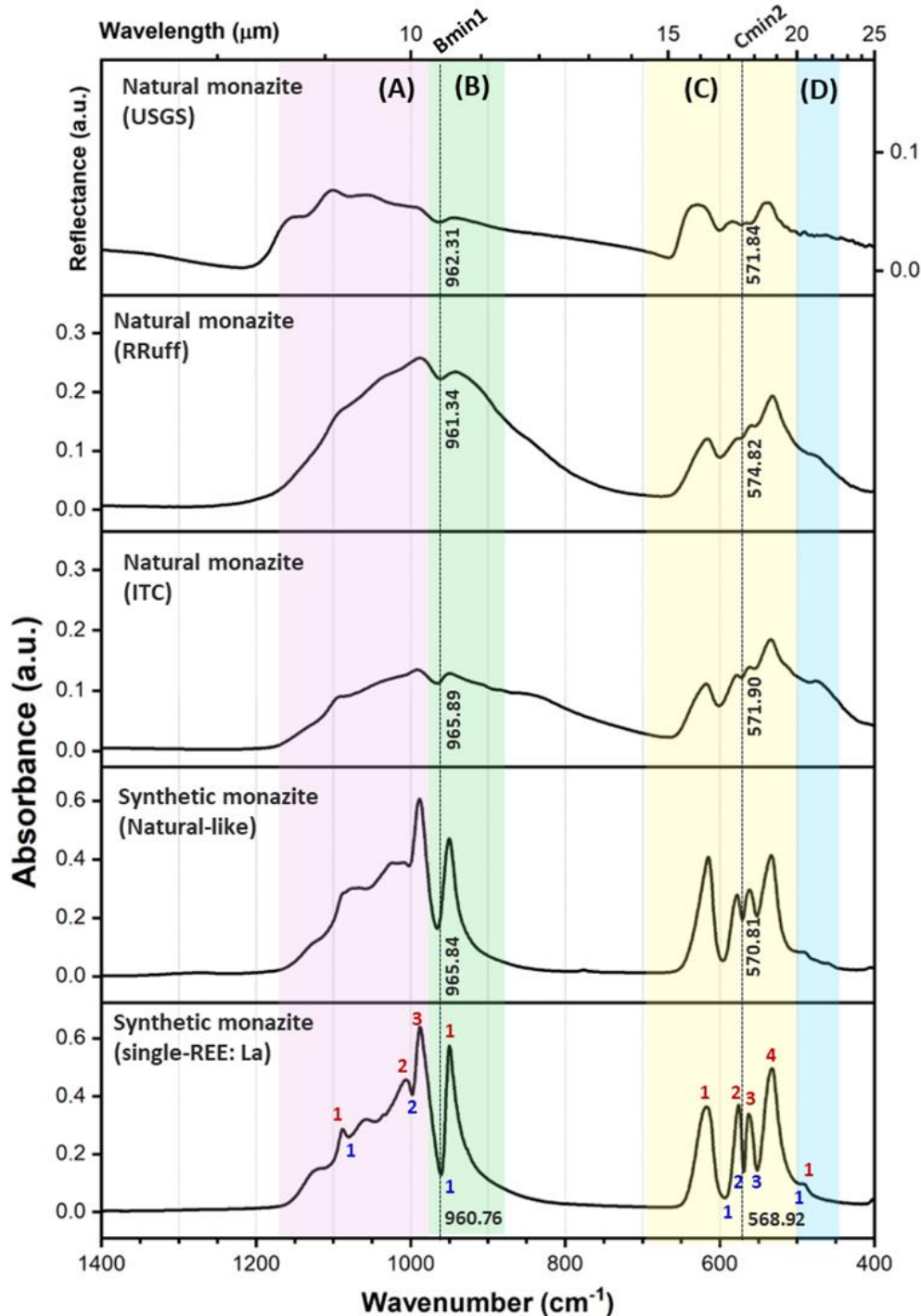


**Figure 5.12** TIR spectra TIR absorbance spectra from wavenumbers 1400 – 400  $\text{cm}^{-1}$  (wavelengths 7.14 – 25  $\mu\text{m}$ ) of (From bottom to top) synthetic monazite-(La) from Sample Set 1, synthetic natural-like monazite (synthesized as part of the work of Dijkstra et al., 2024), natural monazite from ITC collection (used as part of the work of Dijkstra et al., 2024), natural monazite from RRUFF database (RRUFF ID: RA040106), and natural monazite from USGS spectral library (Spectrum title: HS255.3B NIC4bbb RREF). The spectrum from USGS was recorded using DRIFTS technique, while the rest were recorded with ATR-FTIR technique. Local features belonging to each feature group are highlighted: pink - group A, green - group B, yellow - group C, and blue - group D. The selected features for the further analysis are annotated and numbered, with ‘red’ for maxima and ‘blue’ for minima on the spectra of monazite-(La). The spectra are stacked to enable comparison between samples, allowing for better observation of small variations in shape, absorbance intensity and positional shifts of the spectral features. All spectra are displayed in absorbance mode, except USGS spectra displayed in reflectance. Reference lines are drawn at features Bmin1 and Cmin2 within the spectra to aid in observing shifts in feature positions. The numbers to the left of each reference line indicate the wavenumber positions of these features obtained from parabolic fitting method.

In Figure 5.12, despite differences in spectral features due to varying sampling techniques, it is clear that the absorbance intensities of both synthetic monazites are higher than those of the natural samples. Two strong intensity bands correspond to the stretching ( $\nu$ ) and bending mode ( $\delta$ ) of  $\text{PO}_4$  (at between  $1200 - 900 \text{ cm}^{-1}$  and  $700 - 475 \text{ cm}^{-1}$  respectively) which are considered diagnostic features of monazite in the TIR region can still be observed. However, a significant difference is the absence of several local features within the spectra, especially for feature group A (highlighted with pink in Figure 5.12), of the natural samples. The possible cause of this absence is discussed further in this subchapter.

Although several features are missing in natural monazite spectra, some major local features can still be observed. In the range between  $1200 - 900 \text{ cm}^{-1}$ , feature  $B_{\text{min}1}$  can be seen as the most prominent feature in this range. However, the feature appears shallower and less sharp compared to the feature within the synthetic samples. Positional shifts of this feature are noticeable, ranging from  $960.75 \text{ cm}^{-1}$  in synthetic monazite-(La) to  $965.89 \text{ cm}^{-1}$  in natural monazite from ITC collection. This observation is consistent with the findings of our study, where local features shift toward higher wavenumbers when REEs with atomic numbers higher than La are incorporated into the monazite mineral. However, it is important to note that this shift might also result from the different resolutions used in acquiring the spectra. To accurately confirm the shift, we recommend recording the spectra of natural monazite with a  $2 \text{ cm}^{-1}$  sampling resolution.

Moving to the range of  $700 - 475 \text{ cm}^{-1}$ , it can be observed in Figure 5.12 that the local features within the natural monazite spectra maintain more well-defined shapes. The two local features,  $C_{\text{max}2}$  and  $C_{\text{max}3}$ , which we believe indicate the direct influence of REE on the spectra of monazite, can still be observed, although they are very weak. By applying a second-degree polynomial fitting algorithm to the spectra, we can still get the interpolated local minima values from feature  $C_{\text{min}1}$ . Based on our finding, we suggest that  $C_{\text{min}1}$  is one of the most reliable features among all those selected in our study. This could provide a good opportunity for further investigation of this particular feature. Additionally, this feature also shows subtle positional shifts, ranging from  $568.92 \text{ cm}^{-1}$  in synthetic monazite-(La) to  $574.82 \text{ cm}^{-1}$  in natural monazite from RRUFF database, confirming that the shift observed in feature  $B_{\text{min}1}$  also occurs in feature  $C_{\text{min}1}$ .

However, it is crucial to note that, compared to the ideal chemical conditions in synthetic monazite, the chemical composition of natural monazites is significantly more complex. They can contain cationic tetravalent radioactive elements, like thorium (Th), and other divalent cations such as calcium (Ca), which can be substituted into the monazite crystal lattice due to their compatible ionic radii with the crystal vacancies in monazite structures (Clavier et al., 2011). Furthermore, the study by Murata et al. (1957) on the variation of REEs in monazite reveals that some heavy rare earth elements (HREEs), including yttrium (Y), can also be present in natural monazite. These chemical complexities in natural samples suggest that our findings alone are insufficient for a complete understanding of the TIR spectral behaviour of the host mineral.

Several studies were conducted on observing the impact of radioactive contents on the TIR spectra of minerals and synthetic compounds (Zhang & Salje, 2001; Knyazev et al., 2021). These investigations have demonstrated that radioactive elements can degrade the spectra, leading to reduced sharpness and distorted the overall shape of the spectra as well. This degradation may be a reason of the significant differences observed between the natural and synthetic monazite spectra in our study.



Unfortunately, due to numerous unknown variables affecting the variation in the spectral features of monazite, we must acknowledge that the insights derived from our study may not be sufficient for accurately estimating the relative abundance of REEs in natural monazite. Knowing this would possibly help us ‘guess’ the positional shifts within the mineral's spectra. However, we still lack precise knowledge about the reference wavenumber positions of other single-element monazite compounds, such as  $\text{CaPO}_4$ ,  $\text{YPO}_4$ , and  $\text{ThPO}_4$ , which are critical as they frequently occur within monazite. Also, we have yet to fully determine the specific effects of radioactive elements on the spectra. We also don't fully know how radioactive elements affect the spectra.

Furthermore, we are uncertain how monazite spectra would respond to more complex REE compositions since natural monazite contains several species of REE within the host minerals (Table 5.1). These factors suggest that we do not have enough ‘known variables’ to accurately determine the relative abundance of various REEs in natural monazite using TIR spectra alone. However, the study by Murata et al. (1957) indicate that the variation of REEs in natural monazite is systematic, which might help narrow down the unknowns.

Nevertheless, we believe the findings from our study provide a foundational understanding of how REEs could influence the TIR spectra of the host minerals. We hope that our finding will enhance future research in spectral geology and support data integration efforts in the exploration of REEs. Importantly, our results have pinpointed specific spectral features that might be useful for further investigation in the future study.

## 6. CONCLUSION AND RECOMMENDATIONS

### 6.1. Conclusion

This study aimed to develop a fundamental understanding of how spectral features of REE-host mineral within the TIR range are influenced by different REE contents, focusing specifically on monazite.

1. In this study, rhabdophane, synthesized using the wet precipitation method, was used as a precursor to produce both single-REE and double-REE monazites. Following heat treatment at 800° for 6 hours, the final products were characterized as monazite based on the XRD results. Two series of monazites were synthesized: monazite-(La<sub>1-x</sub>Nd<sub>x</sub>) and monazite-(La<sub>1-x</sub>Sm<sub>x</sub>). Both series exhibited systematic shifts in their XRD patterns and linear changes in unit cell parameters. This indicates that the obtained products contain the desired amounts of REE(s) without any fractionation. The presence of Nd and Sm in the products could be confirmed using VNIR-SWIR reflectance spectroscopy.
2. TIR spectra were recorded using ATR-FTIR spectroscopy. The spectra in the 1400 – 400 cm<sup>-1</sup> region revealed diagnostic absorption features of PO<sub>4</sub> in monazite. Comparison with Hezel & Ross (1966) showed that the synthetic monazite exhibited all major vibration modes of PO<sub>4</sub>.
3. Detailed analysis of the TIR spectra revealed distinct trends in how the spectral features of PO<sub>4</sub> change with varying REE content. Systematic changes were observed in both single-REE and double-REE monazites. In single-REE monazites, these trends corresponded to lanthanide contraction, while in double-REE monazites, the trends corresponded to increases in Nd and Sm content. Trends included variations in absorbance intensity, feature shape, and positional shifts toward higher wavenumbers.
4. The systematic positional shifts in local features and the changes in relative absorbance intensity of specific features, C<sub>max2</sub> and C<sub>max3</sub>, in the asymmetric bending vibration ( $\delta_{as}$ ) region are believed to be due to the direct influence of REE, while changes in overall intensity of PO<sub>4</sub> features and sharpness of local features are likely the indirect influences of REE which may disrupt the crystallinity of the synthetic host mineral.
5. Feature extraction using second-degree polynomial fitting algorithm proved to be a robust method for identifying and analysing spectral features. Despite limitations in detecting weak shoulder features, this method provided precise positions for spectral maxima and minima, facilitating the identification of trends and correlations within the spectra of synthetic monazites.
6. The application on estimating the relative abundance of REEs using TIR spectra of natural monazite remains unfeasible due to the many unknown variations and chemical complexities inherent in natural monazite.
7. Although our findings cannot yet be used to precisely estimate the relative abundance of REEs in REE-bearing minerals, particularly monazites, we believe this goal is still achievable. The TIR spectra still hold significant potential for REE estimation, and our findings provide a general understanding of how REEs influence the spectral features of host minerals. Therefore, future research should focus on the consistency and the positional shifts of feature C<sub>min2</sub>, as it has shown high reliability across both sample sets.

## 6.2. Recommendations

1. To develop a fundamental understanding of how REEs or other cations influence the TIR spectra of host minerals, further studies on synthetic minerals are recommended as the resulting knowledge can serve as a reference for predicting positional shifts in multi-REE monazites. Therefore, ATR-FTIR is recommended for spectral acquisition. This technique is less influenced by external factors, offers high consistency and reproducibility, requires minimal sample preparation, and eliminates concerns about sample compaction.
2. To achieve the objective of using TIR spectra to estimate the relative abundance of REEs in host minerals, it is essential to synthesize more complex synthetic multi-REE samples to develop baseline understanding on how the presence of complex REE with different species and different ratios can influence changes of host minerals' spectral features, especially the positional shift of feature  $C_{\min 2}$ . Additionally, more synthetic 'natural-like' monazites should be synthesized to mimic the REE content of natural monazite samples, based on geochemical analyses like EPMA. This can simplify the mineral and chemical complexity of the host minerals. Furthermore, synthetic minerals exhibit more well-defined spectral features compared to natural samples, facilitating the observation of spectral changes.
3. Differences in the spectral features of chemically identical single-REE monazites from Sample Sets 1 and 2 highlight the need to synthesize a complete series of single-REE monazites. This would help verify if the reliable features identified in this study remain consistent in position. To ensure the final products from different synthesis conditions yield consistent results, various synthesis pathways. Additionally, systematic testing of the effects of heating (annealing) and applying high pressure on the synthetic process of monazites should be conducted to observe changes and ensure the consistency of the positions of the  $C_{\min 2}$  features
4. Variations in particle size might contribute to differences in the TIR spectra of monazite. Scanning electron microscopy analysis will provide data on the particle size of the synthetic powders, aiding in the understanding of how particle size could impact on spectral features.
5. TIR spectra obtained from different acquisition methods may exhibit positional shifts and spectral features distortions. While the findings of this study offer guidelines on how REEs influence TIR spectra, the reported wavenumber positions might not be accurate when compared with other methods like LWIR hyperspectral imaging spectroscopy. To ensure precise wavenumber measurements, it is recommended to use the same instrument for acquiring spectra from synthetic single-REE monazites and use the wavenumbers of the local features positions as the references for further analysis on the target materials.
6. A comprehensive database of TIR spectra for synthetic compounds that closely resemble the crystallography and chemistry of REE host minerals should be developed and shared to expand collective knowledge. However, standardized protocols for reporting data should be established, always including the acquisition techniques and sampling resolution.

## LIST OF REFERENCES

---

- Anfimova, T., Li, Q., Jensen, J. O., & Bjerrum, N. J. (2014). Thermal Stability and Proton Conductivity of Rare Earth Orthophosphate Hydrates. *International Journal of Electrochemical Science*, 9(5), 2285–2300. [https://doi.org/10.1016/S1452-3981\(23\)07927-0](https://doi.org/10.1016/S1452-3981(23)07927-0)
- Asadzadeh, S., & de Souza Filho, C. R. (2016). A review on spectral processing methods for geological remote sensing. *International Journal of Applied Earth Observation and Geoinformation*, 47, 69–90. <https://doi.org/10.1016/J.JAG.2015.12.004>
- Balaram, V. (2019). Rare earth elements: A review of applications, occurrence, exploration, analysis, recycling, and environmental impact. *Geoscience Frontiers*, 10(4), 1285–1303. <https://doi.org/10.1016/j.gsf.2018.12.005>
- Bart, S. C. (2023). What is the “Lanthanide Contraction”? *Inorganic Chemistry*, 62(9), 3713–3714. <https://doi.org/10.1021/ACS.INORGCHEM.3C00440>
- Beasley, M. M., Bartelink, E. J., Taylor, L., & Miller, R. M. (2014). Comparison of transmission FTIR, ATR, and DRIFT spectra: implications for assessment of bone bioapatite diagenesis. *Journal of Archaeological Science*, 46(1), 16–22. <https://doi.org/10.1016/J.JAS.2014.03.008>
- Begun, G. M., Beall, G. W., Boatner, L. A., & Gregor, W. J. (1981). Raman spectra of the rare earth orthophosphates. *Journal of Raman Spectroscopy*, 11(4), 273–278. <https://doi.org/10.1002/jrs.1250110411>
- Chen, Y., Zou, C., Mastalerz, M., Hu, S., Gasaway, C., & Tao, X. (2015). Applications of Micro-Fourier Transform Infrared Spectroscopy (FTIR) in the Geological Sciences—A Review. *International Journal of Molecular Sciences* 2015, Vol. 16, Pages 30223-30250, 16(12), 30223–30250. <https://doi.org/10.3390/IJMS161226227>
- Christensen, P. R., Bandfield, J. L., Hamilton, V. E., Howard, D. A., Lane, M. D., Piatek, J. L., Ruff, S. W., & Stefanov, W. L. (2000). A thermal emission spectral library of rock-forming minerals. *Journal of Geophysical Research: Planets*, 105(E4), 9735–9739. <https://doi.org/10.1029/1998JE000624>
- Chukanov, N. V. (2014). *Infrared spectra of mineral species*. Springer Netherlands. <https://doi.org/10.1007/978-94-007-7128-4>
- Clark, R. N. (1999). Spectroscopy of Rocks and Minerals, and Principles of Spectroscopy. In: Rencz, A.N. & Ryeson, R.A. (eds) Spectroscopy of Rocks and Minerals, and Principles of Spectroscopy, *Manual of remote sensing, volume 3, Remote Sensing for the Earth Sciences*, John Wiley and Sons
- Clark, R. N., King, T. V. V., Klejwa, M., Swayze, G. A., & Vergo, N. (1990). High spectral resolution reflectance spectroscopy of minerals. *Journal of Geophysical Research: Solid Earth*, 95(B8), 12653–12680. <https://doi.org/10.1029/JB095iB08p12653>
- Clavier, N., Mesbah, A., Szenknect, S., & Dacheux, N. (2018). Monazite, rhabdophane, xenotime & churchite: Vibrational spectroscopy of gadolinium phosphate polymorphs. *Spectrochimica Acta Part A: Molecular and Biomolecular Spectroscopy*, 205, 85–94. <https://doi.org/10.1016/j.saa.2018.07.016>
- Clavier, N., Podor, R., & Dacheux, N. (2011). Crystal chemistry of the monazite structure. *Journal of the European Ceramic Society*, 31(6), 941–976. <https://doi.org/10.1016/J.JEURCERAMSOC.2010.12.019>
- De Sousa Filho, P. C., & Serra, O. A. (2008). Tripolyphosphate as precursor for REPO<sub>4</sub>:Eu<sup>3+</sup> (RE = Y, La, Gd) by a polymeric method. *Journal of Fluorescence*, 18(2), 329–337. <https://doi.org/10.1007/S10895-007-0272-3/TABLES/2>
- Dijkstra, A. H., Bakker, W. H., Deon, F., Marcatelli, C., Plokker, M. P., & Hintzen, H. T. (2024). Identification of rare earth elements in synthetic and natural monazite and xenotime by visible-to-

- shortwave infrared reflectance spectroscopy. *Physics and Chemistry of Minerals* 2024 51:2, 51(2), 1–19. <https://doi.org/10.1007/S00269-024-01284-7>
- Eid, M. M. (2022). Characterization of Nanoparticles by FTIR and FTIR-Microscopy. *Handbook of Consumer Nanoproducts*, 645–673. [https://doi.org/10.1007/978-981-16-8698-6\\_89](https://doi.org/10.1007/978-981-16-8698-6_89)
- Farmer, V. C. (1974). The Infrared Spectra of Minerals. In *The Infrared Spectra of Minerals*. Mineralogical Society of Great Britain and Ireland. <https://doi.org/10.1180/MONO-4>
- Heuser, J., Bukaemskiy, A. A., Neumeier, S., Neumann, A., & Bosbach, D. (2014). Raman and infrared spectroscopy of monazite-type ceramics used for nuclear waste conditioning. *Progress in Nuclear Energy*, 72, 149–155. <https://doi.org/10.1016/J.PNUCENE.2013.09.003>
- Heuser, J. M., Neumeier, S., Peters, L., Schlenz, H., Bosbach, D., & Deissmann, G. (2019). Structural characterisation of metastable Tb- and Dy-monazites. *Journal of Solid State Chemistry*, 273, 45–52. <https://doi.org/10.1016/J.JSSC.2019.02.028>
- Hezel, A., & Ross, S. D. (1966). Forbidden transitions in the infra-red spectra of tetrahedral anions—III. Spectra-structure correlations in perchlorates, sulphates and phosphates of the formula MXO<sub>4</sub>. *Spectrochimica Acta*, 22(11), 1949–1961. [https://doi.org/10.1016/0371-1951\(66\)80183-2](https://doi.org/10.1016/0371-1951(66)80183-2)
- Hirsch, A., Kegler, P., Alencar, I., Ruiz-Fuertes, J., Shelyug, A., Peters, L., Schreinemachers, C., Neumann, A., Neumeier, S., Liermann, H. P., Navrotsky, A., & Roth, G. (2017). Structural, vibrational, and thermochemical properties of the monazite-type solid solution La<sub>1-x</sub>Pr<sub>x</sub>PO<sub>4</sub>. *Journal of Solid State Chemistry*, 245, 82–88. <https://doi.org/10.1016/J.JSSC.2016.09.032>
- Hunt, G. R. (1977). Spectral signatures of particulate minerals in the visible and near infrared. *Geophysics*, 42(3), 501–513. <https://doi.org/10.1190/1.1440721>
- Itakura, Y., Tsutsumi, S., & Takagi, T. (1974). Statistical properties of the background noise for the atmospheric windows in the intermediate infrared region. *Infrared Physics*, 14(1), 17–29. [https://doi.org/10.1016/0020-0891\(74\)90005-0](https://doi.org/10.1016/0020-0891(74)90005-0)
- Kalvig, P. (2022). Rare Earth Elements (REE). Geology, technologies, and forecasts. GEUS. *MiMa rapport* Vol. 2022 No. 1 <https://doi.org/10.22008/gpub/38124>
- Kijkowska, R., Cholewka, E., & Duszak, B. (2003). X-ray diffraction and Ir-absorption characteristics of lanthanide orthophosphates obtained by crystallisation from phosphoric acid solution. *Journal of Materials Science*, 38(2), 223–228. <https://doi.org/10.1023/A:1021188810349/METRICS>
- Knyazev, A., Savushkin, I., Mirsaidov, U., Lukoyanov, A., & Oganov, A. (2021). Synthesis and structure of triple thorium phosphates with monazite structure. *Journal of Radioanalytical and Nuclear Chemistry*, 327(3), 1105–1112. <https://doi.org/10.1007/S10967-020-07586-8/FIGURES/6>
- Kokaly, R. F., Clark, R. N., Swayze, G. A., Livo, K. E., Hoefen, T. M., Pearson, N. C., Wise, R. A., Benzel, W., Lowers, H. A., Driscoll, R. L., & Klein, A. J. (2017). USGS Spectral Library Version 7. *Data Series*. <https://doi.org/10.3133/DS1035>
- Laakso, K., Turner, D. J., Rivard, B., & Sánchez-Azofeifa, A. (2019). The long-wave infrared (8–12 μm) spectral features of selected rare earth element—Bearing carbonate, phosphate and silicate minerals. *International Journal of Applied Earth Observation and Geoinformation*, 76, 77–83. <https://doi.org/10.1016/j.jag.2018.11.005>
- Lafuente, B., Downs, R. T., Yang, H., & Stone, N. (2016). The power of databases: The RRUFF project. *Highlights in Mineralogical Crystallography*, 1–29. <https://doi.org/10.1515/9783110417104-003/MACHINEREADABLECITATION/RIS>
- Laukamp, C., Rodger, A., LeGras, M., Lampinen, H., Lau, I. C., Pejčić, B., Stromberg, J., Francis, N., & Ramanaidou, E. (2021). Mineral physicochemistry underlying feature-based extraction of mineral abundance and composition from shortwave, mid and thermal infrared reflectance spectra. *Minerals*, 11(4), 347. <https://doi.org/10.3390/min11040347>

- Lusty, P. A. J., & Gunn, A. G. (2014). Challenges to global mineral resource security and options for future supply. *Geological Society Special Publication*, 393, 265–276. <https://doi.org/10.1144/SP393.13>
- Morin-Ka, S. (2018). Detection and distinction of rare earth elements using hyperspectral technologies. *Geological Survey of Western Australia. Report 187*, 16p (accessed 25 Nov 2023) <https://dmpbookshop.eruditetechnologies.com.au/product/detection-and-identification-of-rare-earth-elements-using-hyperspectral-techniques.do>
- Müller, C. M., Pejčić, B., Esteban, L., Piane, C. D., Raven, M., & Mizaikoff, B. (2014). Infrared Attenuated Total Reflectance Spectroscopy: An Innovative Strategy for Analyzing Mineral Components in Energy Relevant Systems. *Scientific Reports 2014 4:1*, 4(1), 1–11. <https://doi.org/10.1038/srep06764>
- Murata, K. J., Rose, H. J., Carron, M. K., & Glass, J. J. (1957). Systematic variation of rare-earth elements in cerium-earth minerals. *Geochimica et Cosmochimica Acta*, 11(3), 141–161. [https://doi.org/10.1016/0016-7037\(57\)90077-7](https://doi.org/10.1016/0016-7037(57)90077-7)
- Papagelis, K., & Ves, S. (2003). Vibrational properties of the rare earth aluminum garnets. *Journal of Applied Physics*, 94(10), 6491–6498. <https://doi.org/10.1063/1.1623328>
- Rodger, A., Laukamp, C., Haest, M., & Cudahy, T. (2012). A simple quadratic method of absorption feature wavelength estimation in continuum removed spectra. *Remote Sensing of Environment*, 118, 273–283. <https://doi.org/10.1016/J.RSE.2011.11.025>
- Salisbury, J. W., Walter, L. S., & Vergo, N. (1987). Mid-infrared (2.1-25 um) spectra of minerals; first edition. *Open-File Report*. <https://doi.org/10.3133/OFR87263>
- Shannon, R. D., & IUCr. (1976). Revised effective ionic radii and systematic studies of interatomic distances in halides and chalcogenides. *Urn:Issn:0567-7394*, 32(5), 751–767. <https://doi.org/10.1107/S0567739476001551>
- Sheibley, D. W., & Fowler, M. H. (1966). Infrared spectra of various metal oxides in the region of 2 to 26 microns. NASA TN D-3750. *Technical note. United States. National Aeronautics and Space Administration*, 1–62.
- Silva, E. N., Ayala, A. P., Guedes, I., Paschoal, C. W. A., Moreira, R. L., Loong, C.-K., & Boatner, L. A. (2006). Vibrational spectra of monazite-type rare-earth orthophosphates. *Optical Materials*, 29(2–3), 224–230. <https://doi.org/10.1016/j.optmat.2005.09.001>
- Smelror, M., Hanghøj, K., & Schiellerup, H. (2023). Entering the Green Stone Age – introduction. *Geological Society, London, Special Publications*, 526(1), 1–12. <https://doi.org/10.1144/SP526-2022-312>
- Smith, B. C. (2011). *Fundamentals of Fourier Transform Infrared Spectroscopy*. <https://doi.org/10.1201/B10777>
- Stuart, B. H. (2004). Infrared Spectroscopy: Fundamentals and Applications. In *Infrared Spectroscopy: Fundamentals and Applications*. Wiley. <https://doi.org/10.1002/0470011149>
- Stuart, B. H. (2005). Infrared Spectroscopy: Fundamentals and Applications. *Infrared Spectroscopy: Fundamentals and Applications*, 1–224. <https://doi.org/10.1002/0470011149>
- Surovell, T. A., & Stiner, M. C. (2001). Standardizing infra-red measures of bone mineral crystallinity: an experimental approach. *Journal of Archaeological Science*, 28(6), 633–642. <https://doi.org/10.1006/JASC.2000.0633>
- Tan, W., Qin, X., Liu, J., Michalski, J., He, H., Yao, Y., Yang, M., Huang, J., Lin, X., Zhang, C., & Liang, X. (2021). Visible/near infrared reflectance (VNIR) spectral features of ion-exchangeable rare earth elements hosted by clay minerals: Potential use for exploration of regolith-hosted REE deposits. *Applied Clay Science*, 215, 106320. <https://doi.org/10.1016/J.CLAY.2021.106320>
- Thompson, T. J. U., Gauthier, M., & Islam, M. (2009). The application of a new method of Fourier Transform Infrared Spectroscopy to the analysis of burned bone. *Journal of Archaeological Science*, 36(3), 910–914. <https://doi.org/10.1016/J.JAS.2008.11.013>

- Van Ruitenbeek, F. J. A., Bakker, W. H., Van Der Werff, H. M. A., Zegers, T. E., Oosthoek, J. H. P., Omer, Z. A., Marsh, S. H., & Van Der Meer, F. D. (2014). Mapping the wavelength position of deepest absorption features to explore mineral diversity in hyperspectral images. *Planetary and Space Science*, *101*, 108–117. <https://doi.org/10.1016/J.PSS.2014.06.009>
- Williams, Q. (1995). Infrared, Raman and optical spectroscopy of Earth materials. In T. J. Ahrens (Ed.), *Mineral Physics & crystallography: A Handbook of Physical constants* (Vol. 2, pp. 291–302). <https://doi.org/10.1029/RF002p0291>
- Wim H. Bakker. (2024). wimhbakker/hyppy: HypPy3 (hyppy-v3). Zenodo. <https://doi.org/10.5281/zenodo.11204368>
- Yunxiang Ni, Hughes, J. M., & Mariano, A. N. (1995). Crystal chemistry of the monazite and xenotime structures. *American Mineralogist*, *80*(1–2), 21–26. <https://doi.org/10.2138/AM-1995-1-203>
- Zhang, M., & Salje, E. K. H. (2001). Infrared spectroscopic analysis of zircon: Radiation damage and the metamict state. *Journal of Physics: Condensed Matter*, *13*(13), 3057. <https://doi.org/10.1088/0953-8984/13/13/317>

# APPENDIX

Appendix I: The mass of REO for synthesizing monazite samples in this study

Single-REE		
Final product	Expected REE (mol)	REO need (g)
LaPO <sub>4</sub>	0.0050	0.8145
NdPO <sub>4</sub>	0.0050	0.8412
SmPO <sub>4</sub>	0.0050	0.8718

Double-REE: (La <sub>1-x</sub> Nd <sub>x</sub> )				
Final product	Expected La (mol)	La <sub>2</sub> O <sub>3</sub> need (g)	Expected Nd (mol)	Nd <sub>2</sub> O <sub>3</sub> need (g)
(La <sub>0.10</sub> Nd <sub>0.90</sub> )PO <sub>4</sub>	0.00050	0.0815	0.00450	0.7571
(La <sub>0.75</sub> Nd <sub>0.25</sub> )PO <sub>4</sub>	0.00125	0.2036	0.00375	0.6309
(La <sub>0.50</sub> Nd <sub>0.50</sub> )PO <sub>4</sub>	0.00250	0.4073	0.00250	0.4206
(La <sub>0.25</sub> Nd <sub>0.75</sub> )PO <sub>4</sub>	0.00375	0.6109	0.00125	0.2103
(La <sub>0.90</sub> Nd <sub>0.10</sub> )PO <sub>4</sub>	0.00450	0.7331	0.00050	0.0841

Double-REE: (La <sub>1-x</sub> Sm <sub>x</sub> )				
Final product	Expected La (mol)	La <sub>2</sub> O <sub>3</sub> needed (g)	Expected Sm (mol)	Sm <sub>2</sub> O <sub>3</sub> needed (g)
(La <sub>0.10</sub> Sm <sub>0.90</sub> )PO <sub>4</sub>	0.00050	0.0815	0.00450	0.7846
(La <sub>0.75</sub> Sm <sub>0.25</sub> )PO <sub>4</sub>	0.00125	0.2036	0.00375	0.6539
(La <sub>0.50</sub> Sm <sub>0.50</sub> )PO <sub>4</sub>	0.00250	0.4073	0.00250	0.4359
(La <sub>0.25</sub> Sm <sub>0.75</sub> )PO <sub>4</sub>	0.00375	0.6109	0.00125	0.2180
(La <sub>0.90</sub> Sm <sub>0.10</sub> )PO <sub>4</sub>	0.00450	0.7331	0.00050	0.0872



**Appendix II: (Table)** Crystallographic information of single-REE monazites from Sample Set 1 (data from Dijkstra et al., 2024)

Single-REE monazite (Sample Set 1)							
REE	Atomic no.	Ionic radii (Å) (CN = 9)	Unit cell parameters				Cell volume (Å <sup>3</sup> )
			a (Å)	b (Å)	c (Å)	β (°)	
La	57	1.216	6.8410	7.0775	6.5114	103.29	306.824
Ce	58	1.196	6.8005	7.0254	6.4741	103.48	300.786
Pr	59	1.179	6.7705	6.9893	6.4421	103.58	296.333
Nd	60	1.163	6.7444	6.9582	6.4116	103.69	292.335
Sm	62	1.132	6.6914	6.8938	6.3721	103.89	285.357
Eu	63	1.120	6.6704	6.8672	6.3549	103.95	282.512
Gd	64	1.107	6.6524	6.8467	6.3359	104.01	280.001

**Appendix III:** Crystallographic information of single and double-REE monazite synthesized in this study

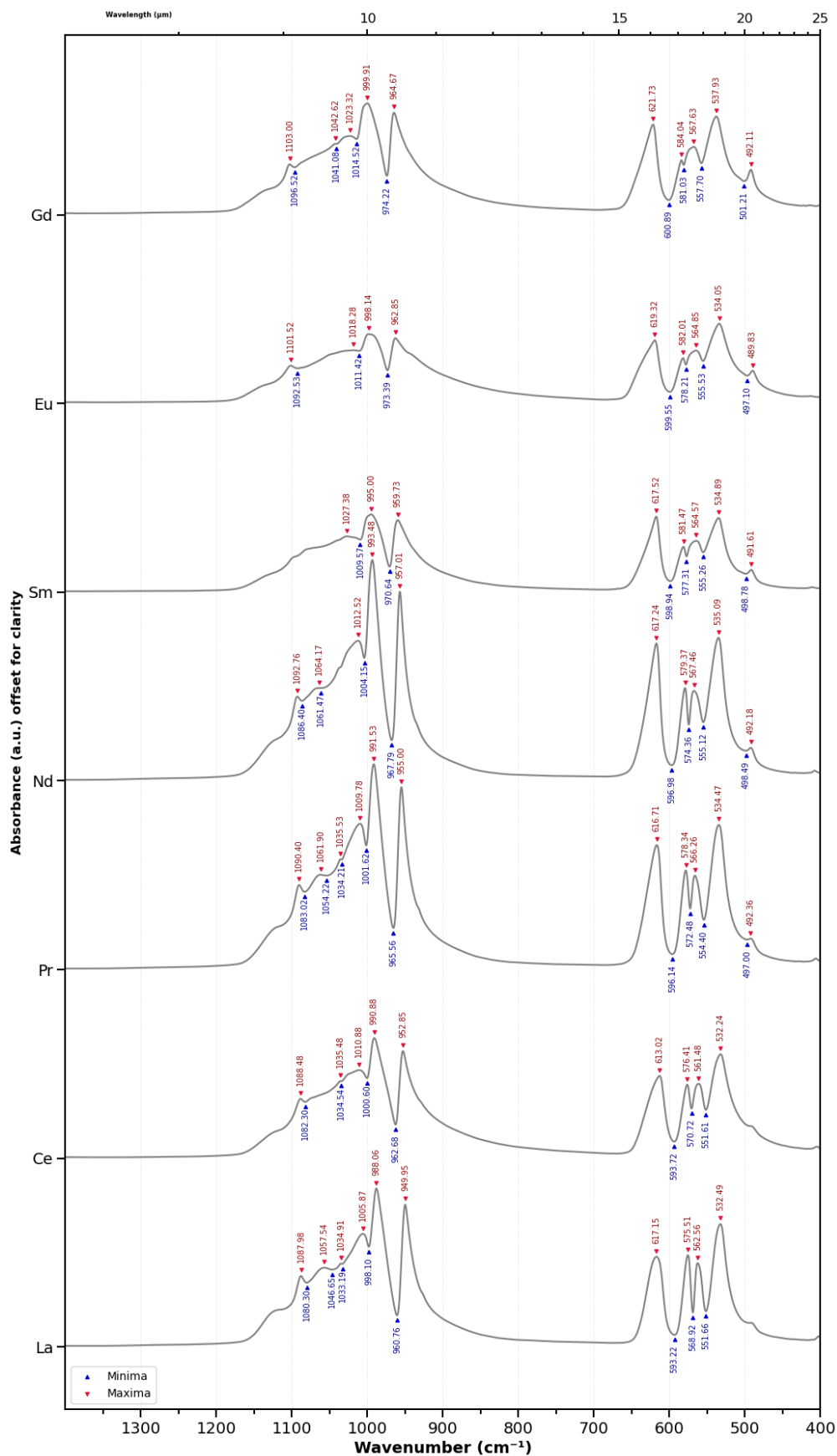
(Top) monazite-(La<sub>1-x</sub>Nd<sub>x</sub>) (\* indicates single-REE monazite – La: x = 0.00 and Nd: x = 1.00)

(Bottom) monazite-(La<sub>1-x</sub>Sm<sub>x</sub>) (\* indicates single-REE monazite – La: x = 0.00 and Sm: x = 1.00)

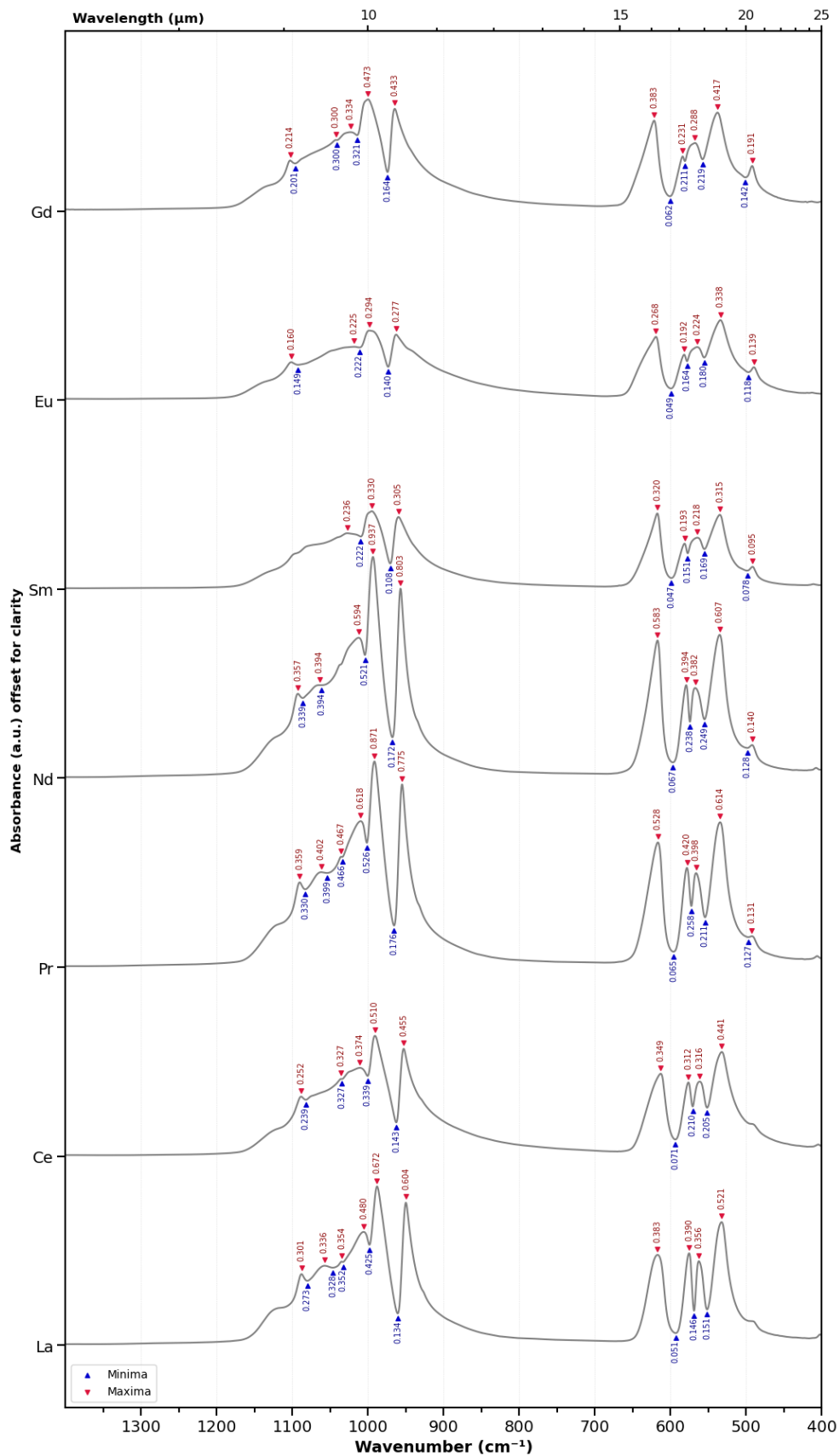
Monazite-(La <sub>1-x</sub> Nd <sub>x</sub> )					
x (Nd molar fraction)	Unit cell parameters				Cell volume (Å <sup>3</sup> )
	a (Å)	b (Å)	c (Å)	β (°)	
0.00*	6.8419	7.0776	6.5113	103.31	306.832
0.10	6.8317	7.0661	6.5010	103.36	305.332
0.25	6.8199	7.0507	6.4878	103.42	303.444
0.50	6.7946	7.0188	6.4631	103.53	299.673
0.75	6.7695	6.9895	6.4378	103.61	296.050
0.90	6.7528	6.9692	6.4203	103.67	293.587
1.00*	6.7436	6.9582	6.4105	103.72	292.223

Monazite-(La <sub>1-x</sub> Sm <sub>x</sub> )					
x (Sm molar fraction)	Unit cell parameters				Cell volume (Å <sup>3</sup> )
	a (Å)	b (Å)	c (Å)	β (°)	
0.00*	6.8419	7.0776	6.5113	103.31	306.832
0.10	6.8270	7.0589	6.4983	103.38	304.657
0.25	6.8055	7.0318	6.4793	103.47	301.539
0.50	6.7641	6.9826	6.4409	103.62	295.654
0.75	6.7276	6.9384	6.4067	103.77	290.468
0.90	6.7055	6.9109	6.3852	103.85	287.298
1.00*	6.6920	6.8942	6.3717	103.90	285.356

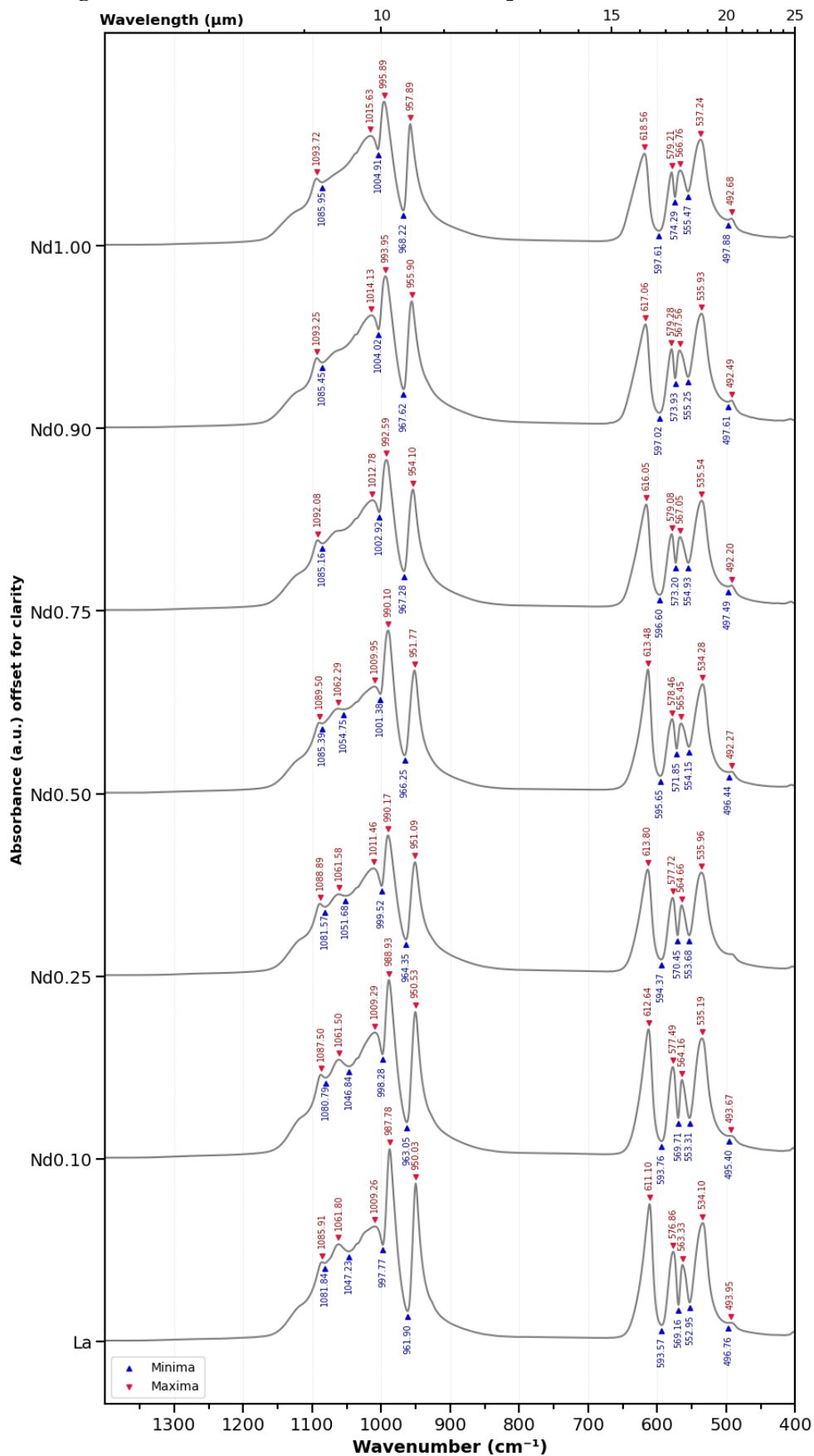
Appendix IV: Positions of all detectable features in the spectra of synthetic single-REE monazites from *Sample Set 1*



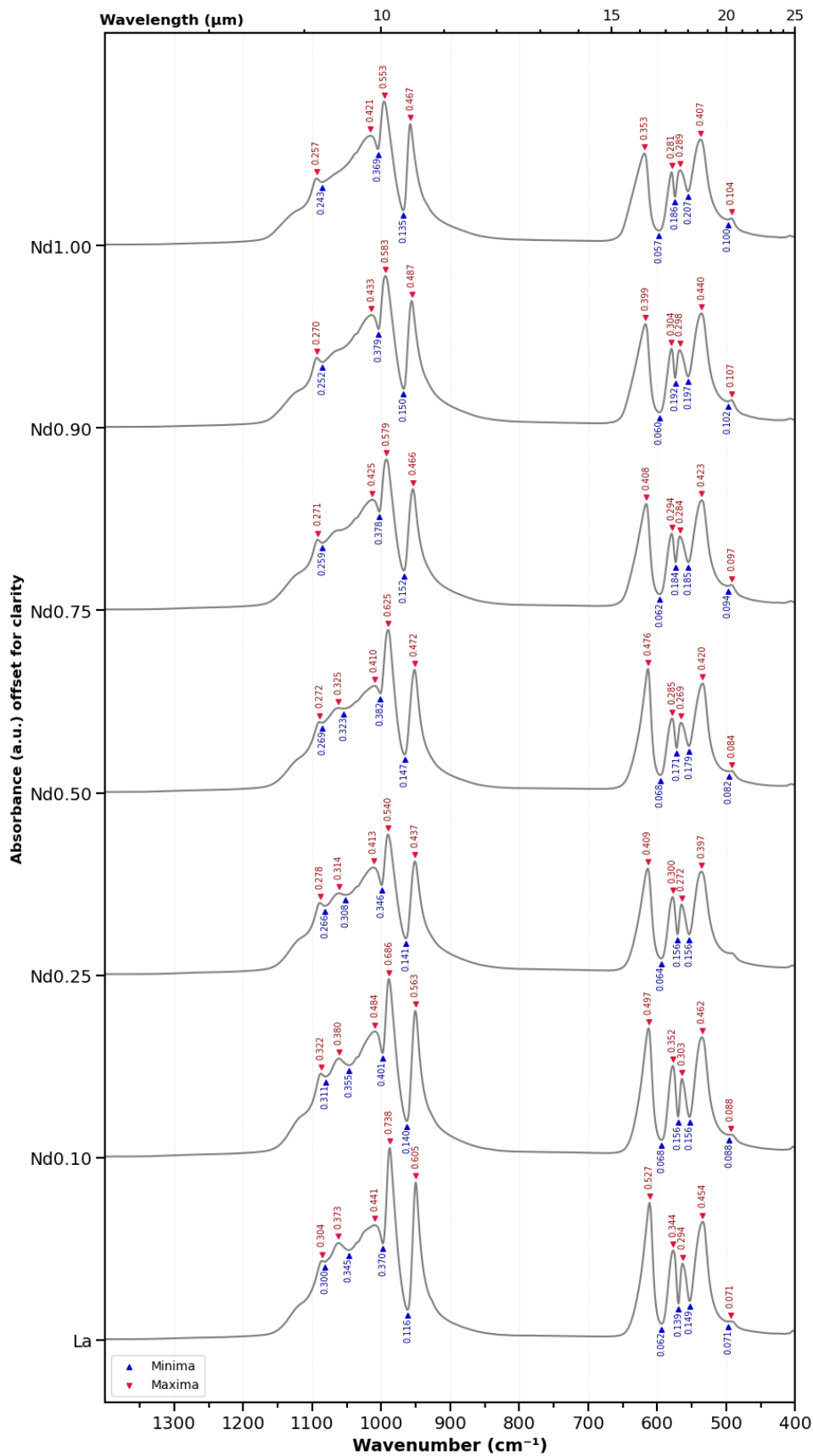
Appendix IV (Continued): Absorbance intensities of all detectable features in the spectra of synthetic single-REE monazites from *Sample Set 1*



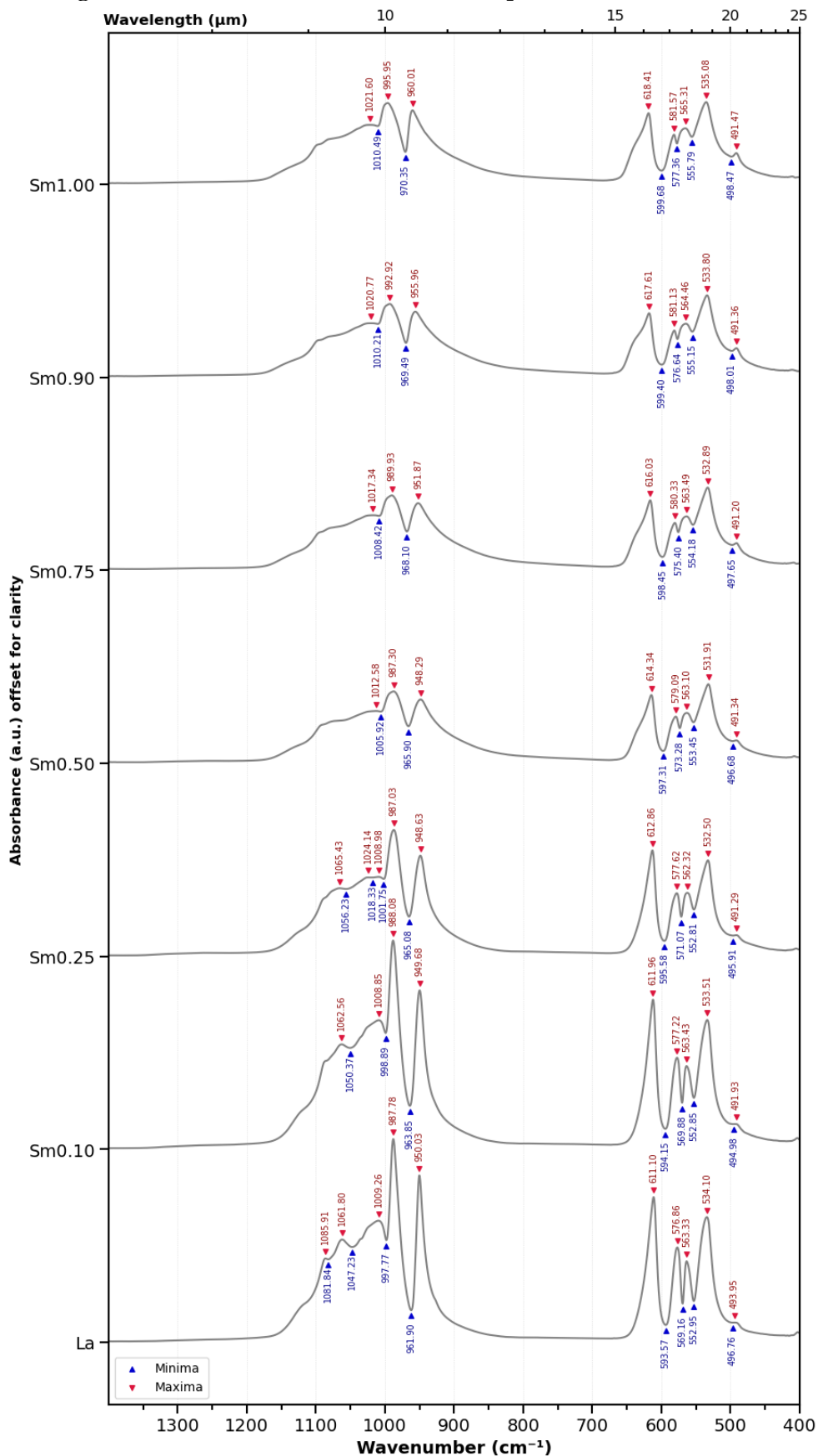
Appendix IV (Continued): Positions of all detectable features in the spectra of synthetic double-REE  $\text{La}_{1-x}\text{Nd}_x$  and single-REE: La and Nd monazites from *Sample Set 2*.



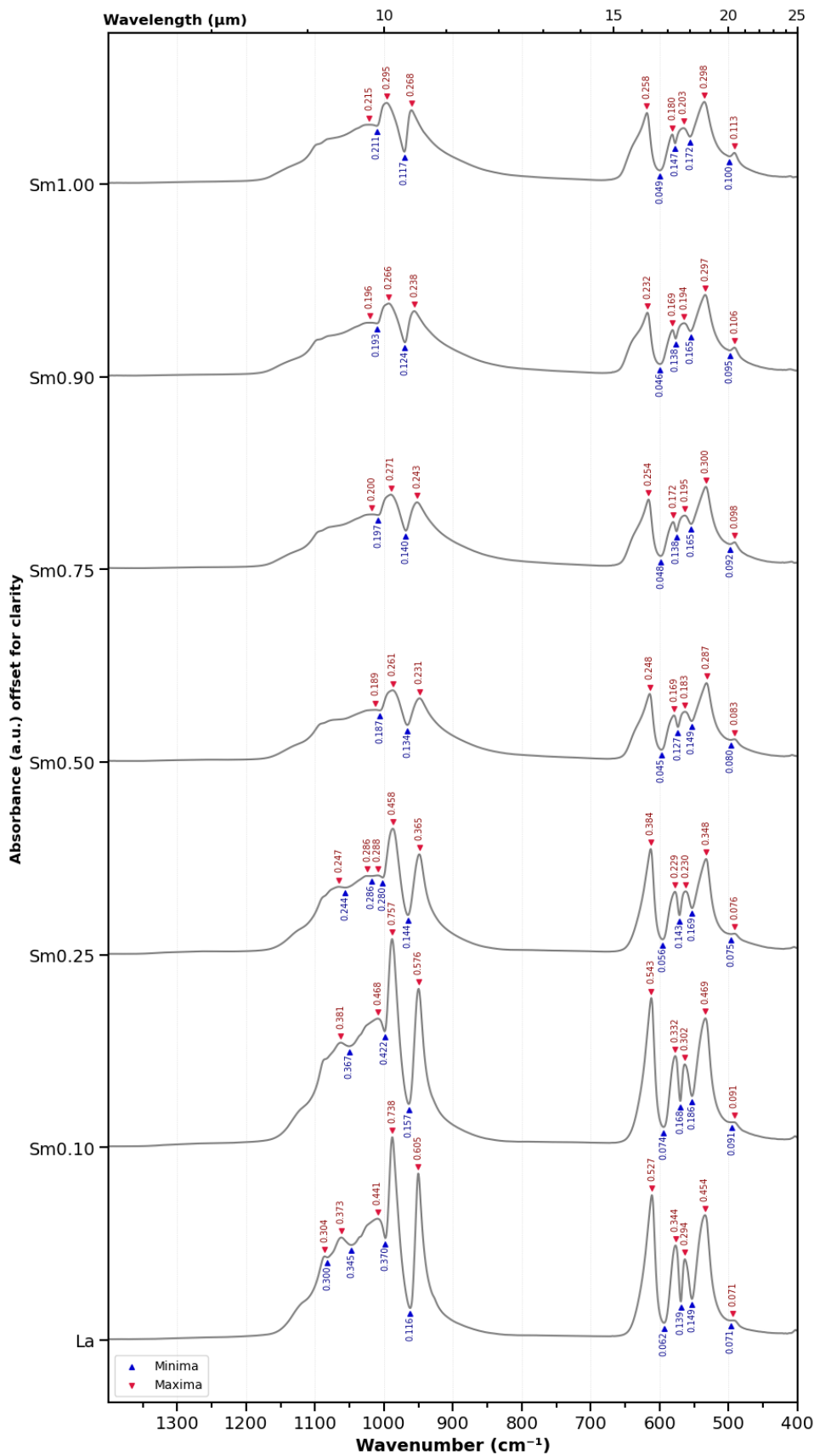
Appendix IV (Continued): Absorbance intensities of all detectable features in the spectra of synthetic double-REE  $\text{La}_{1-x}\text{Nd}_x$  and single-REE: La and Nd monazites from *Sample Set 2*.



Appendix IV (Continued): Positions of all detectable features in the spectra of synthetic double-REE  $\text{La}_{1-x}\text{Sm}_x$  and single-REE: La and Sm monazites from *Sample Set 2*.



Appendix IV (Continued): Absorbance intensities of all detectable features in the spectra of synthetic double-REE  $\text{La}_{1-x}\text{Sm}_x$  and single-REE: La and Sm monazites from *Sample Set 2*.



**Appendix V:** Scatter plots showing trend of positional shifts in every selected feature (both minima and maxima) of all monazite samples in this study. **(Left)** Single-REE monazites (from Sample Set 1 and 2) **(Middle)** monazite-(La<sub>1-x</sub>Nd<sub>x</sub>) **(Right)** monazite-(La<sub>1-x</sub>Sm<sub>x</sub>). The single-REE data is plotted against ionic radii of REE<sup>3+</sup> (CN = 9, Shannon, 1976), while double-REE data are plotted against molar fraction of Nd and Sm respectively. The trendline and correlation coefficient in single-REE plot correspond to Sample Set 1. Error bars indicates the minimum and maximum values obtained from the repeated measurement spectra of each sample. The plots are shown in sequence from higher to lower wavenumbers (cm<sup>-1</sup>).

